ADELAIDE UNIVERSITY AUSTRALIA

SUB CRUCE LUMEN

A HIGH POWER SCALABLE DIODE-LASER-PUMPED CW Nd:YAG LASER USING A STABLE-UNSTABLE RESONATOR

By

Damien Mudge

Thesis submitted for the degree of
Doctor of Philosophy

December, 2000

This work contains no material which has been accepted for the award of any other degree or diploma in any University or other tertiary institution and, to the best of my knowledge and belief, contains no material previously published or written by another person, except where due reference has been made in the text.

I give consent to this copy of my thesis, when deposited in the University Library, being available for loan and photocopying.

DATE: 15/2/01...

Supervisors: Dr. P. Veitch, Prof. J. Munch and
Dr. M. Hamilton

Acknowledgments

I would like begin by thanking my supervisors, Dr. Peter Veitch, Prof. Jesper Munch and Dr. Murray Hamilton for their support and guidance throughout my candidature. I particularly appreciated the fact that they could always be approached and always found time to discuss any difficulties encountered in the lab.

I would also like to thank the many people who have contributed to this work in various ways:

- Dr. Martin Ostermeyer, a visiting German research fellow who worked with me during the latter half of this thesis. His enthusiasm and useful suggestions were much appreciated.

- Todd Rutherford and Bill Tulloch at Stanford University for information on the application of Teflon to Nd:YAG slabs.

- I am indebted to the highly skilled staff in the Department of Physics workshop, Blair Middlemiss, Trevor Waterhouse and Greame Eames. Their assistance in manufacturing the custom components required for this work was invaluable and a necessity.

- I would like to especially thank Blair Middlemiss for his technical assistance in the design and development of the laser head in this thesis. His creativity, initiative and enthusiasm was instrumental in the technical construction of the laser.

- Mike Shorthose, Bob Nation and Bob Hurn for their assistance with computing and electronics.

- My colleagues in the optics group, for their cooperation, useful advice, and for contributing to a pleasant place to work.

- The friendly and helpful general staff of the Department of Physics, for their assistance.

- Peter Veitch, Jesper Munch, Kerry Corbett and Martin Ostermeyer for their assistance proof-reading this thesis.

- The Australian Research Council which supported this work under a Grant as part of the Australian Consortium for Interferometric Gravitational Wave Astronomy.

Finally, I wish to thank my parents, Pam and Geoff for their continued support and encouragement throughout my studies.

Abstract

Some modern laser applications require continuous wave (CW) high power (>100 W), and diffraction limited performance near 1.064 μm. One such laser application with these, and additional, requirements is gravitational wave interferometry. This thesis will report the development of a scalable high power laser for this application.

A high-power, single-transverse-mode laser might be produced by intensely pumping the small mode volume within a stable resonator or by using a resonator that has a large transverse mode. Intensely pumping a small volume can lead to crystal fracture and large thermally-induced wavefront aberrations. Using a large transverse mode would also be difficult if using a stable resonator as these are, in general, not suited to fundamental modes that have large cross-sectional areas.

Unstable resonators, by comparison, routinely produce fundamental modes that have large cross-sectional areas. They have been used for decades with high-power, high-gain chemical or gas lasers and provide efficient energy extraction, good mode discrimination and beam quality. However, the low gain of Nd:YAG in combination with the high output coupling associated with unstable resonators would limit the efficiency of such a CW laser. One way to utilize the properties of unstable resonators while reducing the output coupling, and thus increase the efficiency, is to use a stable-unstable resonator. These resonators are stable in one plane and unstable in the orthogonal plane, rather than unstable in both planes. The required output coupling can be further reduced without degrading the beam quality by using a Graded Reflectivity Mirror (GRM) as the output coupler. The soft aperturing of the GRM also eliminates diffraction loss associated with scraper mirrors in hard-edged unstable resonators, and enhances mode discrimination.

The stable-unstable resonator reported in this thesis is side-pumped by fibre-coupled diode-lasers and side-cooled. It uses a total internal reflection (TIR) zigzag slab geometry, in which the zigzag is co-planar with the pumping and cooling. The resonator is stable in the plane of the zigzag (horizontal) and unstable in the plane orthogonal to the zigzag [1]. In this configuration the strong thermal lensing in the horizontal direction is averaged out by the zigzag. The vertical thermal lens is

controlled by Thermo-Electric Coolers (TEC's) which are used to adjust the temperature of the bottom and top surfaces of the slab.

To test the performance of the side-pumped, side-cooled laser head it was operated initially with a stable resonator. Efficient operation was achieved[2] and will be reported. Control of the refractive index profile (thermal lens) using the TEC's on the bottom and top surfaces results in a vertical thermal lens that could be set to any value between 47 mm and 450 mm. The thermal lens encountered by the zigzag mode in the plane of pumping and cooling is weak (horizontal direction) and independent of TEC current. Thus, the thermal lensing in the horizontal and vertical directions is de-coupled, as is necessary for scalability of the mode volume in the vertical direction.

A travelling-wave (for ease of injection locking) stable-unstable resonator was investigated using a Fox-Li model, which assumed a greater pump power and mode volume than used for the laser head presented in this thesis. A strip, $n = 2$ super-Gaussian GRM is shown to be the optimum output coupler for the stable-unstable laser. Furthermore, it is shown that the output coupling loss associated with a resonator magnification of -1.3 could be sustained using pump densities below the crystal fracture limit. Useful operation over a realistic range of thermal lens focal lengths is predicted.

The validity of the Fox-Li modelling is confirmed using with a standing-wave stable-unstable resonator. The standing-wave resonator was chosen as it suited the available crystal and pump power used for the work in this thesis. The GRM reflectivity profile used the minimum commercially available profile radius. The vertical thermal lens is varied by adjusting the pump power, and then by adjusting the temperature of the bottom and top surfaces at full pump power. This demonstrated CW operation of the standing-wave laser with $M = 1.3$ and good beam quality. Good qualitative agreement with the Fox-Li model of the standing-wave resonator is thus confirmed.

Finally, suppression of the multiple longitudinal modes by injection locking is reported.

List of Symbols

Throughout this thesis, several symbols will be used repeatedly to represent specific quantities or parameters, the following is a list of these symbols and short descriptions for the readers convenience. This list is not exhaustive but every effort has been made to maintain conformity of symbols used here. Wherever possible standard symbols and notation have been used which appear in most laser texts.

R_o	...	Peak intensity reflectance of Graded Reflectivity Mirror
n	...	Order of Super-Gaussian function
k	...	Order of Parabolic function
n_c	...	Refractive index of crystal medium
M	...	Geometric magnification of the unstable resonator
g_o	...	Small-signal gain coefficient
l_g	...	Geometric pathlength in a laser crystal
$\eta_{g\varepsilon}$	...	Geometric extraction energy of a laser mode in a crystal
$\mathrm{TEM_{oo}}$	...	Transverse Electromagnetic Mode of zeroth order
λ_o	...	Optical wavelength in free space
θ_1	...	Total Internal Reflection (TIR) bounce angle in a laser crystal
θ_B	...	Brewster's Angle (= 61.2094° for Nd:YAG)
γ_{mn}	...	Eigenvalue of mode designated m, n in rectangular co-ordinates
r	...	Radius of mirror, laser rod or laser beam, measured from centre
w_m	...	Characteristic radius of supergaussian profile
a_m	...	Characteristic radius of parabolic profile
M_s	...	Material strength parameter (or material constant)
σ_{21}	...	Stimulated emission cross-section of $^4\mathrm{F}_{3/2} \rightarrow ^4\mathrm{I}_{11/2}$ in Nd:YAG
τ_f	...	Spontaneous flourescence lifetime
k	...	Thermal conductivity
λ_abs	...	Absorption wavelength
λ_e	...	Emission wavelength

$\mathrm{d}n/\mathrm{d}T$	...	Change in index of refraction with temperature
σ_f	...	Tensile fracture strength
α	...	Thermal expansion coefficient
E	...	Young's Modulus
I_s	...	Saturation intensity
A_m	...	Mode cross-section area
M^2	...	Beam quality parameter
ν	...	Poisson's ratio
η_s	...	Stokes factor
λ_{ht}	...	Thin film convection coefficient
h	...	Height of slab (x-direction)
w	...	Width of slab (y-direction)
l	...	Length of rod or slab gain medium (z-direction)
A	...	Area of pump faces
$\overline{R}$	...	Average reflectance of output coupler
P_p	...	Absorbed pump power
P_h	...	Thermal power absorbed by gain medium
Q	...	Heat absorbed per unit volume
l_p	...	Length of the pumped region
h_p	...	Height of the pumped region
w_p	...	Width of the pumped region
$T(y)$	...	Temperature as a function of y-position
T_c	...	Temperature of the flowing coolant
R_s	...	Thermal shock resistance parameter
σ_s	...	Surface stress
$\sigma_{\mathrm{max.}}$	...	Maximum surface stress at fracture
RN	...	Reynolds number
ρ	...	Density
v_f	...	Fluid speed
ξ	...	Viscosity
G	...	Single-pass small-signal gain factor

PFI	...	Fabry Perot Interferometer
η_q	...	Quantum efficiency
η_s	...	Stokes factor
η_{B}	...	Multimode beam overlap efficiency
V	...	Volume
CCD	...	Charge coupled device
f_{therm}	...	Thermal lens focal length
R_w	...	Wavefront curvature
$\widetilde{\gamma}$	...	Lens duct parameter related to the transverse variation of the index of refraction
n_o	...	Index of refraction of lens duct at optical axis
w_{pp}	...	Radius of Gaussian pump profile
n_p	...	Inversion density between the upper and lower laser level
a	...	Aperture radius
$\widetilde{u}_1(x)$	...	One-dimensional wavefunction
Y	...	Loss factor
$P_{out,\text{standing-wave}}$	...	Calculated output power for a standing-wave resonator
$P_{out,\text{travelling-wave}}$	...	Calculated output power for a travelling-wave resonator
w_{GRM}	...	GRM profile radius
L_o	...	On-axis optical length
W_p	...	Optical pumping rate
TIR	...	Total Internal Reflection
nb	...	Number of TIR bounces
$W(z)$	...	Laser beam radius
W_0	...	Laser beam radius at waist
z_0	...	$z-$location at waist

Contents

Chapter 1

Introduction

Efficient, high-power, continuous-wave (CW), solid-state lasers with good beam quality are sought for many medical, industrial, military and scientific applications. One very demanding scientific application of such a laser is as a source for a laser interferometric gravitational wave detector. This application currently requires reliable single-frequency ($\lambda \approx 1.06$ μm), fundamental mode operation in excess of 100 W, which can be efficiently coupled to high finesse Fabry-Perot cavities. The aim of this thesis is to describe a scalable solid-state laser designed to satisfy these requirements.

Diode-lasers are essential for pumping this type of high power laser, and they have become both reliable and economical in the last decade[3][4][5]. The ability to tune the narrow-band emission to the crystal absorption band maximizes the absorbed energy while minimizing heating of the laser medium.

Several techniques can be used to generate high power laser beams, for example: coherent addition of several phase-locked lasers; using a Master Oscillator Power Amplifier (MOPA) arrangement; or using a high power laser oscillator. A laser oscillator approach is investigated in this thesis, as these devices have optimized efficiency (see next section), and have well understood and controlled mode properties. Laser oscillators also achieve better gain saturation than MOPA systems, resulting in less Amplified Spontaneous Emission (ASE). Furthermore, the spectral properties of laser oscillators can be controlled by injection locking[6][7][8] (see discussion later).

1.1 Review of CW solid-state laser oscillators

Diode-laser-pumped Nd:YAG laser oscillators have been used in a variety of configurations. Only some of these are suitable for producing high output powers in a diffraction-limited TEM_{oo} beam, however. This section briefly reviews these configurations and discusses their efficiencies, advantages and disadvantages.

Contag *et al.*[9] have demonstrated a thin disk Yb:YAG laser with a TEM_{oo} power of 32 W with an optical efficiency of 49%. The thin disk laser concept can also be used with Nd:YAG[9]. To increase the power, multiple thin disks can be included at the expense of increasing the complexity of the resonator design. Alternatively, the amount of pump light absorbed by a single disk can be increased by increasing the absorption length of the pump light resulting in a short end-pumped, end-cooled rod geometry. If the absorption length of the disk becomes too long, heat can no longer be removed efficiently from the end, and side-cooling must be used.

Efficient CW operation of diode-laser end-pumped, side-cooled rod lasers is possible due to good spatial overlap of the pump light and the fundamental laser mode. Tidwell *et al.*[10] reported a near-diffraction-limited TEM_{oo} output power of 60 W with an optical efficiency of 26% from a Nd:YAG laser using two intracavity rods, each of which were pumped at both ends. However, the thermal fracture strength of the gain medium limits the pump density at the end face[11], and thus multiple end-pumped rods would be required to produce higher powers.

The high efficiency of end-pumped rods has been applied to a zigzag slab geometry by Neuenschwander *et al.*[12]. These authors individually end-pump the zigzag mode segments, in a bottom and top cooled slab laser, with four total internal reflection (TIR) bounces which produced a near TEM_{oo} output power of 4.5 W ($M^2_{horiz.} = 1.8$, $M^2_{vert.} = 1.5$), with an efficiency of 28%. However, the pumping of the individual elements is complicated due to the pump focussing optics. Also, increasing the pump power would require a longer crystal and more end-pumped segments, reducing the focal length of the thermal lens in the gain medium. At high powers the thermal lens would become too short for efficient fundamental mode operation.

Side-pumping of laser rods allow a greater amount of pump power to be deposited within the gain medium than when end-pumping. Golla *et al.* [13] have

demonstrated a TEM_{oo} output power of 62 W with an efficiency of 17%. The decrease in efficiency compared with the end-pumped rod is due to poorer extraction of the energy near the edges of the rod by the fundamental mode as well as the effects of thermally induced birefringence and lensing within the laser rod. The maximum TEM_{oo} output power is predicted by these authors to be limited to 100-150 W with decreasing efficiency for a single-rod laser.

The thermal lensing, stress-induced biaxial focusing and birefringence can be significantly reduced by using a side-pumped, side-cooled zigzag slab[14]. The reduced thermal focusing and birefringence has been verified experimentally by Kane *et al.*[15]. Shine *et al.* [16] used a side-pumped, side-cooled zigzag slab laser to produce 40 W of TEM_{oo} output with an optical efficiency of almost 19%. The improved efficiency is most likely due to the improved energy extraction efficiency near the edges of the slab where the pump density is greatest. This efficiency should be maintained to higher powers due to the reduced effects of stress-induced biaxial focusing and birefringence of the slab geometry. The side-pumped, side-cooled slab geometry has also been successfully used by several authors in high average power (pulsed) solid-state laser designs[17][18][19][20][21][22]. Thus, the reduced thermal lensing, stress-induced biaxial focussing and birefringence of the side-pumped, side-cooled zigzag slab laser suggest that it is the most appropriate gain medium geometry for a high power solid-state laser.

Side-pumped, bottom/top cooled slab lasers in which the mode zigzags in the plane orthogonal to the main temperature gradient can also achieve good efficiency[23]. However, they cannot be used to produce high powers as the focal length of the thermal lens becomes too short for efficient fundamental mode operation.

All of the CW approaches described above used stable resonators. Stable resonators often exhibit problems such as poor mode discrimination and poor overlap of the pump and fundamental mode volumes for practical resonator stabilities, which decreases the efficiency. Many of these problems can be avoided by using an unstable resonator. The useful properties of these resonators were discussed in detail by Siegman[24] in 1965. Since then unstable resonators have been used extensively in high-gain chemical and gas lasers[25][26][27][28], where they simultaneously

produce diffraction-limited beams and efficient power extraction from extended gain media. Unstable resonators have also been used to produce kilo-Watt average power from flash-lamp-pumped solid-state lasers with beam-parameter products around 10 mm-mrad[18][19][20][29][30][31][32][33]. It has also been shown that for an unstable resonator the beam quality is largely insensitive to changes in the refractive power of a thermal lens compared to a stable resonator[34][35].

Unstable resonators have not previously been used with CW solid-state lasers as these resonators usually have large output coupling (see Chapter 2) while CW solid-state lasers have relatively low gain. However, the higher-gain densities achievable using fibre-coupled high-power diode-lasers in addition to improved output couplers which use graded reflectivity mirrors (GRM's), encourage the application of unstable resonators to the production of high-power, diffraction-limited, CW solid-state lasers[1]. Diode-lasers minimize the heat deposited in the gain medium allowing an increase in the small-signal gain while remaining below the crystal fracture limit. Fibre-coupled diode-lasers enable the pump density to be increased and separates the diode-lasers from the laser head. The smoothly varying reflectivity of a GRM output coupler avoids edge-diffraction associated with hard-edged output couplers, and thus the magnification needed to produce good mode discrimination and beam quality can be reduced, which reduces the gain-length product required for efficient oscillation.

1.2 Thesis overview

This thesis describes the development of a high power scalable diode-laser-pumped CW Nd:YAG laser using a stable-unstable resonator. As indicated in section 1.1, the reduced thermal lensing, stress-induced biaxial focusing and birefringence of the side-pumped, side-cooled slab geometry are desirable characteristics for high power lasers. Furthermore, such lasers would benefit from the large mode volume and good mode discrimination of an unstable resonator. Chapter 2 gives a brief overview of unstable resonators and essential properties such as dynamic stability, mode discrimination and output coupling.

The limitation for use with low-gain CW solid-state lasers is the large output coupling usually associated with unstable resonators. The work in this thesis shows that a low magnification unstable resonator can be employed through careful selection of laser head and pump geometry. A conceptual high power laser design using a zigzag slab geometry and an unstable resonator is presented in Chapter 3. The best choice of solid-state laser host medium, and additional advantages of slab gain media compared to rod gain media are highlighted. The temperature distribution in the slab and the stress fracture limit are also discussed. The design of the laser head is presented in Chapter 4.

Chapter 5 characterizes the single-pass loss and gain of the side-pumped, side-cooled laser head. The strength of the thermal lensing is investigated using an interferometric technique as a function of the slab boundary conditions, with the aim of establishing the scalability of the laser head design. The remainder of Chapter 5 describes the efficiency, optimum output coupling, multimode and fundamental mode operation of the laser head using a stable resonator. The multimode output power using a stable resonator is compared to a predicted value.

Chapter 6 discusses the numerical model of a travelling-wave stable-unstable resonator and demonstrates numerically that the proposed resonator configuration is feasible. The surface stress of the gain medium for a 100 W output power system is also evaluated.

The travelling-wave resonator is required for ease of injection locking, which is the long-term aim of this work. Injection locking to a master oscillator can be used to control the spectral properties of the CW slave resonator[6][7][8], and prevents the generation of excess noise associated with free-running unstable resonators [36]. Injection locking of unstable resonators typically uses 'adjoint coupling,' a technique to efficiently couple the injected master field to the unstable resonator fundamental mode[37][38][39].

To investigate the operation of a stable-unstable resonator experimentally, a standing-wave stable-unstable resonator was used in conjunction with the laser head in Chapter 7. A standing-wave stable-unstable resonator was used instead of a travelling-wave resonator due to the limited gain available in the particular laser.

The results of these experiments are compared to the predictions of a Fox-Li model of the standing-wave unstable resonator. This enables the validity of the Fox-Li model to be verified and thus give evidence that the numerical model of the travelling-wave unstable resonator in Chapter 6 is valid. Finally, preliminary experiments that successfully demonstrate injection locking of the laser are discussed.

Two publications describe the work contained in this thesis. The first, discusses the design of the high power scalable diode-laser-pumped solid-state laser using a stable-unstable resonator, and the second describes and characterizes the laser head used in this thesis. Copies of both of these publications are included in App. G.

Note that almost a year after the first publication appeared, an alternative CW stable-unstable laser design was published[40]. This laser is an end-pumped, bottom and top-cooled slab design in which the output of a diode-laser stack is imaged through the max-R mirror on the end face of a slab. The authors reported an output power of 22 W with an optical-to-optical efficiency of 30%, and beam quality characterized by $M^2_{\text{stable}} = 1.6$ and $M^2_{\text{unstable}} = 1.3$. The resonator was stable in the direction of cooling, and unstable in the directions orthogonal to pumping and cooling. The unstable resonator had a magnification of 1.06. This laser is not readily scalable since the stable mode is dependent on the focal length of the vertical thermal lens, which will change with pump power. This limitation is the same as that of the side-pumped, bottom and top cooled design of Richards and McInnes, mentioned above. However, the authors of [40] showed the low magnification stable-unstable resonator can be used to achieve good efficiency and good beam quality in the unstable plane, and further supports the approach first proposed and subsequently used in this thesis.

Chapter 2

Unstable Resonators

This Chapter describes the development of unstable resonators, their properties and advantages. Several thorough reviews of unstable resonators appear in the literature[41][42][43]. The first part of this Chapter is based on the review by Morin[43].

Stable resonators with acceptable sensitivity to misalignments and perturbations such as refractive power changes are limited to producing Gaussian modes with an intra-cavity diameter of a few millimetres at most. Efficient energy extraction from extended gain regions using stable resonators is achieved typically only by oscillation with many higher-order modes. In the absence of apertures the loss for the higher-order stable modes, is in principle the same as for the fundamental mode given the uniform reflectance of the output coupler. Higher-order transverse modes in a stable resonator oscillate at slightly differing frequencies, due to the Guoy phase shift between the lowest- and higher-order Hermite-Gaussian (or Laguerre-Gaussian) transverse modes[44]. The Guoy phase shift degrades the focussing properties of the laser beam[44]. Furthermore, it is not possible to simultaneously injection lock all of these higher-order modes. Mode discrimination can only be achieved by using an intra-cavity aperture. This is possible since the transverse modes have different dimensions within the resonator.

Unfortunately, suppressing the higher-order modes wastes laser energy, it would be preferable to use this energy as laser output. Diffraction output coupling, in which light leaks past the edge of a small reflecting output coupler was suggested

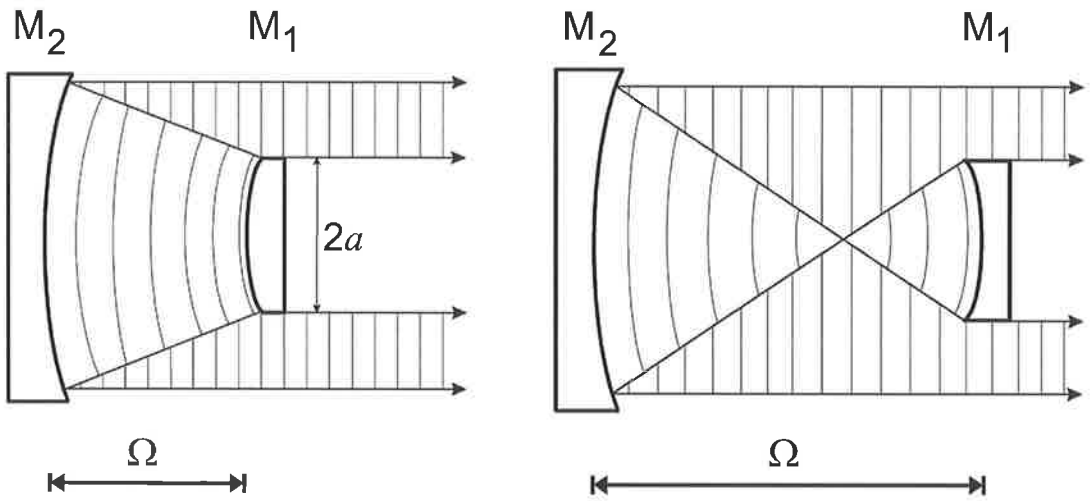

Figure 2.1: Positive- (left) and negative-branch (right) confocal unstable resonators.

by LaTourette *et al.*[45]. Soon after, Siegman[24] proposed the use of an unstable resonator. These resonators are able to produce single-mode beams, that have a large fundamental-mode cross-section. Unstable resonators transversely magnify the self-reproducing mode each round-trip by a factor, M, the 'Magnification' of the resonator. Thus the light walks transversely out of the resonator at a rate dependent on M. The output coupled field is that fraction of the mode leaking past the edge of the smaller, finite diameter mirror.

Typical examples of a positive- and negative-branch confocal unstable resonators are illustrated in Figure 2.1. The geometric magnification is defined by the ratio of the curvatures of M_2 and M_1. The distance between the mirrors, Ω, is given by f_1+f_2, where f_i is the focal length of mirror M_i (f_1 is negative for a convex mirror). The near-field output of the unstable resonator with a hard-edged output coupler has an annular cross-section. The most obvious difference between these resonators is that the negative-branch unstable resonator has an intracavity focus. The intra-cavity focus can cause breakdown in air in high peak power systems. Positive-branch resonators are often preferred when the length of the gain medium is a significant fraction of the resonator length, as the gain extraction is improved. Positive- and negative-branch unstable resonators have different perturbation stabilities, especially at low magnifications[46], these are discussed further in section 2.1.

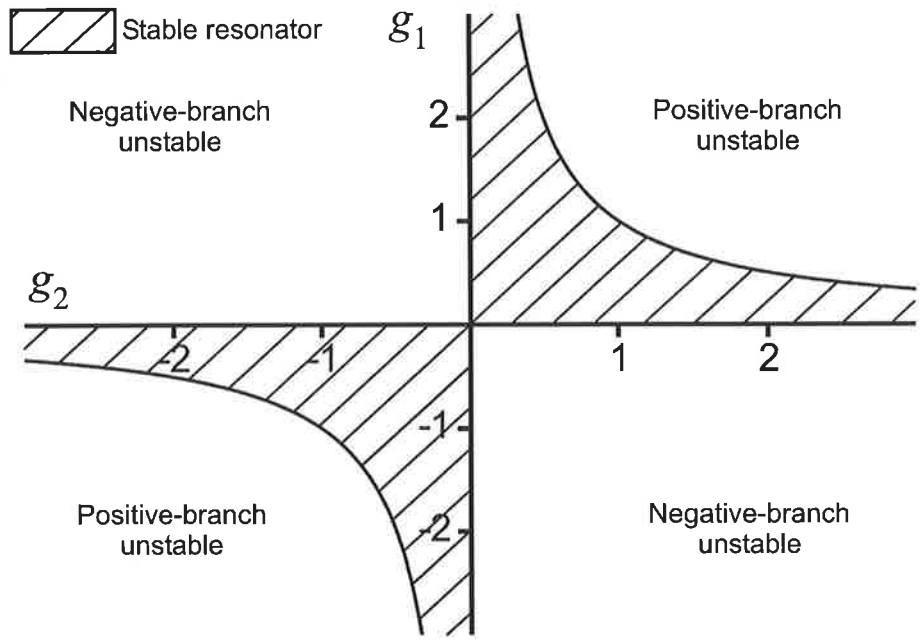

Figure 2.2: Resonator stability diagram (g-diagram) showing parameters g_1 and g_2. Negative- and positive-branch unstable regions are labelled and the shaded region indicates stable resonator operation.

Figure 2.2 shows a resonator stability diagram. The g-diagram shows regions of resonator stability (shaded), and thus also indicates regions where the resonator is unstable (unshaded). The g-parameters, are given by

$$g_i = 1 - \frac{\Omega}{R_i}, \qquad i = 1, 2 \tag{2.1}$$

where R_1 and R_2 are the radii of curvature of mirrors M_1 and M_2. The resonator is stable if $0 < g_1 g_2 < 1$.

An alternative stability parameter, β, is given by[43]

$$\beta = \left| \frac{A + D}{2} \right| \tag{2.2}$$

where A and D are the elements of the resonator round-trip ABCD matrix. The resonator is stable if $-1 < \beta < 1$. The two parameters are related by $\beta = 2g_1g_2 - 1$.

For a positive-branch unstable resonator, the magnification, M_p, is[43]

$$M_p = \beta + \sqrt{\beta^2 - 1} \tag{2.3}$$

and for a negative-branch unstable resonator, the magnification, M_n, is [43]

$$M_n = \beta - \sqrt{\beta^2 - 1} \tag{2.4}$$

Note that M_n is less than -1. The negative sign indicates a negative-branch unstable resonator, and $|M_n|$ is the geometric magnification each round-trip.

A useful feature of the unstable resonator is that the output coupling of the modes depends on the magnification of the resonator and is independent of the size of the output coupler, for large Fresnel numbers[47]. Higher-order transverse modes have substantially higher loss per pass, as more of the energy in these modes is concentrated near the edges of the resonator and is thus lost more rapidly[47]. Hence, mode discrimination is also determined by the magnification of the resonator, as discussed further in section 2.2.

While geometric approximations of unstable resonators were known to accurately predict the wavefront curvature, they poorly estimated the laser mode intensity profile. Large 'diffraction ripples' are observed on the intensity profile in practice. This is due to edge-diffraction causing backscatter from the hard-edges of the output coupler within the resonator [48]. It was found that losses of the individual modes varied quasi-periodically with equivalent Fresnel number[49] (A discussion of Fresnel numbers is included in Appendix A). For integral equivalent Fresnel numbers, the unstable resonator eigenvalues have the same magnitude (loss) but have different phase angles[42][48]. The magnitudes of the transverse mode eigenvalues are most different at half-integral equivalent Fresnel numbers, and thus mode discrimination is maximum. Hence, hard-edged output coupler unstable resonators should

be designed to operate at half-integral equivalent Fresnel numbers.

The near-field of early unstable resonators would have been of little practical use for efficient coupling into a high finesse Fabry-Perot cavity because of the diffraction from the edge of the output coupler mirror which degraded the beam quality, resulting in a significant fraction of the energy being located in side-lobes in the far-field. In applications requiring a single intensity lobe, the side lobes must be removed thereby reducing the overall efficiency of the laser. This is particularly significant for low magnification resonators, where the fraction of the mode leaking past the edge of the output coupler is small and the influence of edge diffraction is significant[46][50][51]. For these reasons, high magnification resonators were traditionally used, where the mode area was large compared to the output coupler area, and hence the effect of the edge-diffraction was small. Unfortunately, high magnification requires high gain due to the large output coupling.

Avoiding diffraction from the hard-edges of the output coupler would be an advantage. Anan'ev and Sherstobitov[52] suggested apodizing the output coupler to achieve smoothly varying reflectivity profiles. It was expected that the effects of edge-diffraction within the resonator would be decreased, thus removing the periodic loss with equivalent Fresnel number, and the resonator would be less sensitive to Fresnel number fluctuations.

Early theoretical work focussed on the use of a Gaussian reflectivity profile because that particular reflectivity profile could be treated with ABCD matrix formalism, thus simplifying the analysis[53][54]. However, it was postulated that the broad Gaussian profile would not be ideal if the gain medium is defined by limiting apertures such as edges of the gain media, and energy extraction would not be optimal. This generated interest in parabolic and super-Gaussian profiles, which are discussed in section 2.3. Unfortunately, the modes of resonators which use these mirrors cannot be described with closed-form analytic solutions and numerical solutions are required[55].

It was presumed that proper design of the output coupler reflectance profile allowed some control over the transverse cavity field distribution. A lack of available components initially delayed the use of apodization in unstable resonators. A

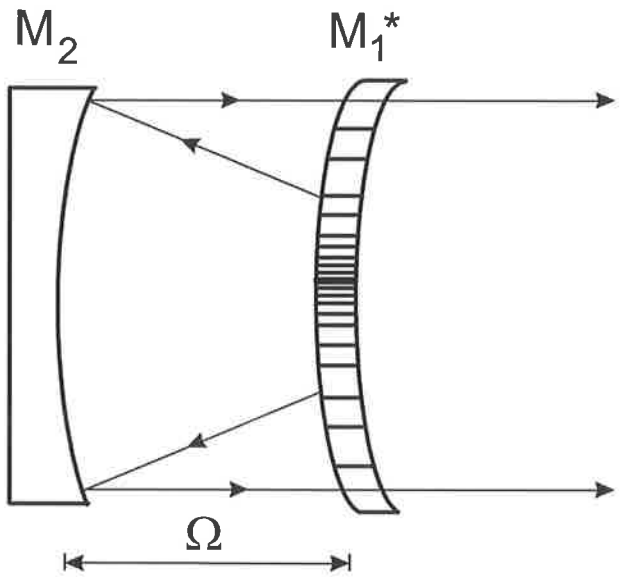

Figure 2.3: Confocal positive-branch unstable resonator with a Graded Reflectivity Mirror, M_1*.

radially variable birefringent element along with a polarizer was first used to realize apodization with a graded reflectivity profile for an unstable resonator[56][57]. However, difficulties were encountered if the gain medium was birefringent.

An effective solution to this problem is the use of dielectric graded reflectivity mirrors (GRM's). The low loss and the high damage threshold of these coatings allow use in laser cavities. Their functionality is the same as regular mirrors allowing simple alignment and cleaning. Figure 2.3 shows a confocal GRM unstable resonator. M_1 in Figure 2.1 (left) has been replaced by the GRM, M_1*. The first implementation of a GRM used a single variable thickness layer of material with a high refractive index. These devices were limited to a near-infrared reflectivity of 50% at most. The peak reflectivity was later increased by using multiple-layer designs[58][59][60], which led to commercial fabrication of GRM's.

Large single mode operation with a far-field that is free of side-lobes has been demonstrated with a GRM unstable resonator[61]. Furthermore, misalignment of the resonator did not favor oscillation of higher-order modes, as was previously observed in hard-edged unstable resonators[46][62]. Thus the mode discrimination benefits of apodization in unstable resonators and the improved beam quality with the absence of hard-edge diffraction were verified. The term GRM (Graded Reflec-

tivity Mirror) is principally used in this thesis, however they are also referred to as variable reflectivity mirrors (VRM's). Dielectric GRM's are one of the key components of the laser design developed in this thesis, and are used in Chapters 6 and 7.

2.1 Dynamic stability

The dynamic stability of the confocal unstable resonator is different for positive- and negative-branch resonators, and affects the mode structure, output coupling, output power, beam pointing and the beam quality. The sensitivity of these resonators to perturbations is discussed briefly below.

Krupke and Sooy[46] show that the variation in output coupling (or variation in M) for a small change in one of the resonator mirror curvatures or the focal length of the thermal lens is greater for positive-branch than for negative-branch unstable resonators. The authors conclude that the greater tolerance of the negative-branch resonator to these changes arises because of the greater curvature of it's mirrors.

The sensitivity of the resonator to changes in length is also important. Negative-branch resonators were shown to be much more sensitive to variations in the resonator length than the positive-branch[46]. This was demonstrated by analyzing the effect of a resonator length change on the central far-field power density.

The final perturbation considered here is mirror misalignment. From a geometric view, if M2 in Figure 2.1(a) is tilted by an angle, θ, then the optic axis will be rotated by an angle ϕ about the centre of curvature of M1. For confocal resonators the relationship between these angles are[46]

$$\frac{\phi}{\theta} = \frac{2|M|}{|M|-1} \qquad \text{(positive-branch)} \tag{2.5}$$

$$\frac{\phi}{\theta} = \frac{2|M|}{|M|+1} \qquad \text{(negative-branch)} \tag{2.6}$$

	Positive-branch	Negative-branch
Δ(Thermal lens) sensitivity	high	low
Δ(Resonator length) sensitivity	low	high
Mirror tilt sensitivity	high	low

Table 2.1: Comparison of alignment stability parameters of positive- and negative-branch unstable resonators.

That is, for the same $|M|$, the negative-branch is always less sensitive to mirror misalignment than the positive-branch. Note that this is particularly important close to $|M| = 1$. Table 2.1 summarizes the results in this section.

2.2 Mode discrimination

Mode discrimination properties are an integral part of any resonator design. Unstable resonators achieve mode discrimination by utilizing the change in reflectance of the output coupler with radial distance from the optical axis. The average reflectance of the output coupler is different for each transverse laser mode. The lowest-order mode has the greatest reflectance, and higher-order modes experience greater loss as the transverse mode order increases. Thus, the oscillation threshold for each transverse mode is different and increases with the order of the mode.

Another description of the behavior of unstable resonators is to consider the power loss per round-trip, given by $1-|\gamma|^2$ where γ is the eigenvalue of the mode[63]. In the geometric optical limit, as $N_{eq} \rightarrow \infty$ (N_{eq} is the equivalent Fresnel number, and is defined in App. A), the eigenvalues for resonators which have toroidal, spherical and strip geometries (the strip geometry refers to a resonator that is unstable in one dimension, typically using cylindrical optics) are given by[42] [47]

$$\gamma_{mn,\text{toroid.}} = \frac{1}{|M|^{n+m+1}}, \qquad m,n = 0,1,2... \tag{2.7}$$

$$\gamma_{pl,\text{spherical}} = \frac{1}{|M|^{p+1}}, \qquad p = 0,1,2... \tag{2.8}$$

$$\gamma_{n,\text{strip}} = \frac{1}{|M|^{n+1/2}}, \qquad n = 0, 1, 2... \tag{2.9}$$

where M is the geometric magnification of the unstable resonator, m and n are Cartesian mode indices, p and l are the radial and azimuthal mode indices.

For a given magnification, M, the eigenvalue of a strip resonator is greater than the toroidal and spherical resonators, and thus the lowest-loss mode in the strip unstable resonator will experience less loss. Alternatively, since the average reflectivity of the output coupler is given by[63]

$$\overline{R} = R_o \gamma^2 \tag{2.10}$$

where R_o is the peak reflectivity of the GRM (see later), the average reflectivity for the lowest-order mode in a one-dimensional strip resonator is a factor of M larger than for the lowest-order mode in a two-dimensional toroidal or spherical resonator (see Equations 2.7-2.10 for m, n and $p = 0$). A strip unstable resonator is therefore more appropriate for low-gain lasers.

The mode discrimination compares the loss factors of a mode and the next higher-order mode. That is the mode discrimination between modes a and b is given by the ratio γ_a/γ_b. The ratio of the eigenvalues for a particular mode and the next higher-order mode is therefore equal to M for all resonator geometries (using Equations 2.7-2.9), and thus there is no mode discrimination penalty in using the lower-loss strip unstable resonator. To investigate the mode discrimination of unstable resonators, VSOURCE and VRM software was used, which are sub-modules of PARAXIA[1].

VSOURCE implements the virtual source formulation that estimates the eigenvalues and eigenmodes of hard-edged strip or cylindrical unstable resonators[64][65][66][67]. The eigenvalues are calculated as a function of equivalent Fresnel number, and the eigenmode intensity distribution just before the hard-edged output coupler

[1]PARAXIA Resonator and Optics Programs version 2.02, distributed by SCIOPT Enterprises, P.O. Box 20637, San Jose, CA 95160, U.S.A.

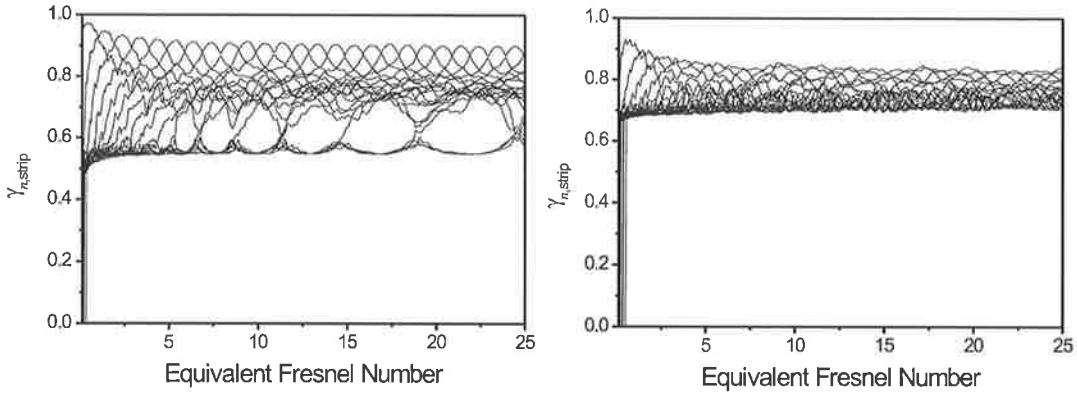

Figure 2.4: Loss factor for hard-edged unstable resonators for even (left) and odd (right) modes. Magnification = 1.3. Calculated using VSOURCE.

can be estimated.

VRM uses analytical results given by Doumont *et al.*[39]. This code gives the eigenvalues of strip or spherical unstable resonators with a variable reflectivity mirror. The eigenvalues are calculated as a function of equivalent Fresnel number. VRM can also calculate the eigenmode intensity distribution just before the variable reflectivity mirror output coupler. This formalism is limited to VRM's (or GRM's) with a Gaussian reflectivity profile.

2.2.1 Mode discrimination plots

Figure 2.4 shows plots of mode discrimination as predicted by VSOURCE, for an unstable resonator with magnification, 1.3, using a strip hard-edged output coupler. This resonator configuration was chosen for comparison as a strip GRM unstable resonator with $M = 1.3$ is used in Chapters 6 and 7. The eigenvalue magnitudes are plotted as a function of equivalent Fresnel numbers for the first 20 even (left) and the first 20 odd (right) modes of the resonator. Note the quasi-periodic, interleaving structure of the eigenmodes for the hard-edged unstable resonator, due to the edge diffraction from the output coupler as discussed earlier. Figure 2.4 illustrates the need to operate at half-integral equivalent Fresnel numbers, where the eigenvalue separation between the largest eigenvalue and the next nearest eigenvalue is greatest.

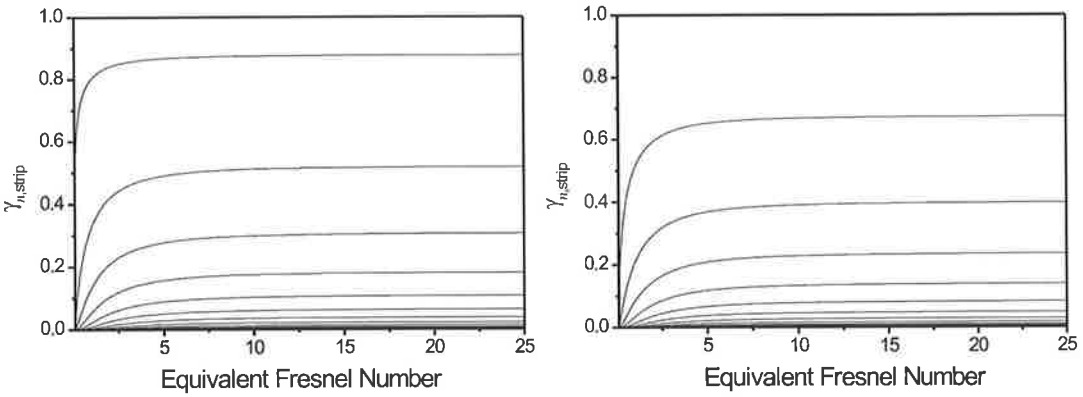

Figure 2.5: Loss factor for a GRM unstable resonator for even (left) and odd (right) modes. Magnification = 1.3. Calculated using VRM.

A similar plot for a resonator with a Gaussian GRM output coupler (generated using VRM code), is shown in Figure 2.5. The advantage of replacing the hard-edged output coupler with a GRM is clearly evident as the mode discrimination is essentially independent of Fresnel number. Furthermore, the separation between the lowest- and next higher-order mode is much greater than in Figure 2.4, and is large even though M is relatively small (1.3). The eigenvalue magnitudes approach their geometric values for large Fresnel numbers as predicted by Equation 2.9.

The VSOURCE and VRM programs were used to provide insight into the mode discrimination and beam quality of the unstable resonator as a function of magnification and Fresnel number.

In practice, more complex resonator designs involving finite apertures and non-Gaussian GRM profiles are used. These designs require a full physical optics analysis, such as the technique suggested by Fox and Li[68] [69]. This technique yields the lowest-loss unstable resonator mode but does not provide any information about the higher-order modes of the resonator. Fox-Li analysis is discussed further in Chapter 6.

2.3 GRM Output Coupler

The near- and far-field beam profile of an unstable resonator is affected by the reflectivity profile of the GRM. Two reflectivity profiles have been widely used: the super-Gaussian and parabolic functions.

The super-Gaussian reflectivity profile has the form[70][71][72][73]

$$R(r)_{sg} = R_o \exp\left[-2\left(\frac{r}{w_m}\right)^n\right] \tag{2.11}$$

where R_o is the peak (intensity) reflectivity and n is the order of the super-Gaussian function (for $n = 2$ the super-Gaussian is a Gaussian, and as $n \to \infty$ a top-hat profile results). The variable r denotes the radial distance from the centre of the GRM and w_m is the $1/e^2$ radius of the reflectivity profile.

The parabolic GRM reflectivity profile is given by[74]

$$R(r)_{pa} = \begin{cases} R_o\left(1 - \left(\frac{r}{a_m}\right)^n\right), & -a_m \leq r \leq a_m \\ 0, & \text{elsewhere.} \end{cases} \tag{2.12}$$

where n is the order of the parabolic distribution and can be either 2 or 4. As before, R_o is the peak reflectivity, r denotes the radial distance from the centre of the GRM and a_m is the profile radius. Note that the radial distance from the centre of the GRM, r, can be used for both strip (1-Dimensional) and spherical (2-Dimensional) GRM profiles. Indeed, throughout Chapters 6 and 7 a strip GRM is considered, and r represents the distance from the centre of the 1-Dimensional profile.

The most uniform near-field profile is produced if the peak reflectivity of the strip unstable resonator satisfies the 'maximally flat' condition[63]

$$R_o = \frac{1}{M^{n/2}} \tag{2.13}$$

If the peak reflectance is greater than that in Equation 2.13, then the GRM transmission increases faster than the mode intensity decreases, resulting in a dip in the centre of the near-field. Conversely if the peak reflectance is less than that in

Equation 2.13 the laser can be over-coupled, and the near-field loses uniformity.

The GRM average reflectance for the lowest-order mode in an unstable strip resonator with order n super-Gaussian or parabolic GRM that satisfies the maximally flat condition, using Equation 2.10 is

$$\overline{R} = \frac{R_o}{M} = \frac{1}{M^{\left(1+\frac{n}{2}\right)}}. \tag{2.14}$$

Equation 2.14 implies that, for a given M, the gain-length product required to support lasing increases as the order of the GRM increases. That is, n should be small for low gain systems to enable M to be maximized for a given optimum $\overline{R}$.

2.4 Summary

Table 2.2 gives a comparison of many of the unstable resonator properties discussed in this Chapter, for low and high magnifications. It is clearly beneficial to use a high magnification to utilize the advantages of the unstable resonator, such as the mode good discrimination and a large mode volume. High magnification unstable resonators are also less sensitive to misalignment. Associated with high magnifications, however, is the need for high gain due to the low average reflectance of the output coupler. Many solid-state gain media have inherently low gain. However, the average reflectivity for the lowest-order mode of a strip (1-Dimensional) unstable resonator is a factor of M larger than for the lowest-order mode in a two-dimensional resonator. Also, the ratio of eigenvalues for a particular mode and the next higher-order mode is equal to M regardless of the resonator geometries given in section 2.2. Thus there is no mode discrimination penalty in using the lower-loss strip unstable resonator. A strip unstable resonator typically employs a stable resonator in the orthogonal plane. The implementation of a strip unstable resonator is discussed further in the next Chapter.

Furthermore, Equation 2.14 implies that, the order of the super-Gaussian GRM should be as small as possible for low gain systems allowing M to be maximized for the optimum $\overline{R}$. The average reflectance of the output coupler is, in turn, determined by the laser head and resonator properties. All of these points suggest

	Low Magnification	**High Magnificaiton**
Required gain	low	high
Average reflectance of output coupler	high	moderate
Beam quality: hard-edged o/coupler	low	high
Beam quality: GRM	high	high
Mode discrimination	moderate	high
Dynamic stability	moderate	high
Large mode volume	yes	yes
Excess noise factor	moderate	high

Table 2.2: Comparison of unstable resonator properties with magnification.

that the strip stable-unstable resonator is the most appropriate choice for a low gain, CW solid-state laser.

Chapter 3

Laser Design Summary

From the discussion in Chapter 1, the optimum choice of laser geometry for a *scalable* high-power, CW, solid-state laser would appear to be a side-pumped, side-cooled zigzag slab. The rectilinear slab geometry reduces the problems associated with stress induced birefringence and the zigzag optical path minimizes thermal and stress induced focusing. Furthermore, as will be seen below, the thermal stresses and ease of scalability show the additional advantages of the slab geometry compared with the rod geometry.

Eggleston *et al.*[14] have shown that the ratio of thermal power per unit length which can be absorbed without fracture by a side-pumped, side-cooled slab to that which can be absorbed by a side-pumped, side-cooled rod is given by

$$\frac{(P_h/l)_{slab}}{(P_h/l)_{rod}} = \frac{3}{2\pi}\left(\frac{h}{w}\right) \tag{3.1}$$

where P_h is the thermal power absorbed by the gain medium, l is the length of the gain medium, and w and h are the width (in the pump direction) and height of the slab respectively (see Figure 3.1). They conclude the power handling capability of a slab is greater than a rod if the aspect ratio (h/w) is greater than 2. This further supports the use of a slab geometry for a scalable high power laser gain medium.

The slab geometry is also simple to scale to high powers: since the width of the pumped gain medium and thus the width of the mode in the pump direction is determined by the absorption length for the pump light, the output power can

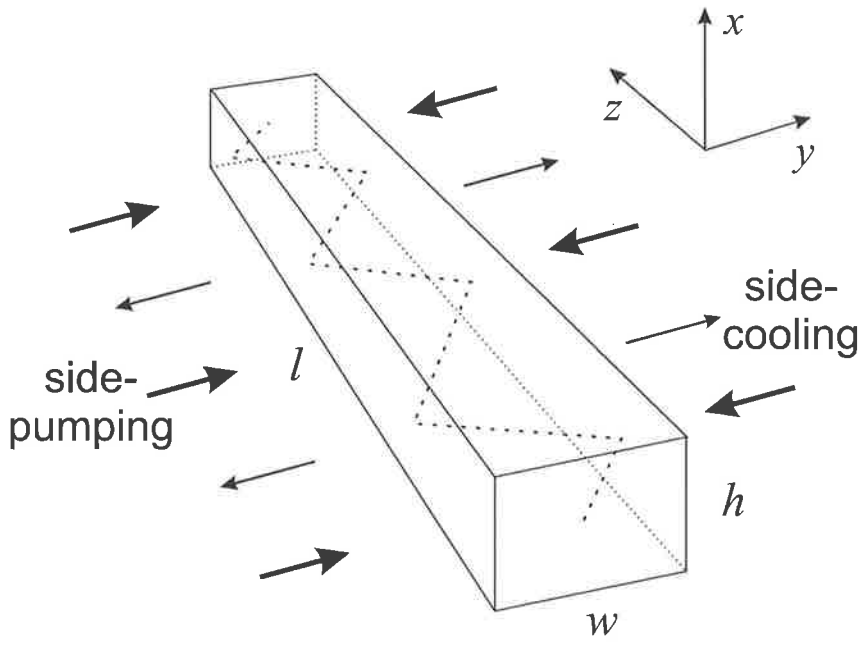

Figure 3.1: Side-pumped, side-cooled zigzag slab geometry. The slab has dimensions of height×width×length ($h \times w \times l$), in the x, y, and z directions respectively.

be increased by increasing the height of the mode or by increasing the length of the gain medium. The mode should zigzag in the plane defined by the pumping (referred to as the horizontal plane here), that is the yz-plane shown in Figure 3.1. This will generally result in a laser mode that has a horizontal width comparable to a mode which might be produced in a stable resonator. Thus the resonator could be designed to be stable in the horizontal direction and unstable in the vertical direction, referred to here as a stable-unstable resonator. Such a resonator would allow the mode cross-section to be scaled in the vertical direction.

The side-pumped, side-cooled zigzag slab geometry should ideally have minimal thermal lensing in the vertical direction. Hence the height of the unstable mode need not vary significantly as it propagates through the gain medium and it should thus have good spatial overlap with a gain region of constant height. Furthermore, since the pumping and heat removal are co-planar, increasing the mode height should not increase the refractive power of either the horizontal or vertical thermal lenses, as the lensing in the horizontal and vertical planes should be de-coupled. This is investigated experimentally in Chapter 5. These features should result in a laser which

produces high beam quality and is relatively insensitive to thermal lens variations.

The advantages of the strip GRM unstable resonator were discussed in Chapter 2. The average reflectance of the output coupler for the lowest-order mode using a strip unstable resonator is a factor of M larger than for a two-dimensional (2-D) toroidal or spherical unstable resonator. Furthermore, there is no mode discrimination penalty in using the strip unstable resonator. The strip stable-unstable resonator therefore allows M to be maximized for low gain CW solid-state systems, thus efficiently utilizing the properties of the unstable resonator. GRM output couplers offer further advantages for a low-gain system, such as good mode discrimination and greater average reflectance than for a hard-edged output coupler.

The remainder of this Chapter gives a description of the choice of solid-state material to be used as the high power gain medium. Equations for the temperature and stress distributions of the side-pumped, side-cooled slab geometry are also presented. These distributions affect the thermal lensing and limit the maximum pump density, which is required for Chapter 6.

3.1 Choice of solid-state material

There are a large number of gain media that lase near 1.06 μm described in the literature. Ideally, the gain media for this work would satisfy the following criteria:

- 4-level laser
- efficient atomic transition
- broad absorption linewidth (greater than diode-laser emission)
- an absorption line which coincides with available high-power diode-lasers
- long upper state lifetime
- narrow emission linewidth
- high absorption efficiency
- high thermal conductivity

Parameter	Value
Nd:Host Material	Nd:$Y_3Al_5O_{12}$ (YAG)
Nd Concentration	1.1 ± 0.1 at.%
Refractive index @1μm	1.8197
Stimulated emission cross-section, σ_{21}	2.8E-19 cm^2 ($^4F_{3/2} \rightarrow {}^4I_{11/2}$)
Spontaneous flourescence lifetime, τ_f	230μs
Thermal conductivity, k	10.39 W/m.K
Absorption wavelength, λ_{abs}	0.808 μm
Absorption linewidth	1.2 nm
Absorption coefficient (†)	4.1 cm^{-1}
Emission wavelength, λ_e	1.064 μm
Tensile fracture strength, σ_f	280 MPa
Youngs modulus, E	282 GPa
Material constant, M_s	3.74 E-6 W/m.Pa
Thermal shock resistance parameter, R_s	1047 W/m
dn/dT	8.9 E-6 K^{-1}
Poisson's ratio, ν	0.3
Stokes factor, η_s	0.76
Thin film convection coefficient, λ_{ht}	1.8 E+4 W/m^2.K
Thermal expansion coefficient, α	6.9 E-6 K^{-1} [75]

Table 3.1: Nd:YAG spectroscopic and thermomechanical parameters from Appendix B, references included in App. B unless cited († measured value).

- high fracture strength
- high optical quality crystals of adequate size available.

No material in the literature satisfies all of these requirements. After significant investigation (see App. B) it was found that while materials with better spectroscopic properties (i.e.: higher absorption coefficient, broader absorption linewidth, etc.) exist, the excellent thermomechanical properties of Nd:YAG are critical for this work. An extensive discussion of the most appropriate material for a high power diode-laser-pumped solid-state laser near 1.06 μm is included in Appendix B. Table 3.1 contains a summary of Nd:YAG material parameters.

3.2 Temperature and stress in slab geometries

This section presents formulae for the temperature and stress distributions for the side-pumped, side-cooled slab gain media.

3.2.1 Slab temperature distribution

The temperature distribution in a uniformly side-pumped, side-cooled slab of infinite height and length with constant heat input per unit volume, Q, is given by[14]

$$T(y) = T_c + \frac{Qw_p}{2}\left(\frac{1}{\lambda_{ht}} + \frac{w_p}{6k}\right) + \frac{Qw_p^2}{8k}\left[\frac{1}{3} - \left(\frac{2y}{w_p}\right)^2\right] \tag{3.2}$$

where w_p is the width of the slab in the y-direction (as shown in Figure 3.1), λ_{ht} is the thin film convection coefficient, a parameter that defines the heat extraction efficiency of the coolant from the surface it flows past, T_c is the coolant temperature and k is thermal conductivity of the gain medium, which is assumed to be temperature independent.

3.2.2 Slab stress

The surface stress for a uniformly side-pumped, and side-cooled slab of infinite height and length is given by[14]

$$\sigma_s = Q\frac{1}{12}\frac{\alpha E}{k(1-\nu)}w_p^2 = \frac{Q}{12M_s}w_p^2 \tag{3.3}$$

where α is the thermal expansion coefficient, E is the Young's modulus, k is the thermal conductivity, ν is Poisson's ratio, w_p is the width of the slab, and M_s is the material constant, which is discussed below. All parameters are assumed to be temperature independent.

The heat generated by the absorbed pump light, P_p, is given by $P_h = (1\text{-}\eta_s)P_p$, where η_s is the Stokes factor. The heat absorbed per unit volume, Q, is given by $(P_h/w_p h_p l_p)$.

The material constant M_s can be written as $M_s = R_s/\sigma_{\text{max.}}$, where R_s is the thermal shock resistance parameter and $\sigma_{\text{max.}}$ is the maximum surface stress at fracture (sometimes denoted σ_f), which is strongly dependent on surface polish quality[76]. Therefore Equation 3.3 can be written as

$$\frac{P_h}{l_p} = 12\left(\frac{\sigma_s}{\sigma_{\text{max.}}}\right) R_s \left(\frac{h_p}{w_p}\right) \tag{3.4}$$

Equation 3.4 gives the heat per unit length for a given percentage of the stress fracture limit ($\sigma_s/\sigma_{\text{max.}}$). The scalability of slab lasers is thus predominantly limited by the thermomechanical properties of the crystal, which determine σ_s, and the maximum size of the large aspect ratio Nd:YAG slabs that can be grown and polished[77][78] while maintaining low losses and low wavefront distortion.

Chapter 4

Laser Design

A stable-unstable resonator with useful mode discrimination has relatively large output coupling, which necessitates high gain. A high gain-length product can be produced by using a single layer of closely packed pump fibres. However, the pump density must be chosen such that the surface stress is below the stress fracture limit of the gain medium. If the pump density causes the surface stress to approach the stress fracture limit of the gain medium, the spacing between the fibres could be increased thus decreasing the surface stress. However this also decreases the small-signal gain coefficient. The alternative is to increase the pathlength within the gain region. However, this also increases the path-integrated loss which decreases the efficiency. The laser head described in this Chapter attempts to maximize the gain-length product while maintaining a realistic surface stress, to achieve the gain-length product required for efficient operation of a $M = 1.3$ stable-unstable resonator.

The co-planar side-pumping and side-cooling of the laser head design described in this Chapter, presumes that the mode volume can be scaled by adding layers of pump fibres in the vertical direction. If the pump density remains constant then the gain-length product and the loss should also remain constant, but the mode volume increases and the laser power should subsequently increase. This scalability requires the zigzag optical path to minimize the thermal and stress induced focussing, this is investigated in Chapter 5.

4.1 Slab crystal geometries

Slab gain media are normally operated in one of two ways: either the laser mode passes straight through the gain media, or it follows a Total Internal Reflection (TIR) path within the slab (usually a zigzag path). As discussed in the previous Chapter, a zigzag path within the slab, can be used to minimize thermal and stress induced biaxial focussing[14]. The zigzag path also has the advantage of increasing the pathlength within the crystal, thereby increasing the gain-length product, $g_o l$, and improving the efficiency. Zigzag slab lasers are normally designed so the laser mode enters and leaves the crystal at Brewster's angle to the crystal faces, thereby producing a linearly polarized mode and removing the need for anti-reflection coatings[15][23]. These advantages lead to the popular zigzag slab configuration which is considered here in more detail for some different crystal shapes.

A popular implementation of this idea is the single pass geometry shown in Figure 4.1, which has been successfully used by numerous authors [15][16][18]. This crystal geometry can be simply inserted into an optical cavity. However, a folded version of this crystal has a larger pathlength within the gain medium and can yield a more compact resonator. Such a slab geometry, shown in Figure 4.2, has been developed by Richards and McInnes[23] in a side-pumped, bottom and top conductively cooled Nd:YAG slab. They demonstrated high CW multimode slope efficiency (57%). In a stable laser resonator the demonstrated 35% multimode efficiency and 25% efficiency for a near Gaussian beam with $M^2 = 1.2$ (from 18.3 W of diode-laser pump power, after a collimating optic). The efficient energy extraction of this crystal design is attractive for the high-power laser application here. Furthermore, efficient operation of this laser crystal geometry has been verified in a stable ring resonator and the multimode lasing and frequency noise of the free-running laser has been suppressed by injection locking[79][80][81]. The disadvantage of this geometry for use in a ring resonator is that the incident and transmitted beams are separated by a small angle, especially for a high TIR bounce angle, θ_1. Irrespective, the crystal geometry shown by Figure 4.2 was chosen for the work in this thesis.

The geometry, as shown in Figure 4.3, was investigated because of the larger angle between the incident and transmitted beams, with the mode still incident

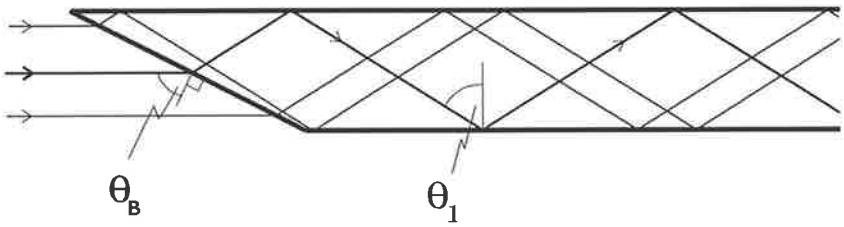

Figure 4.1: Single pass TIR zigzag slab geometry (θ_B is Brewster's angle, θ_1 must be larger than the critical angle for TIR).

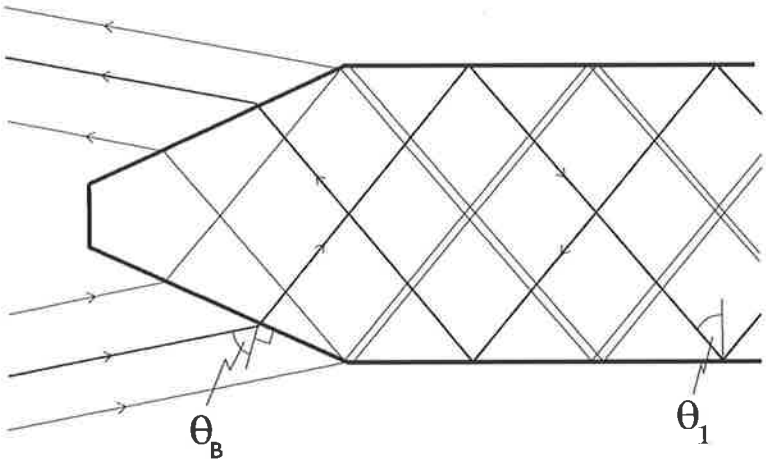

Figure 4.2: Folded TIR laser crystal.

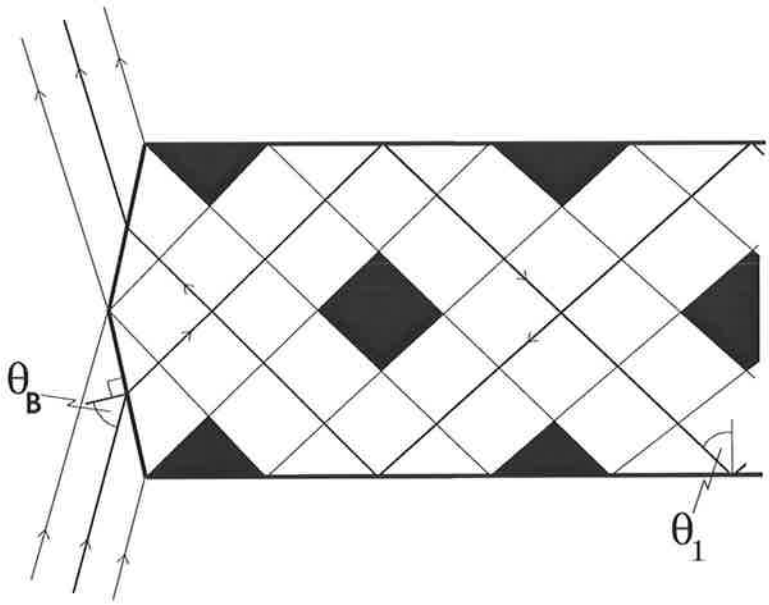

Figure 4.3: Alternative folded TIR design, the geometric area not transversed by a geometric beam is in black.

at Brewster's angle. The design was abandoned because of poor energy extraction efficiency discussed in this paragraph. With this crystal design the area shaded in black is not transversed by a collimated beam. The fraction of area unshaded compared to the total area is an estimation of the geometric energy extraction efficiency of the laser mode, $\eta_{g\varepsilon}$, and for Figure 4.3 is given by

$$\eta_{g\varepsilon} \simeq \frac{\cos(2\theta_1 - \theta_B)\tan(90 - \theta_1)}{2\cos(\theta_B - \theta_1)\cos\theta_1} \tag{4.1}$$

where θ_B is Brewster's angle. This relationship is independent of the width of the crystal. For side-water cooling, θ_1 must be greater than 47.0° for which $\eta_{g\varepsilon} = 59\%$ (i.e.: the area in black would be 41%). Furthermore, $\eta_{g\varepsilon}$ decreases with increasing θ_1. Therefore this would be a poor crystal geometry choice for a side-pumped, side-cooled slab. The energy extraction efficiency of the slab can be increased to 100% by making the entrance/exit face flat, that is using a rectilinear slab, the aperture is then the full width of the slab. While this geometry would also give a large angle of separation between the incident/exit modes, Brewster's angle can no longer be used as the angle of incidence. Furthermore, the end faces require specific AR and HR coatings, and parasitic modes will oscillate in the perfectly rectangular structure of the slab. Again, for simplicity the geometry shown in Figure 4.2 is used, with 100% energy extraction efficiency and no intracavity coatings.

4.2 Laser head construction

This section describes the laser head design.

4.2.1 Laser crystal design

Technical drawings for the Nd:YAG crystal used in this thesis based on the design in Figure 4.2 (purchased from Litton Airtron SYNOPTICS[1]) appear in Appendix C. The slab has a width, w, of 3.0 mm, a parallel-side-length of 32.3 mm and an

[1]Litton Airtron SYNOPTICS, 1201 Continental Boulevard, Charlotte, NC 28273, USA.

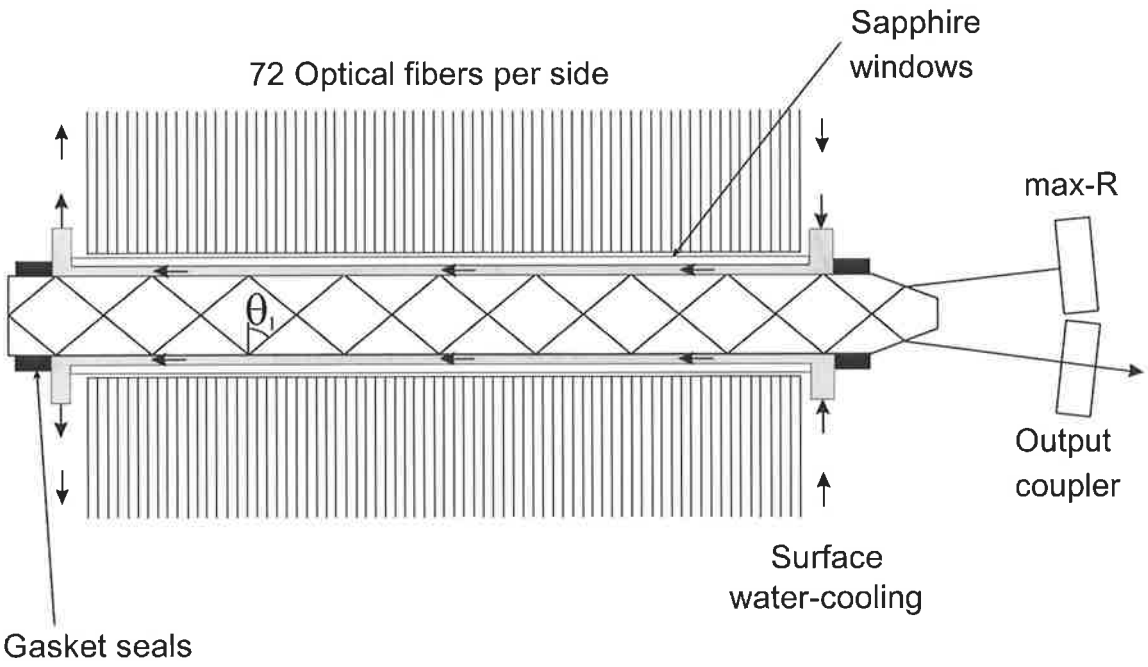

Figure 4.4: Schematic diagram of the fiber-coupled diode-laser pumping scheme (top view) showing the zigzag path of the laser mode. θ_1 is the TIR bounce angle, 51°.

overall length of 34.7 mm. The TIR angle θ_1 of 51° giving 19 reflections is shown by Figure 4.4. The TIR angle allowed conductive water side-cooling of the slab. The slab was pumped by fibre-coupled diode-lasers. The length of the pumped region, l_p, was determined by the number of optical fibres along the pump-faces of the slab and the space for water seals at the end of the array of optical fibres (see Figure 4.4).

The height of the slab was chosen to be 3.4 mm, approximately 3 times greater than the height of the pump region, as shown in Figure 4.5. The excess height should be minimized so as not to complicate temperature control. A compromise of an aspect ratio of 1.11 was chosen for the proof-of-principle experiments. This aspect ratio is less than the value of 'greater than 2' described in Chapter 3 for good power handling capability. If the height of the mode volume is increased then a larger aspect ratio slab should be used.

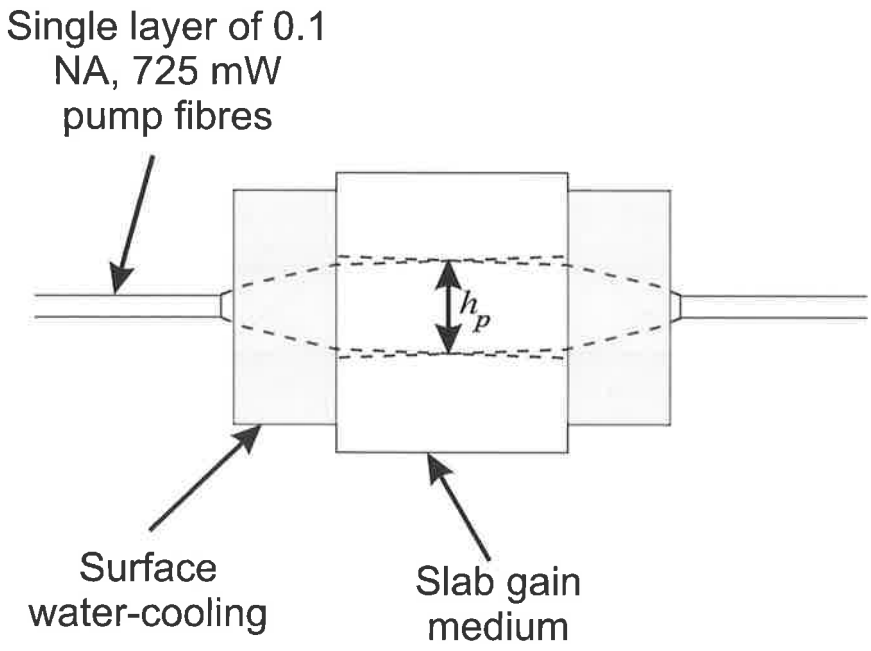

Figure 4.5: End view of the pumped slab. h_p is the height of the pumped region in the slab. A single layer of 0.1 NA, 725 mW pump fibres each side giving 52 W of pump power.

4.2.2 Laser head

A cross-section of the laser head is shown schematically in Figure 4.6, and a photograph of the end-view is included as Plate # 1. The Nd:YAG crystal is side-pumped and side-cooled. Side-cooling is achieved by water, flowing along the sides of the crystal (flow direction orthogonal to the page). The slab sides were coated with Teflon AF 1600,([2]) described later in section 4.2.3, to prevent the gasket water seals from disrupting the TIR. Water was contained at the outer edge of the water channel by an AR-coated sapphire window with dimensions 25.0 mm × 8.0 mm × 0.5 mm thick. Two gasket seals maintain the water channel: a main seal placed between the aluminium body of the laser head and the laser crystal and a second seal between the laser head body and the sapphire window. Ideally, in this configuration the heat deposited by optical pumping and the heat removal will be co-planar; thus minimizing the thermal and stress induced focussing.

[2]TEFLON® AF is an amorphous fluoropolymer developed by Du Pont Polymers, P.O. Box 80713, Wilmington, DE 19880-0713, U.S.A.

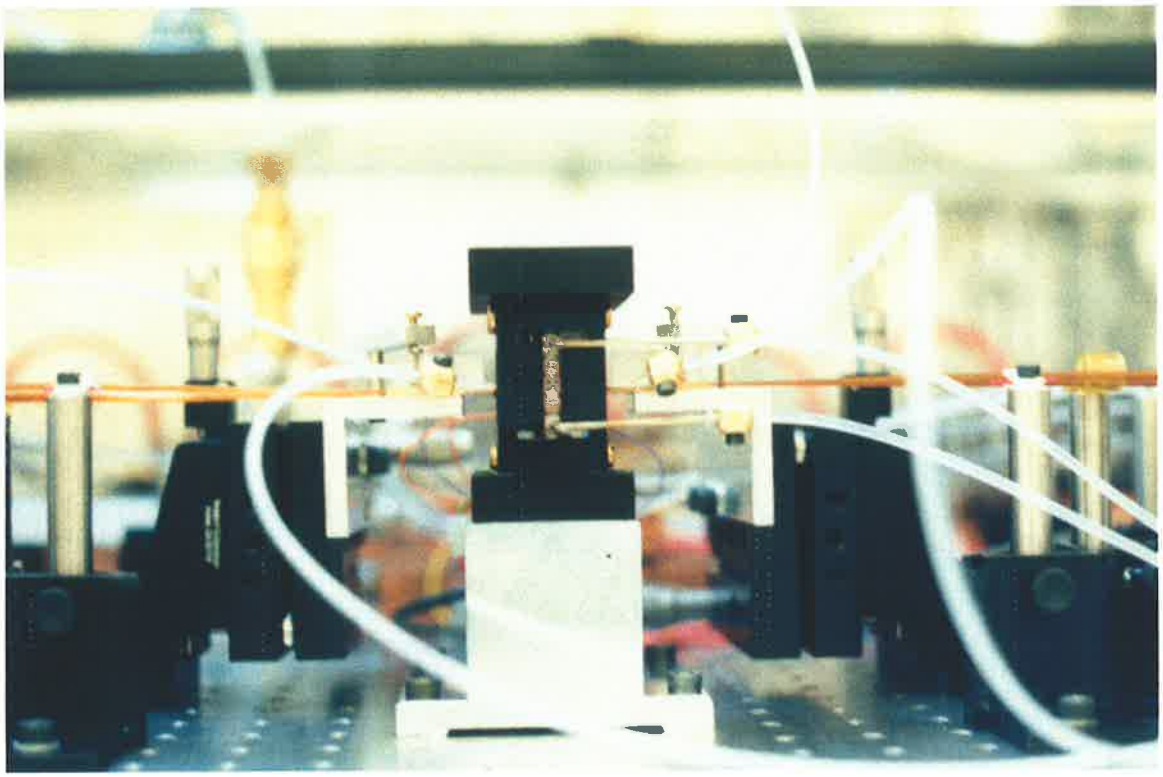

Plate # 1

End view of the laser head showing the TEC's and heatsink's below and above the Nd:YAG slab. The optical fibres used to side-pump the slab are also shown.

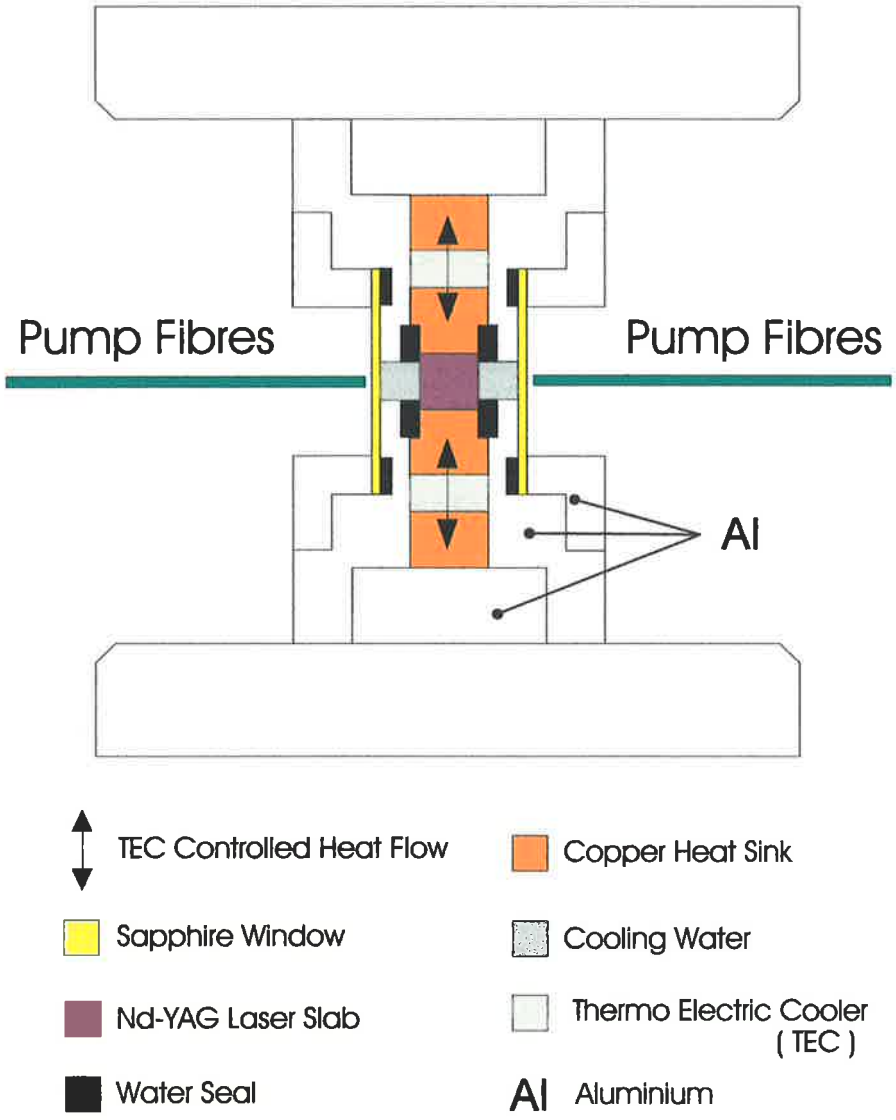

Figure 4.6: Schematic diagram of the laser head geometry used to hold and cool the Nd:YAG crystal (drawn by B. Middlemiss).

The slab is pumped on both sides using fibre-coupled diode-lasers. Each diode-laser bar is coupled to twenty-four 250μm-core (275μm outer diameter), 0.1 NA step-index fibers (Opto Power diode-lasers, model OPC-A015-808-FC). The low numerical aperture of the optical fibres allows arrangement of the pump sources to produce a high pump density without the need for complex focussing optics. Fibre-coupling the diode-lasers also removes them and their temperature control systems from the vicinity of the gain medium, thus reducing the complexity of the laser head[5]. Each fibre supplies a maximum of 725 mW of pump power, giving a total pump power of 104 W. Each diode-laser was individually wavelength tuned to the absorption peak of Nd:YAG by changing the diode-laser temperature, using Thermo-Electric Cooler's (TEC's) and feedback control systems. A schematic diagram of the diode-laser cooling arrangement and feedback systems is included in Appendix D.

The combination of the small fibre core diameter, low NA and refraction as the pump light is transmitted through the sapphire window into the cooling water and on into the Nd:YAG crystal results in a thin, almost collimated slice of pumped gain region from each layer of fibres. Only pumping the central region of the slab means the cavity modes can efficiently extract gain without obscuration by apertures in the vertical plane. If the pump fibre-end is 0.5 mm from the sapphire window, the pump radiation passes through a 0.5 mm sapphire window and then 2 mm of water, it will then have a full width of 0.8 mm at the near face of the slab and 1.1 mm at the far face. The pump-density can be adjusted by varying the packing density of the optical fibres. A photograph of the arrays of pump fibres without the laser head is included as Plate # 2.

As the pumped region is about 1.1 mm high and the side-cooling is 1.5 to 2.0 mm high, a thermal gradient in the vertical direction could be expected. This is due to cooling at the bottom and top of the water channel where there is no pump radiation, therefore cooling the crystal regions below and above the pumped region. This is quite different from the uniformly face-pumped, uniformly face-cooled slab model discussed in Chapter 3. To counteract the non-uniform face-pumping and cooling, heat is added to the top and bottom surfaces using the TEC's as described earlier.

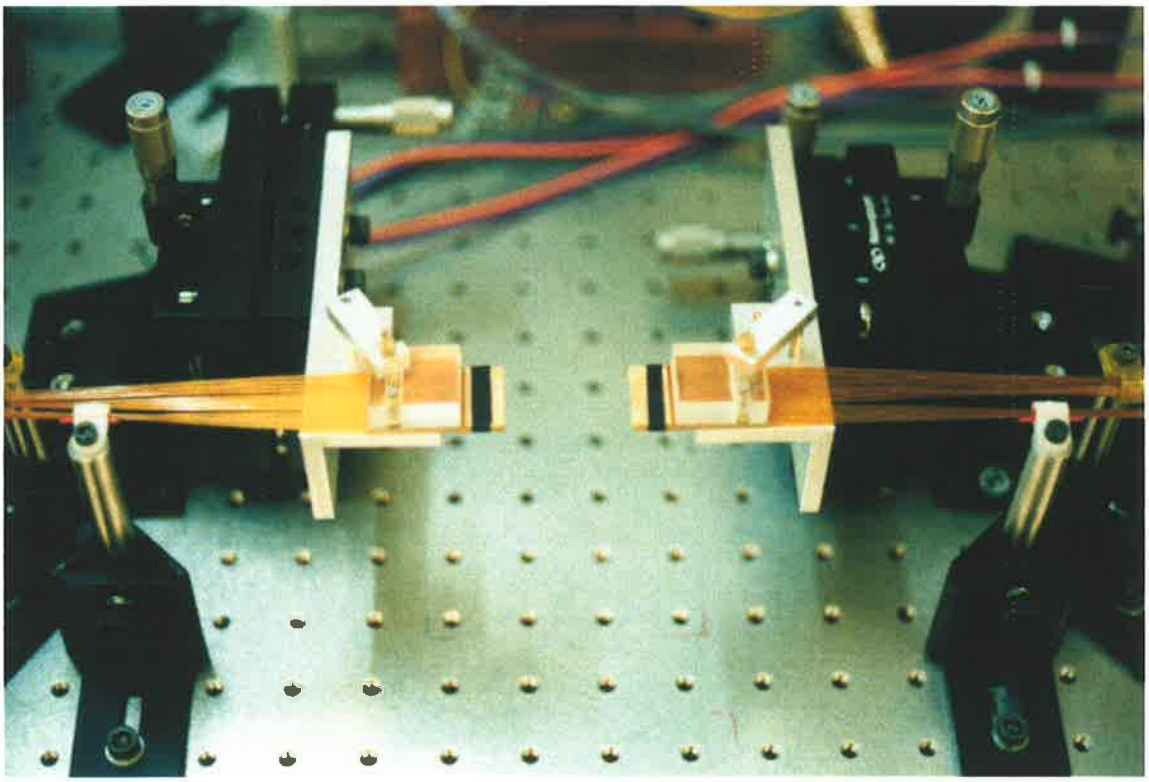

Plate # 2

Arrays of pump fibres (72 per side) with the laser head removed.

TEC's on the bottom and top of the slab, are located between two copper heatsinks. The dimensions of the TEC's were 29.6 mm × 4.1 mm × 3.2 mm thick (Marlow Industries SP1614, $Q_{max.} = 4$ W, $I_{max.} = 0.9$ A, $V_{max.} = 6.5$ V). The copper heatsink in contact with the slab had a thermistor mounted in a hole drilled along the long axis to enable a constant temperature to be maintained at the bottom and top of the slab using a feedback control circuit similar to those used for controlling the temperature of the diode-lasers (see App. D). The outermost copper heatsinks were water cooled. Indium foil was placed between layers to ensure good thermal contact.

This laser head configuration thus has horizontal pumping and cooling and vertical temperature control. Manipulation of the temperature of the bottom and top surfaces of the slab has been demonstrated previously using chill bars[21] to cool or edge bars[22] to heat the bottom and top surfaces. However, the advantage of TEC's is they have the ability to heat or cool the bottom and top surfaces. This enables the focal length of the vertical thermal lens to be increased or decreased, as will be demonstrated in Chapter 5.

The laser head was designed by the author and Mr. B. Middlemiss of the optics group, who subsequently manufactured the prototype laser head that was used for the experiments in this thesis.

4.2.3 Teflon coating

As mentioned earlier, the parallel TIR sides of the slab were coated with a fluoropolymer, Teflon AF 1600, to prevent wavefront distortion by the gasket water seals[16]. A 4% Teflon AF: 96% FC-75 solution was used to coat the slab sides (FC-75 is a solvent for Teflon AF)[3]. The solution is applied to the slab sides; after a few minutes the FC-75 evaporates leaving a thin film of Teflon. The Teflon coating has a refractive index similar to that of water, and has low absorption at 0.808 μm and at 1.064 μm. However, the Teflon coating has relatively poor thermal conductivity, which increases the slab average temperature. Care must therefore be taken when

[3]The author gratefully acknowledges the assistance of T. Rutherford and W. Tulloch at Stanford University, CA, for help with the application of Teflon to laser slabs.

applying the Teflon solution, as thin coatings allow more efficient heat extraction from the crystal by the water-cooling. The coating thickness was estimated to be 15 ± 5 μm.

4.2.4 Water cooling systems

Cooling of the laser system is achieved with two separate systems, one to cool the laser head and the other to cool the pump diode-lasers.

Laser head cooling system

The water cooled laser head requires clean, flowing, temperature stabilized water. Since the long-term aim is to injection lock the laser to produce a reliable single-frequency laser, it was decided to initially minimize the water vibrations associated with water pumps by using a gravity fed water system.

For efficient heat removal from the slab, the water flow in the channels must be turbulent (rather than laminar). To determine if the flow is turbulent, the Reynolds number (RN) may be evaluated[82]

$$RN = \frac{\rho v_f d}{\xi} \tag{4.2}$$

where ρ is the fluid density (1 x 10^3 kg/m^3 for water), v_f is the fluid speed, d is the diameter of a tube and ξ is viscosity (1.0 x 10^{-3} N.s/m^2 for water at 20°C). If $RN < 2{,}000$ the flow is usually laminar, whereas for $RN > 3{,}000$ the flow is usually turbulent[82]. Assuming the 1.5 mm $\times$ 2 mm water channel at the slab edge is a circular tube with the same cross-section, then for a water flow rate of 300 ml/minute, the RN is approximately 3,250.

To verify Equation 4.2 gives a realistic estimate of the type of flow, the inlet pressure as a function of water flow through the laser head was measured. The results are shown in Figure 4.7. The data below and above 550 ml/minute were fitted using independent linear fits of those data sets. This shows a distinct inflection between 500 and 600 ml/minute indicating the flow is changing from laminar to

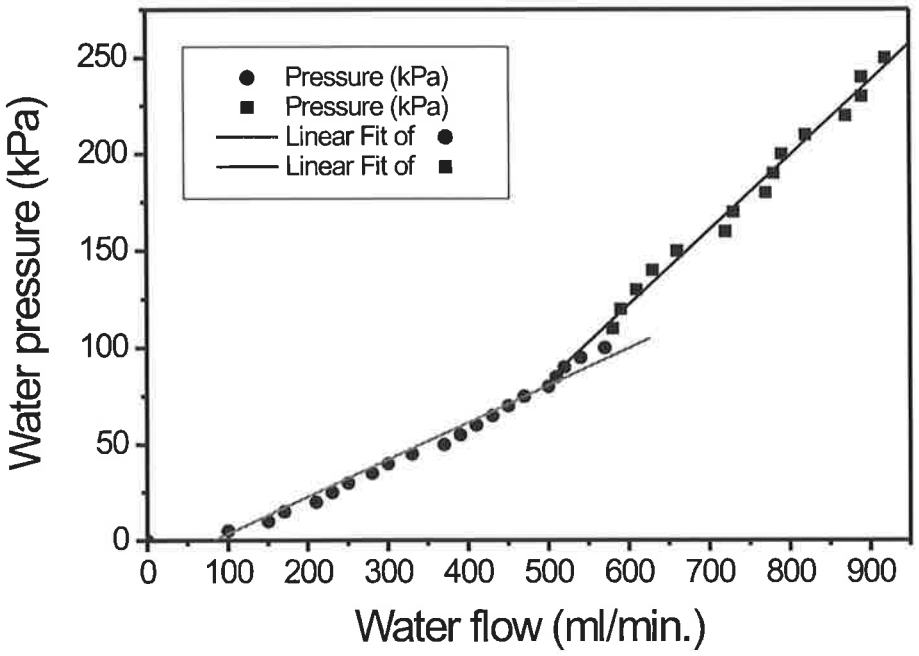

Figure 4.7: Water flow through the laser head, linear fits of the data above and below 550 ml/min. are given.

turbulent, which agrees with the calculation above, where flow rates greater than 600 ml/minute are turbulent.

A schematic of the gravity fed cooling system is shown in Figure 4.8. It was constructed using chemically inert tanks and tubing, to avoid contamination of the cooling water. The tank was located 12 m above the laser head producing sufficient pressure ($\approx$120 kPa) for the desired flow rate through the laser head (0.3 l/min on each side). The water was returned from the bottom tank to the top tank using a pump that was controlled by a 2-pole float switch in the bottom tank. The pump operated for several minutes every hour.

The temperature stabilization system consisted of an immersion heater and a TEC heat exchanger (items A and B in Figure 4.8). The immersion heater (A) consisted of a temperature sensor, a heating element and a feedback circuit controlling a solid-state switch to turn the heater on and off. It's purpose was to provide coarse

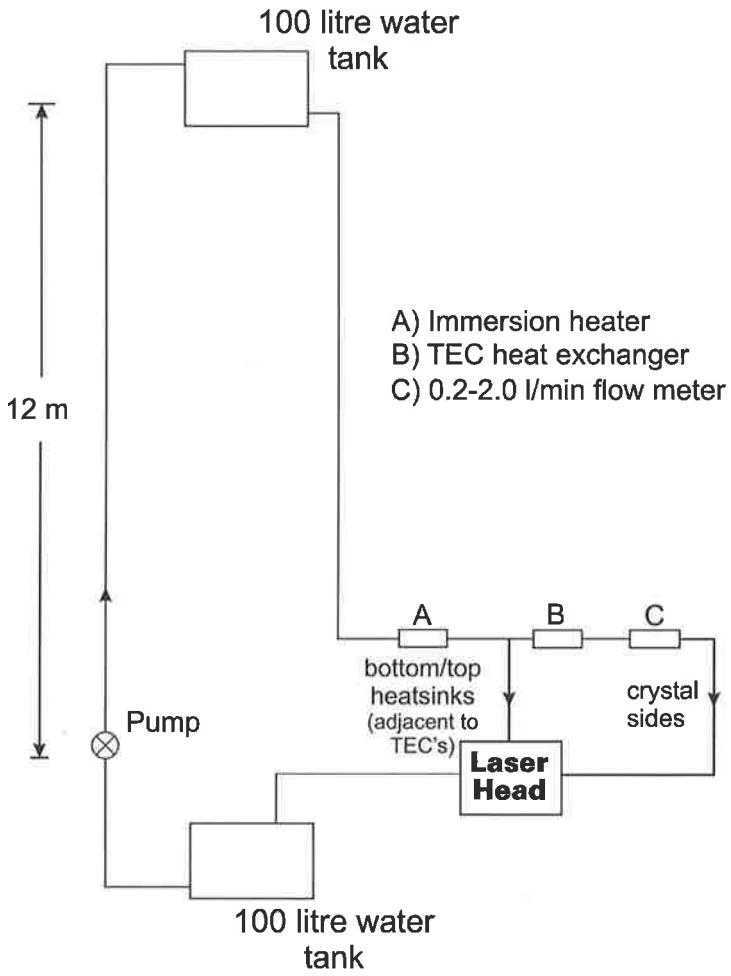

Figure 4.8: Schematic of the temperature stabilized laser head water cooling system.

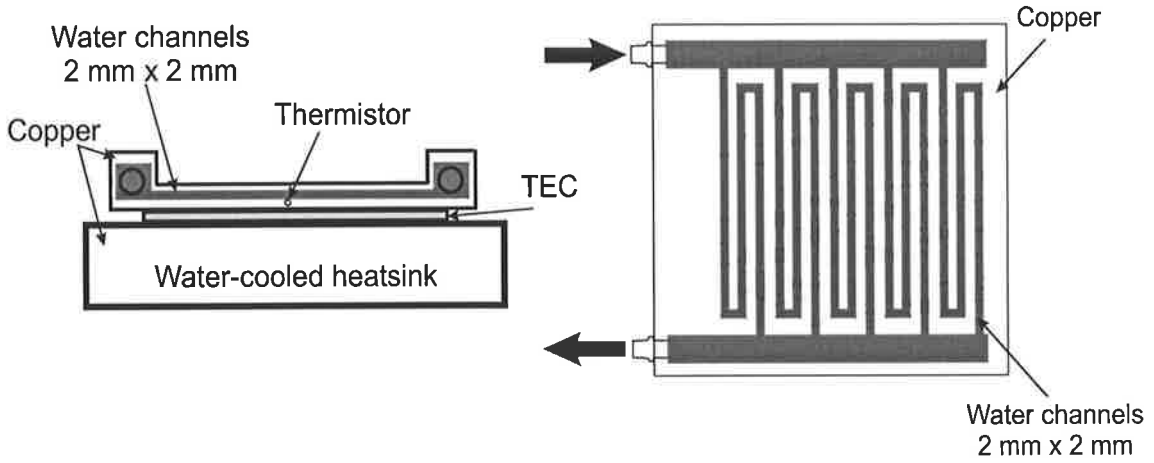

Figure 4.9: Fine control heat exchanger (left) consisting of a water-cooled heatsink, TEC, thermistor and heat exhanger element. A top view of the heat exhanger element (right) shows several 2 mm × 2 mm water channels in parallel.

heating of the cooling water to within ± 1°C of the desired temperature (chosen to be 25°C). This stage was followed by a TEC heat exchanger (B) for fine control of the water temperature. The water flowed through small water channels within a copper block that was in contact with a TEC (Melcor, model # CP 2-127-06L), as shown in Figure 4.9. The TEC was controlled by a feedback system (similar to the circuit for the diode-laser cooling systems, see App. D). This provided fine tuning of the water temperature and resulted in a temperature of 25 ± 0.3°C. The absolute temperature of the water is not particularly important, however the inlet water temperature must be constant. If the water temperature changes then the average temperature of the slab will change, thus changing the length of the slab and the frequency of the laser.

Diode-laser cooling system

The diode-lasers were mounted on heatsinks, illustrated and described in Appendix D. The water cooled heatsinks were cooled with water circulating through an industrial chiller system, water temperature of 15°C. A photograph of the diode-laser cooling arrangement is shown in Plate # 3. The six 20 W diode-lasers were individually temperature stabilized to better than ± 0.1°C with full heat load (60-80 W per diode-laser). The wavelength of the diode-lasers were selected experimentally

by changing the set point temperature for maximum absorption of the pump light by Nd:YAG.

4.3 Resonator configurations

The laser head design can be used in both standing- and travelling-wave resonator configurations. If flat mirrors are placed close to the Brewster angled surfaces, as shown in Figure 4.4 and in Plate # 4, then the resonator is stable and multimode operation results, assuming that there is a positive weak horizontal and vertical thermal lens. Moving the mirrors away from the slab end increases the size of the fundamental mode and eventually the higher-order modes will be extinguished in the horizontal plane due to the crystal apertures. Single mode operation in the vertical direction can be achieved by controlling the thermal lens in the vertical plane. This is demonstrated in Chapter 5.

This laser head could also be used in a travelling-wave (or ring) configuration. In the example shown in Figure 4.10, a dielectric coated prism is used to reflect the narrowly separated beams from the crystal end, to resonator mirrors. This configuration maintains small angles of incidence on the resonator mirrors and allows simple adjustment of the resonator length by increasing the separation of the mirrors. Depending on the choice of curvatures of the max-R mirror and GRM output coupler, the resonator could be either stable or unstable in the vertical direction. The mode-control lens is included to provide control of the horizontal mode.

4.4 Summary

The gain medium described in this Chapter is a side-pumped, side-cooled zigzag Nd:YAG slab in which the laser mode enters and exits at Brewster's angle through the same end of the crystal resulting in an efficient and compact laser[23]. The horizontal aperture of this slab is significantly smaller than the horizontal aperture of a single-pass zigzag slab (see Figures 4.1 and 4.2) of the same width. Therefore, it is easier to achieve single transverse fundamental mode operation in this plane with short resonators. The slab design also lends itself to operation in a standing-

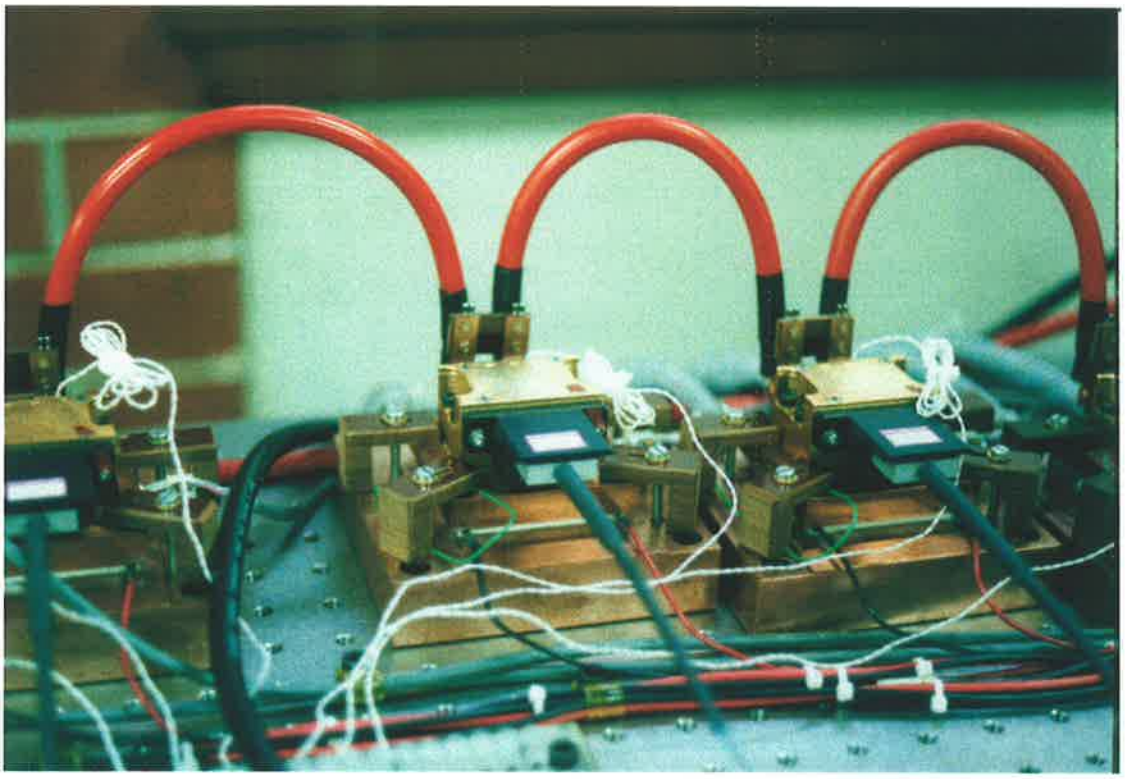

Plate # 3

Fibre-coupled diode-lasers mounted on individual temperature controlled heatsinks.

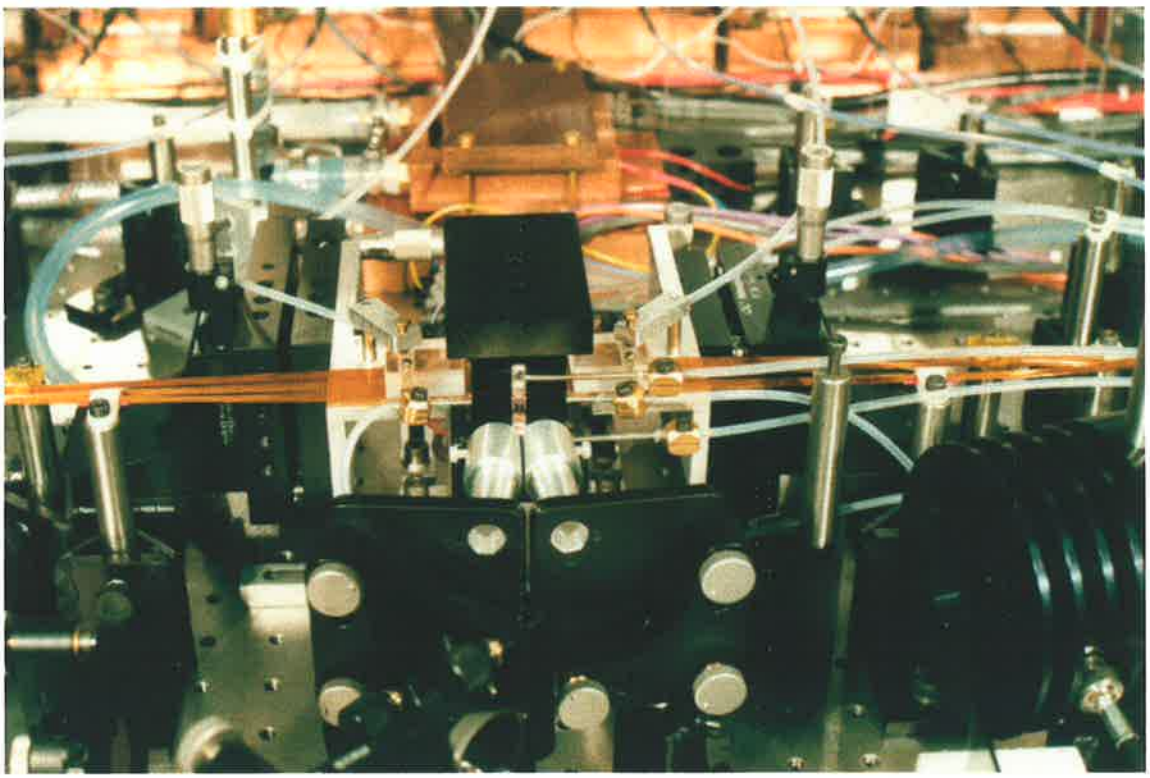

Plate # 4

Laser head setup with a short multimode resonator.

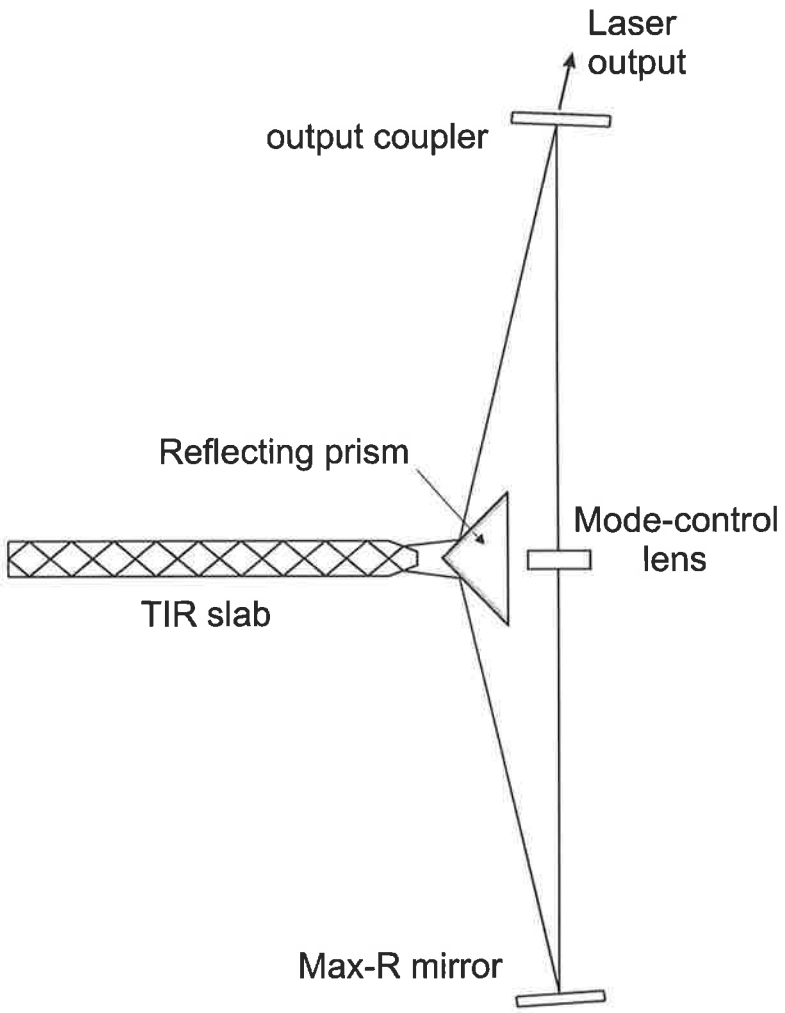

Figure 4.10: Example of a travelling-wave (or ring) resonator configuration.

or travelling-wave configuration. Plate # 5 shows a photograph of the overall laser setup with the diode-lasers, optical fibres, laser head and an interferometer for laser slab diagnostics (see next Chapter).

The next Chapter investigates experimentally the characteristics of the laser head, including the single-pass gain and loss of the slab, and the effect of the active control of the temperatures of the bottom and top of the slab. The optimum output coupler is determined and the efficiency of the multimode and single transverse fundamental mode operation is investigated.

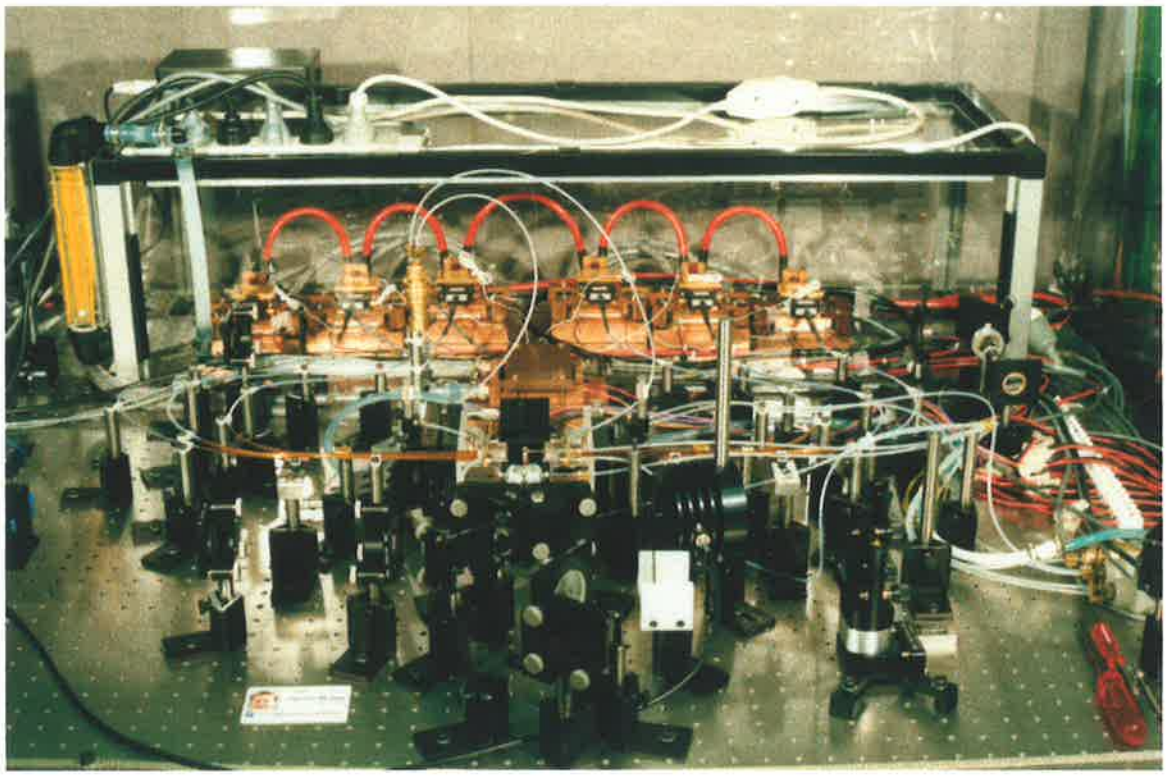

Plate # 5

Overall laser setup showing the diode-lasers, laser head and a Mach-Zehnder interferometer for characterization of the gain medium.

Chapter 5

Characterization of Laser Head

The experiments in this Chapter investigate

- the single-pass gain and loss of the slab,
- the active control of the temperatures of the bottom and top of the slab using TEC's,
- the effect of heating and cooling the bottom and top of the slab on the focal lengths of the horizontal and vertical thermal lenses, and
- the optimum output coupling and efficiency of multimode and single transverse fundamental mode stable resonators.

The results of these experiments show that the behavior of the laser head suits the stable-unstable resonator concept. In particular, the vertical thermal lens can be set as required, and the horizontal and vertical thermal lens is de-coupled which allows the mode height (in the vertical direction) to be scaled without changing the properties of the horizontal, stable resonator. This allows scalability of the laser head.

5.1 Slab loss

Loss within the slab gain medium occurs due to two mechanisms: scatter from bulk crystal imperfections, thermal aberrations and material impurities; and scatter due to micro-roughness of the TIR sides.

Cited TIR loss/bounce	0.1 - 0.2% [16]
Number of TIR bounces	19
Total predicted TIR loss	2.85% [assuming 0.15% loss/bounce]
Cited bulk scatter loss	0.0015 cm^{-1} [83]
Pathlength in crystal	9.05 cm
Total predicted pathlength loss	1.81%
Total predicted scatter loss	4.66%

Table 5.1: Crystal loss prediction.

To assess the quality of the TIR slab used in these experiments, the single-pass loss was measured. For the measurement, the two parallel sides of the 19 TIR bounce Nd:YAG slab were coated with a 3-4% Teflon solution and the crystal was unclamped. A low power π-polarized beam from an Non-Planar Ring Oscillator (NPRO) Nd:YAG laser was used as the probe beam. The beam diameter at the entrance/exit faces was approximately 400 μm, one third of the effective aperture created by the Brewster angled faces, thus avoiding clipping loss. The transmitted laser power (after transversing the crystal) was compared to the incident power. Detection using thermal power meters was too inaccurate, as air currents in the room produced large variations in the measurement of power. Instead a photodiode (model OSD15-5T, active area of 15 mm^2) and amplifier circuit was used. The probe laser beam was chopped (200 Hz) to provide a zero reference and the output of the photodiode circuit measured by a digital CRO. The loss was estimated to be 3% $\pm$ 1%.

The large magnitude of the error was due to poor stability of the source (beam wander and power drift). The measured loss is compared to a predicted loss using values cited in the literature, in Table 5.1. This indicates the crystal quality is probably quite high, since the measured value is less than the total predicted scatter loss.

5.2 Gain

The single-pass small-signal gain factor was measured while pumping only one side of the slab (total pump power 52.2 W) to avoid strong thermal lensing of the probe beam. The single-pass small-signal gain factor can be related to the small-signal

gain coefficient (g_o) by the following equation

$$\mathrm{G} = \exp[g_o l_g] \tag{5.1}$$

where l_g is the geometric pathlength in the crystal.

Figure 5.1 shows the dependence of the measured gain on the height of the pumped region. It also shows the gain predicted using Equations 5.1 and E.2 (see App. E for small-signal gain formula), and Table 5.2. The height of the gain region increased as the fibre array was moved away from the slab. This allows the pump light to diverge more before it enters the slab, thus increasing the height of the gain region, and decreasing the inversion density. The height of the gain region was estimated by considering the solid angle of the pump light, given by the numerical aperture (NA) of the pump fibres. The refraction of the pump light travelling through air, sapphire, water and Nd:YAG, allows the height of the pumped region in the slab to be estimated. There is good correlation between the shape of the measured and calculated curves. The systematic offset most likely arises from the fact that Equation 5.1 does not include the x-dependence of the Gaussian pump profile distribution. The predicted value assumed the pump light was evenly distributed over the pump height, the x-axis variable in Figure 5.1. This approach gives an on-axis gain lower than would be expected given the pump profile inhomogeneity in the vertical plane. Thus the predicted gain should be lower than the measured gain, as illustrated by Figure 5.1.

There were several tasks during this thesis including the above, where a low power 1 μm alignment or probe laser was required. A purpose-built, compact, air-cooled laser was constructed for these applications. A brief description of this laser is given in Appendix F.

Parameter	Value
Pumped width, w_p	3.0 mm
Pumped height, h_p†	1.0 mm
Pumped length, l_p	20.0 mm
Total pathlength in crystal	0.0905 m
Water channel width	2.0 mm
Pump fibre diameter	275 μm
Pump fibre N.A.	0.1
Pump power/fibre	725 W
Number of pump fibres	144
Total pump power	104.3 W
Absorption coefficient @808 nm ‡	4.1 cm^{-1}
Estimated total absorbed pump power, P_p	73.8 W
Absorption wavelength, λ_{abs}	0.808 μm
Emission wavelength, λ_e	1.064 μm
Total slab height	3.4 mm
Slab dimensions	see App. C
Stimulated emission cross-section, σ_{21} ($^4F_{3/2} \rightarrow {}^4I_{11/2}$)	2.8 E-23 m^2
Spontaneous fluorescence lifetime, τ_f	230 μs
$h\nu_l$	1.8694 E-19 J
Quantum efficiency, η_q	0.95
Stokes factor, η_s	0.76
$\eta_{tot} = \eta_q \eta_s$	0.722
Multimode beam overlap efficiency, η_B ◇	0.85 [83]
Small-signal gain, g_o	23.65 m^{-1}
Pathlength in gain region, l_g	0.05147 m
Gain-length product, $g_o l_g$	1.2169
Slab pump volume, V	6.6E-8 m^3
Mode cross-sectional area, A_m	1.28E-6 m^2
Saturation intensity, I_s	2.903E+7 W/m^2

Table 5.2: Quantities used for gain modelling († minimum pump height, ‡ measured, ◇ average of 0.8 - 0.9).

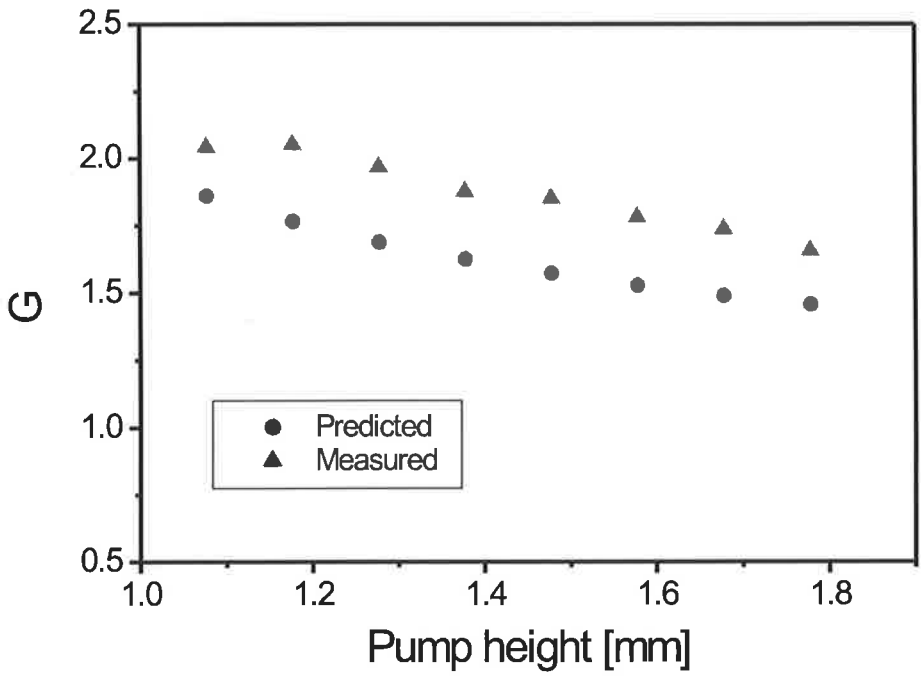

Figure 5.1: Single-pass, small-signal gain factor dependence on the height of the pumped region at the far side of the slab (one fibre array only, pump power 52 W).

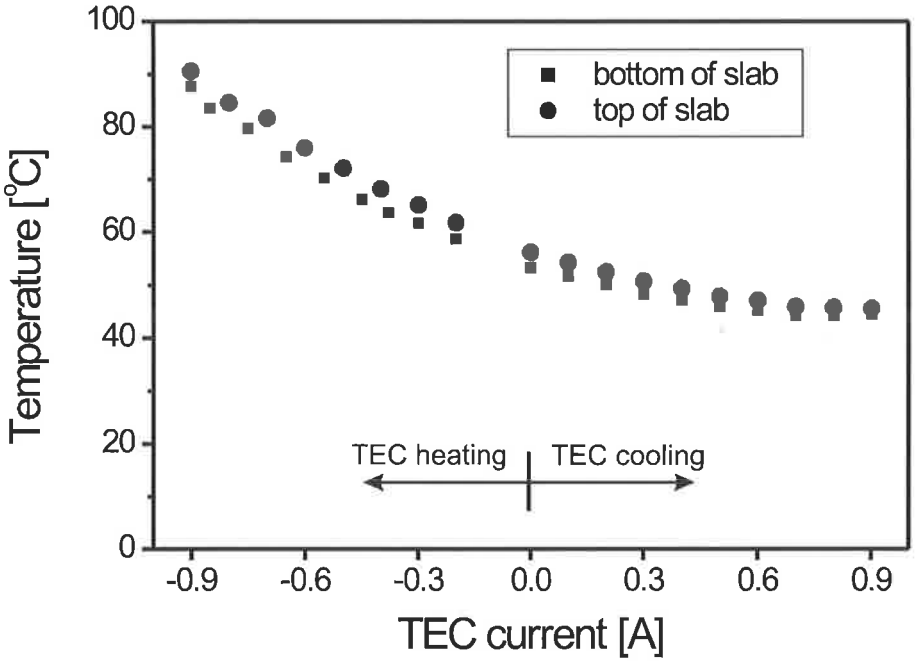

Figure 5.2: Temperature dependence of the bottom and top surfaces of the slab with TEC current.

5.3 Control of slab boundary temperatures using TEC's

The temperatures of the bottom and top surfaces of the slab as a function of TEC current were measured using thermistors mounted in copper heatsinks directly below and above the slab. The results are shown in Figure 5.2. The data points for the negative TEC currents in Figure 5.2 correspond to symmetric thermal lensing and were measured concurrently with the interferograms in Figure 5.4 (see later). As will be shown in section 5.4, this change in temperature of the bottom and top surfaces of 50°C between maximum TEC cooling and maximum heating allows a large range of thermal lens focal lengths to be attained.

5.4 Thermal lensing

Two different methods were used to measure the focal length of the thermal lens in the pumped Nd:YAG laser head. A probe-beam method was initially attempted before proceeding with an interferometric analysis using a Mach-Zehnder interferometer.

5.4.1 Probe beam method

A conceptually simple method of determining the focal length of the thermal lens is to measure the focussing of a collimated HeNe laser by the gain medium. This method was used by Murray[84] who measured the thermal lens in pulsed Nd:YLF and Nd:YAG rods. An image relay system was used to image the endface of the laser rod onto the principal plane of a lens of focal length, f_2. The longitudinal shift, Δz, of the subsequent waist from its initial position, z, can be related to the focal length of the thermal lens by[84]

$$f_{therm} = \frac{-z^2}{\Delta z} \tag{5.2}$$

provided that

$$\frac{\lambda f_2}{\pi \omega_2}\left(\frac{1}{1 - f_2/R_w}\right) \ll 1 \tag{5.3}$$

where ω_2 and R_w are the radius and wavefront curvature of the probe beam at lens f_2.

This method was attempted with the TIR zigzag slab laser head described in Chapter 4. It was expected that the dioptric power would depend linearly on the pump power, but this was not observed. Examination of the assumptions adopted when using this method revealed that Equation 5.2 becomes inaccurate for short thermal lens focal lengths. The method relies on a series expansion and truncating the series after the first two terms. Short thermal lens focal lengths require

more terms to be included to achieve sufficient accuracy. Hence, the equation and method outlined above is accurate for weak thermal lensing (long thermal lens focal lengths) only. This method was therefore abandoned and the interferometric method described below used.

5.4.2 Mach-Zehnder interferometer

Mach-Zehnder interferometers are dual arm instruments in which a single laser beam is divided at a beamsplitter, producing two beams that are recombined at a final (second) beamsplitter. Any phase change encountered by one beam and not the other will manifest itself as a distortion of the interference between the recombined beams.

In this work the interferometer was operated with one beam propagating through free space (the reference beam) and the other passing through the laser crystal. The layout of the Mach-Zehnder interferometer is shown in Figure 5.3. A π-polarized HeNe beam was shaped using cylindrical optics to fill the effective aperture of the Nd:YAG slab. The beam was split at the first beamsplitter wedge, one beam passed through air to the second beamsplitter wedge while the other beam passed through the max-R (at 1.064 μm) mirror, Nd:YAG slab, 75% reflectance output coupler (at 1.064 μm) mirror and 45 degree beamsteering mirror (at 1.064 μm), to the second beamsplitter. The interferometer arms were pathlength matched. The recombined beams propagated to the charge-coupled device (CCD) via a HeNe laser line filter and an imaging lens. The Brewster face of the slab closest to the CCD was imaged onto the CCD. Thus the phase change due to propagation through the pumped slab could be measured.

The resonator was lasing during the measurement since more of the energy in the upper state would otherwise be dissipated in the gain medium. This is due to an increased number of non-radiative transitions and changes in the absorbed spontaneous emission by the laser head. This produces increased heating of the slab, which changes the boundary conditions and may result in an extra 10 - 20 W (in this instance) of power being absorbed by the laser head compared with normal operation.

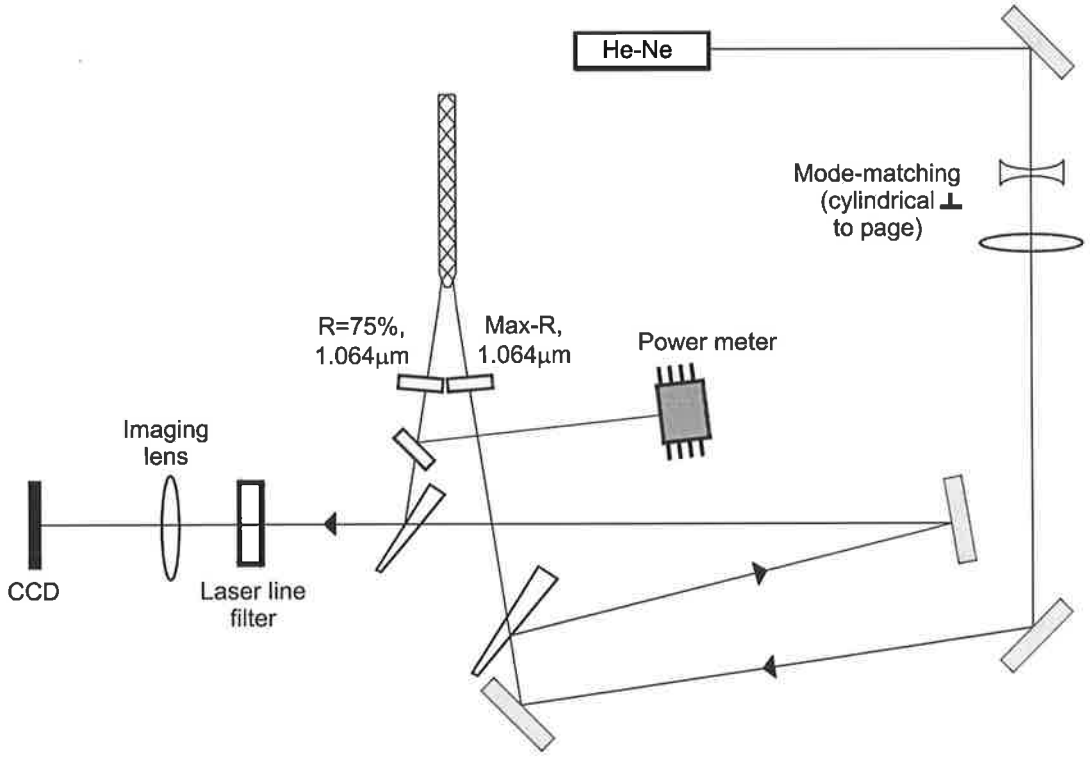

Figure 5.3: Mach-Zehnder interferometer configuration used to measure the thermal lens focal length.

In the absence of pumping, the interferometer produced a zero fringe over the entire slab aperture. Interferograms were recorded as the amount of heat deposited or removed by the TEC's at the bottom and top of the slab was varied (100 W pump power). The flow rate and temperature of the side-cooling water were constant. The measured interferograms are shown on the left-side of Figure 5.4(A)-(D).

Heat removal (A) (positive TEC current) increases the vertical thermal gradient and decreases the focal length of the vertical thermal lens, thus increasing the number of fringes between the centre of the slab and the bottom or top surface. Interferogram (B) shows the case of no active heat transfer by the TEC's (zero TEC current). The more interesting case from the viewpoint of the laser design is where the focal length of the thermal lens is increased (reduced dioptric power). This corresponds to negative TEC currents, which heats the bottom and top surfaces and thus reduces the vertical temperature gradient in the slab. Interferogram (C) shows a region of zero gradient above and below the central region of the slab. As the heating is increased the zero-gradient regions migrate towards the centre of the slab, as shown in (D). A further increase in heating would result in the formation of a negative lens in the central zone. These interferograms show that the vertical thermal lens in the region of the laser mode can be adjusted by controlling the heat transfer through the bottom and top surfaces of the slab.

While the interferograms in Figure 5.4(A)-(D), illustrate qualitatively the thermal performance of the laser head, quantitative analysis is difficult due to the limited number of fringes. To measure the thermal lens accurately, the wavefront in the reference arm was tilted in the vertical direction to increase the number of fringes.

A reference interferogram was recorded for the unpumped slab. The wavefront distortion due to pumping of the slab was determined by subtracting the fringe positions in the reference interferograms from those in the interferograms of the pumped slab. The resulting profiles are shown on the right-hand sides of Figure 5.4(A)-(D) and illustrate the migration of the region of zero gradient. Cooling of the bottom and top surfaces increases the optical-pathlength gradient (A). Heating of these surfaces can reverse the gradient and reduce the wavefront distortion in the pumped region of the slab to less than $\pm$ 0.1 of a wave (D).

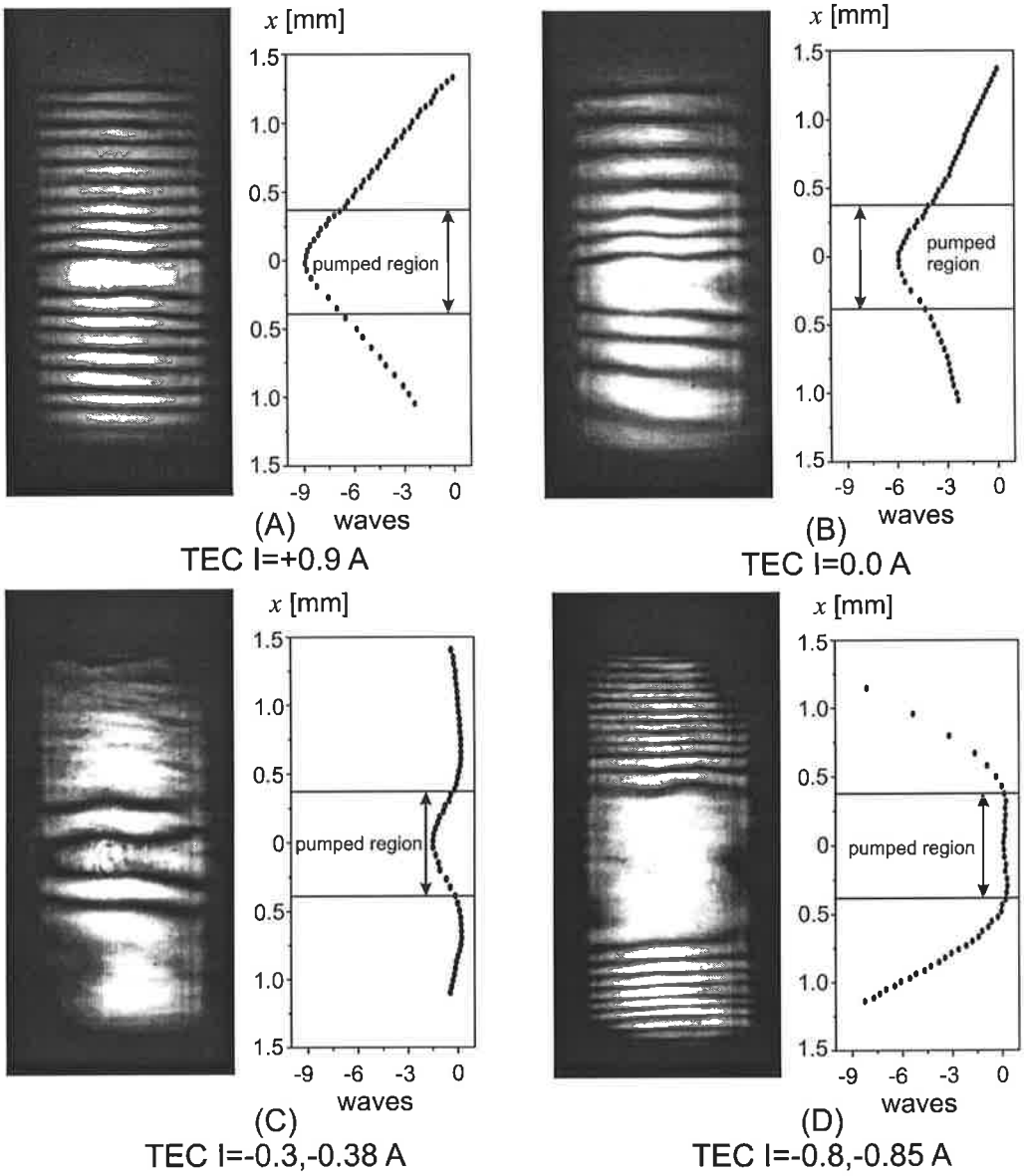

Figure 5.4: Mach-Zehnder interferograms of the Nd:YAG slab crystal for different bottom & top TEC currents. Negative (positive) TEC currents correspond to heating (cooling). The deviations from zero fringe are shown on the left-hand sides of (A)-(D). The data for the graphs on the right-hand sides of (A)-(D) was obtained by tilting the reference wavefront.

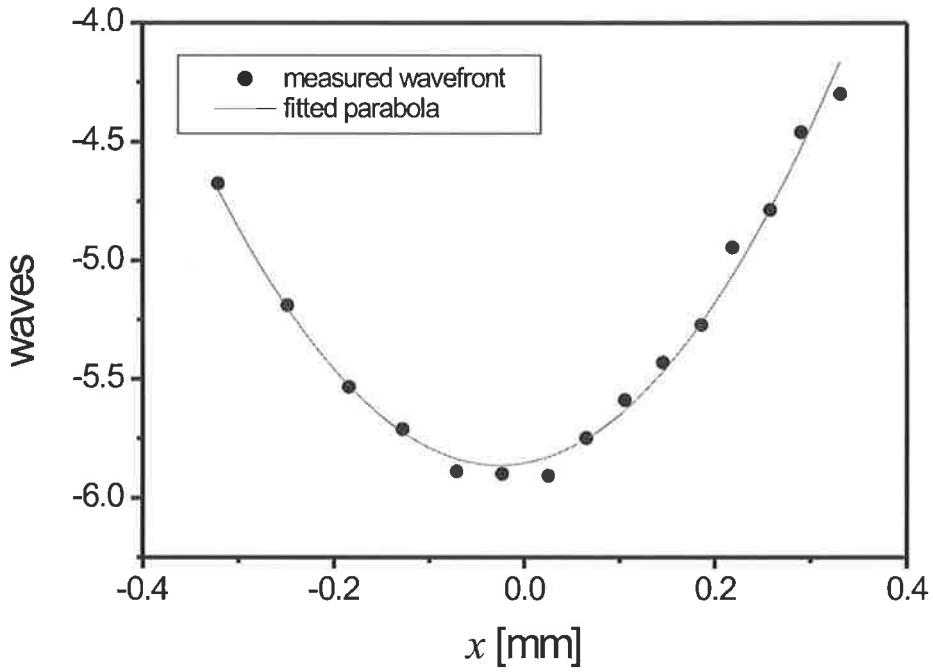

Figure 5.5: Parabolic fit of the data measured in the pumped region for a TEC current of 0 A (case B in Figure 5.4).

The focal length of the thermal lens in the pumped region of the slab can be estimated by fitting a parabolic curve to the data[85], giving cylindrical thermal lens focal lengths of 47 mm (A), 66 mm (B) and 450 mm (D). Figure 5.5 shows the measured data from the pumped region of Figure 5.4(B) and the parabolic fit.

The interferometer was then re-aligned to zero fringe in the vertical (x-) direction before introducing a tilt in the horizontal (y-) direction of the reference arm. The laser head was again operated at full pump power and the wavefront distortion in the horizontal direction was measured over the range of the bottom/top TEC currents. The wavefront distortion for three different TEC currents is shown in Figure 5.6. The wavefront distortion was less than $\pm$ 0.2 of a wave, and was unchanged by TEC operating conditions. Thus, the optical design of the resonator in the horizontal (y-) plane will be independent of the vertical (x-) plane. This de-coupling of thermal lensing is critical for a scalable design. The focal length of the horizontal thermal

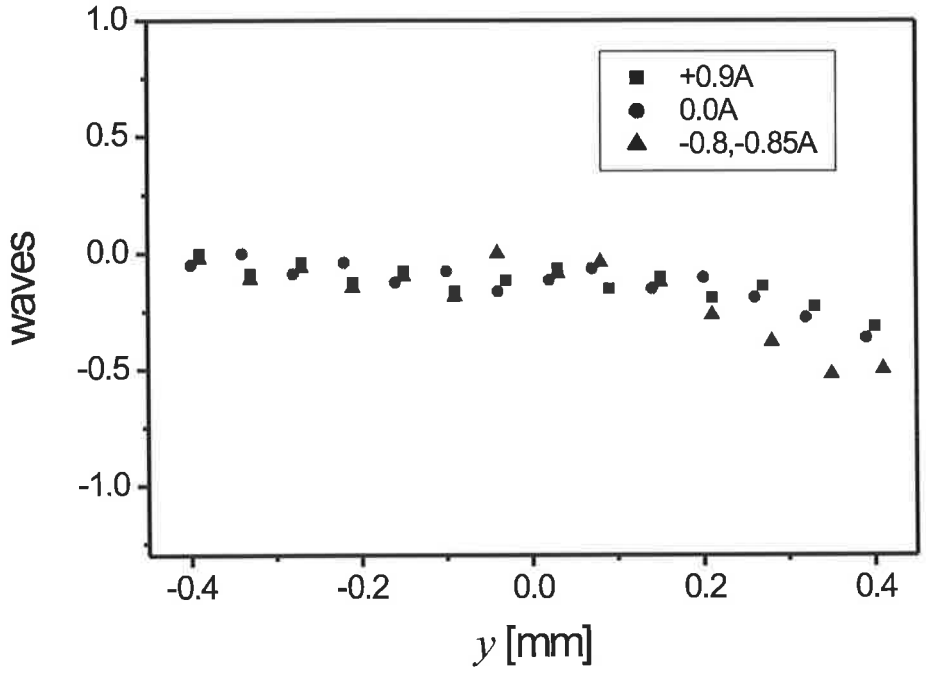

Figure 5.6: Wavefront distortion of a HeNe probe beam across the horizontal crystal aperture, while lasing, for different bottom/top TEC currents.

lens was in the regime of meter(s), the parabolic curvature of the tilted horizontal wavefront was too large to fit with an appropriate degree of certainty.

5.5 Optimum output coupling

Two flat mirrors were placed 2 cm from the end of the crystal, at normal incidence to the mode in a configuration similar to that shown in Figure 4.4. The measured multimode power for different output coupler reflectances is shown by Figure 5.7. The optimum reflectivity of the output coupler is between 70% and 80%. A maximum multimode power of 32 W from 100 W of pump power was achieved. This was measured with the bottom and top TEC's both operating at maximum cooling, thereby allowing many higher-order modes to oscillate and extract power from the gain medium. The multimode optical-to-optical efficiency was 32%.

Figure 5.8 shows the predicted output power for a standing-wave resonator as a function of output coupler reflectance, calculated using Equation E.4 (see App. E) and the parameters in Table 5.2. For a 3% loss factor, Figure 5.8 shows a predicted optimum reflectance between 70-80%, and a predicted output power of 32.1 W, in good agreement with experiments. An output coupler reflectance of 75% was used for the remaining measurements.

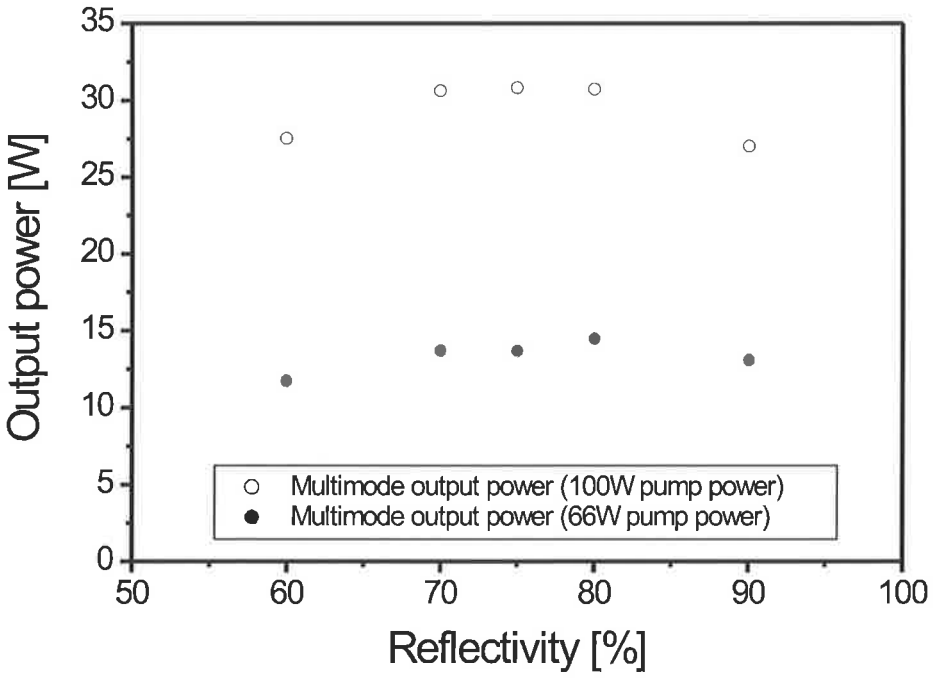

Figure 5.7: Measured output coupler reflectivity for the short multimode stable resonator with flat mirrors.

5.6 Multimode slope efficiency

To assess the efficiency of the laser head the multimode slope efficiency was measured. The output power (multimode) of the laser as a function of input pump power is shown in Figure 5.9. This was measured with the TEC's turned off. The fitted slope efficiency of the multimode laser was 37.2%.

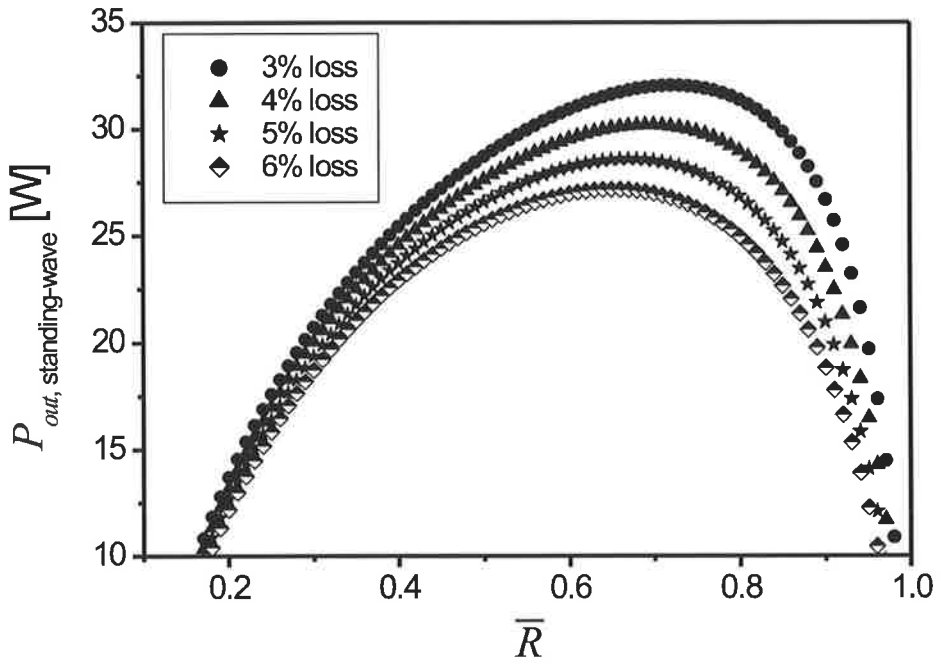

Figure 5.8: Calculated output power of the standing-wave resonator as a function of the output coupler reflectance, $\overline{R}$, for different single-pass loss factors, Y. Total pump power, 104.3 W.

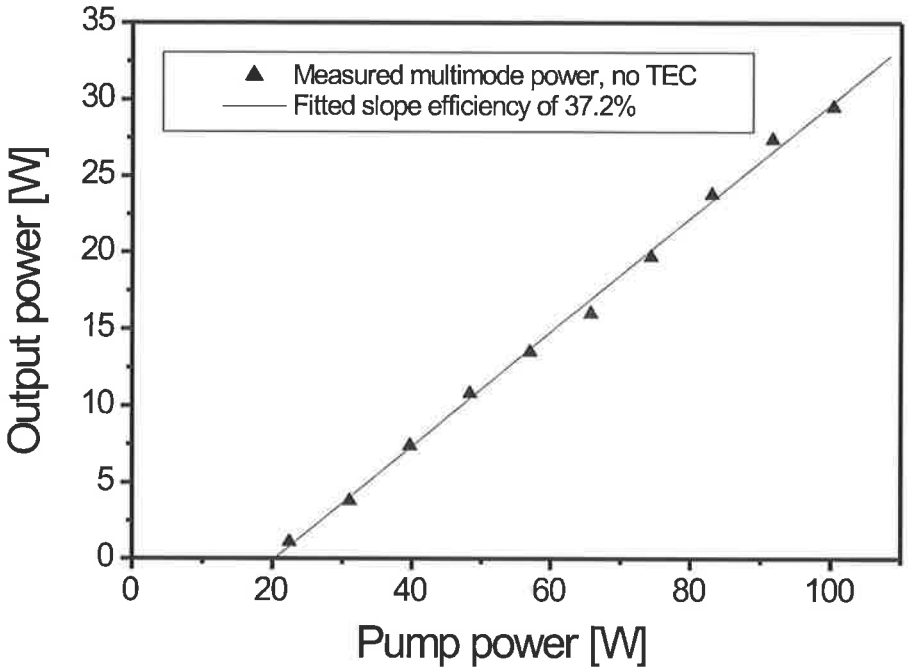

Figure 5.9: Multimode slope efficiency of the stable resonator, no TEC current. Fitted slope efficiency is 37.2%.

5.7 Single transverse fundamental mode performance

For single transverse fundamental mode operation, the mirrors were moved to between 10.5 cm - 10.8 cm from the crystal end. Increasing the cavity length increases the diameter of the horizontal transverse fundamental mode. When the diameter $(1/e^2)$ of the fundamental mode is approximately 60% of the aperture diameter, the fundamental mode will have good transmission while the higher-order modes will experience large losses[86]. This provides mode discrimination in the horizontal plane.

In the vertical direction mode discrimination was achieved with a combination of gain aperturing (only the central region of the crystal was pumped), increased armlength and vertical thermal lens control by using the TEC's to change the tem-

perature of the bottom and top of the slab.

This configuration produced a laser power of 20 W with $M_y^2 = 1.19$ and $M_x^2 = 1.38$ with no thermal lens compensation[1]. Heating the bottom and top of the crystal using the TEC's with a current of -0.16 A improved the beam quality to $M_y^2 = 1.16$ and $M_x^2 = 1.15$ and yielded 18.5 W of laser power. The pump power in both cases was 100 W.

The multimode efficiency of 32% and near TEM_{oo} efficiency of 18.5% to 20% compare favorably with the results of Richards and McInnes [23] who achieved efficiencies of 35% and 25% respectively, as discussed in Chapter 4.1. Some decrease in efficiency could be expected since laser crystal was approximately 30% longer, giving increased loss. Also, the pump power used in these experiments was more than five-fold larger, increasing the thermal loading, aberrations and distortions within the gain medium. Furthermore, the near TEM_{oo} efficiency demonstrated here is comparable to the transverse fundamental mode efficiency achieved by other author's using side-pumped, side-cooled zigzag slab lasers[16].

5.8 Summary

This Chapter demonstrates that the laser head design, based on a diode-laser side-pumped, side-cooled Nd:YAG zigzag slab is viable. Fibre-coupling of the diode-lasers facilitates pumping of only the central region of the crystal, allowing high gain densities and efficient energy extraction without the influence of apertures in the vertical direction. The thermal lens in the vertical plane, normal to the zigzag, can be adjusted without changing the lensing in the zigzag plane. Furthermore, the decoupling of the horizontal and vertical thermal lens allows scaling of the mode volume vertically. In principle the height of the vertical mode could be increased using additional layers of pump fibres, while maintaining the same inversion density, and the horizontal lens would not be expected to change. This is a design requirement for scalability.

The compact solid-state laser, efficiently produced a near diffraction limited

[1] M^2 measured using an M^2-101 Laser Beam Propagation Analyzer, and LBA-100A Laser Beam Analyzer from Spiricon, Inc., Logan, UT, U.S.A.

	Multimode	**TEM_{oo} - case 1**	**TEM_{oo} - case 2**
Maximum power	32 W	20 W	18.5 W
Optical Efficiency	32%	20%	18.5%
Beam quality, M_y^2	N/A	1.19	1.16
Beam quality, M_x^2	N/A	1.38	1.15

Table 5.3: Summary of multimode and transverse fundamental mode performance. Cases 1 and 2 were different operating conditions (case 1 was no TEC operation, and case 2 was with bottom/top TEC currents of -0.16 A).

TEM_{oo} output of 20 W, when pumped with 100 W. The laser output performance is summarized by Table 5.3. These results are comparable with the performance cited by Richards and McInnes. The results in this Chapter form the basis of a publication[2], a copy of which is included in Appendix G of this thesis.

Shortly after the work in this Chapter was completed the multimode laser power dropped approximately 30% at full pump power. A small fracture in the slab was subsequently observed. This fracture increased the intra-cavity loss, therefore decreasing the efficiency of the laser. Thus the experiments in Chapter 7 were not conducted using the full pump power of 100 W. Their purpose was to demonstrate operation of the stable-unstable resonator and not to assess the efficiency.

The next phase of this work involved investigating a stable-unstable resonator. Chapter 6 contains a model based investigation of a travelling-wave stable-unstable resonator. The optimum magnification of the unstable resonator and an estimation of the surface stress of the gain medium are considered. The mode properties of the unstable resonator are evaluated using a Fox-Li type analysis. To demonstrate the stable-unstable resonator concept is viable, proof-of-principle experiments in Chapter 7 show the operation of a standing-wave stable-unstable resonator.

Chapter 6

Travelling-Wave Stable-Unstable Resonator

The characterization experiments in Chapter 4 showed that the laser head design is viable. In this Chapter it will be shown that, in principle, such a laser head can be used to produce a travelling-wave stable-unstable resonator, suitable for injection locking.

The beginning of this Chapter describes the optimum magnification and stress calculations for the laser head assuming an increased pump power of 520 W and an increased mode volume, compared to the setup in Chapters 4 and 5. The remainder of the Chapter analyses the design of the travelling-wave stable-unstable resonator. As discussed in Chapter 3, the resonator design is to be stable in one plane and unstable in the orthogonal plane. This allows the horizontal and vertical modes to be treated separately. The unstable resonator incorporates a slab gain medium with a non-uniform gain distribution and mirrors with finite apertures and therefore requires analysis using a Fox-Li model. Section 6.2 gives a brief explanation of Fox-Li modelling, which is used in section 6.3 to analyze the travelling-wave strip unstable resonator. The parameter values used in the modelling in this Chapter are listed in Table 6.1.

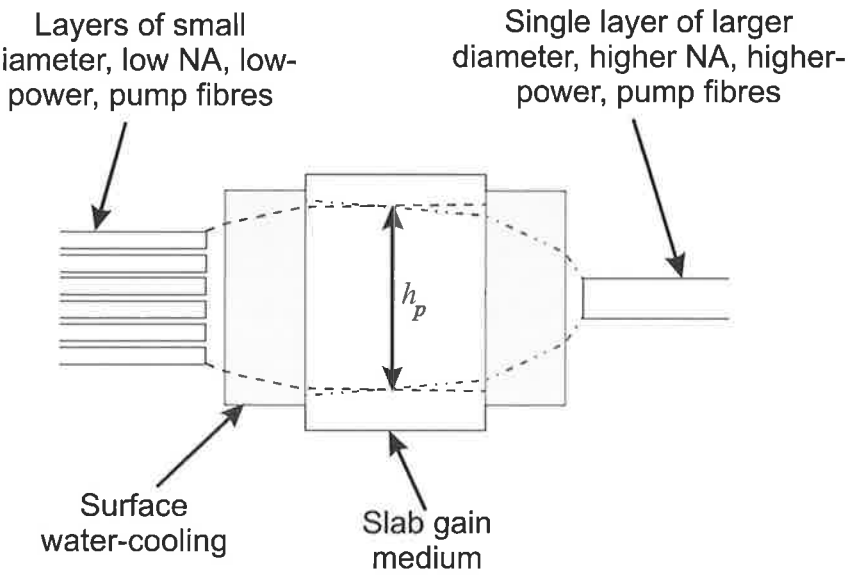

Figure 6.1: End view of the pumped slab, h_p is the height of the pumped region. Several layers of small diameter, low power, low NA pump fibres (left) or one layer of larger diameter, higher power, higher NA pump fibres - both solutions can be used to achieve a similar pump density, as indicated by the pump light envelopes.

6.1 Optimum magnification & stress calculation

The aim of this section is to demonstrate that the gain density and gain volume can be increased sufficiently to allow the use of a travelling-wave strip unstable resonator without fracturing the gain medium. Increasing the mode volume in the vertical direction can be achieved in practice by either stacking multiple layers of small diameter, low NA, low power pump fibres (see Figure 6.1 (left)) or by using a single layer of higher power, higher NA fibres (see Figure 6.1 (right)).

6.1.1 Optimum magnification

The output power for a travelling-wave resonator, $P_{out,\ \text{travelling-wave}}$ can be calculated as a function of the average reflectance of the output coupler, $\overline{R}$, for a given loss, Y, using Equation E.5. The results are plotted for a range of possible losses in Figure 6.2. From Figure 6.2, the optimum average reflectance of the output coupler, R_{opt}, which will achieve maximum energy extraction efficiency, is between 70% and

Parameter	Value
Pumped width, w_p	3.0 mm
Pumped height, h_p	2.2 mm
Pumped length, l_p	20.0 mm
Total pathlength in crystal	0.0905 m
Water channel width	1.5 mm
Pump fibre diameter	600 μm
Pump fibre N.A.	0.22
Pump power/fibre	20 W
Number of pump fibres	26
Total pump power	520 W
Absorption coefficient @808 nm†	4.1 cm^{-1}
Estimated total absorbed pump power, P_p	368 W
Absorption wavelength, λ_{abs}	0.808 μm
Emission wavelength, λ_e	1.064 μm
Total slab height	4.3 mm
Slab dimensions	see App. C
Stimulated emission cross-section, σ_{21} $(^4F_{3/2} \rightarrow {}^4I_{11/2})$	2.8 E-23 m^2
Spontaneous fluorescence lifetime, τ_f	230 μs
$h\nu_l$	1.8694 E-19 J
Quantum efficiency, η_q	0.95
Stokes factor, η_s	0.76
$\eta_{tot} = \eta_q \eta_s$	0.722
Multimode beam overlap efficiency, η_B $\diamond$	0.85 [83]
Small-signal gain, g_o	58.94 m^{-1}
Pathlength in gain region, l_g	0.05147 m
Gain-length product, $g_o l_g$	3.034
Slab pump volume, V	1.32E-7 m^3
Mode cross-sectional area, A_m	2.81E-6 m^2
Saturation intensity, I_s	2.903E+7 W/m^2

Table 6.1: Quantities used for travelling-wave stable-unstable resonator gain modelling († measured, $\diamond$ average of 0.8 - 0.9). Note the slab dimensions are the same as in Appendix C, but the crystal height is changed to 4.3 mm.

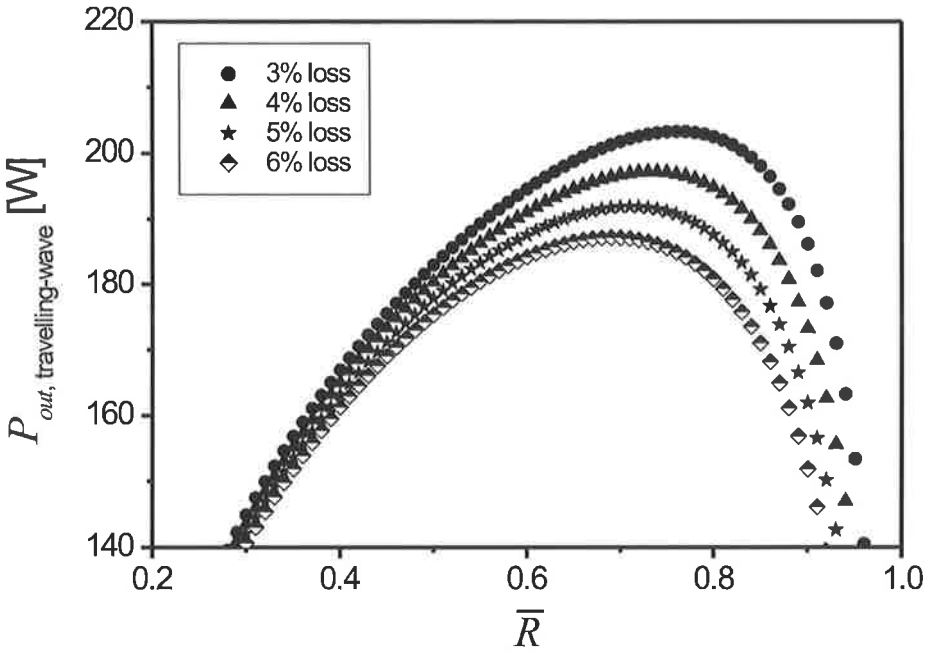

Figure 6.2: Calculated output power of the travelling-wave resonator as a function of output coupler reflectance, $\overline{R}$, for different single-pass loss factors, Y. Total pump power, 520 W.

80%, depending on the loss (Y). Note that a standing-wave unstable resonator with the parameters given in Table 6.1 yields a similar predicted output power for an $\overline{R}$ between 50% and 60%. The advantage of the travelling-wave resonator is the less complex injection locking.

The optimum average reflectance of the output coupler for the travelling-wave resonator restricts the allowed magnification, M, of the unstable resonator if the 'maximally flat' near-field profile is to be achieved. For example, if a $n = 2$ super-Gaussian profile is used then $\overline{R} = 1/|M|^2$ (see Eqn. 2.14). Hence, for a magnification of -1.3 (the minus sign indicates a negative-branch unstable resonator), $\overline{R} = 59\%$, which would reduce the output power by less than 5%. Thus, the chosen magnification is acceptable. From this discussion, it is evident that $|M|$ greater than 1.3 would significantly decrease the efficiency of the laser.

This result will be used later in this Chapter as the starting point for the Fox-Li

resonator design.

6.1.2 Thermally induced stress

To estimate the thermally induced stress, the thermal power deposited by quantum defect heating is assumed to be evenly distributed within the pumped volume of the slab, given by $w_p \times h_p \times l_p$. For $R_s = 1047$ W/m (see Table 3.1 in Chapter 3), and the dimensions of the pumped region given in Table 6.1, Equation 3.4 gives $(\sigma_s/\sigma_{\text{max.}})$ = 0.48. That is, the surface stress here is 48% of the stress fracture limit. This also indicates that an unstable resonator with $|M|$ greater than 1.3, which would require a greater pump density, is not feasible as the surface stress would approach the fracture stress of the slab.

However, several of the assumption involved with Equation 3.4 are not realized, the heat is not evenly distributed within the pumped volume of the slab, the slab is not infinitely high and the slab is not uniformly side-cooled. Heat generation within the crystal has a Gaussian distribution, and the heat removal is along a water channel height of 2.2 mm (compared to the slab height of 4.3 mm). Furthermore, the above prediction does not include the temperature dependence of the thermomechanical properties of the slab[87][88]. A co-worker, Dr. Martin Ostermeyer used a finite element analysis (FEA) model which includes non-uniform heat generation, non-uniform heat extraction and the temperature dependent properties of Nd:YAG to assess the result above, and found that the FEA model predicted $(\sigma_s/\sigma_{\text{max.}}) = 0.50$. This indicates that Equation 3.4 in this instance provides a good estimate of the surface stress of the slab. FEA analysis is an important for evaluating the effect of different pump geometries, due to the assumptions of Equation 3.4. Similar calculations for the laser head described in Chapters 4 and 5 showed that Equation 3.4 poorly estimated the surface stress, see the publication in App. G[2].

6.2 Fox-Li model

The Fox-Li technique involves propagating an initially random wave through an optical system that represents the resonator. The wave is continually propagated

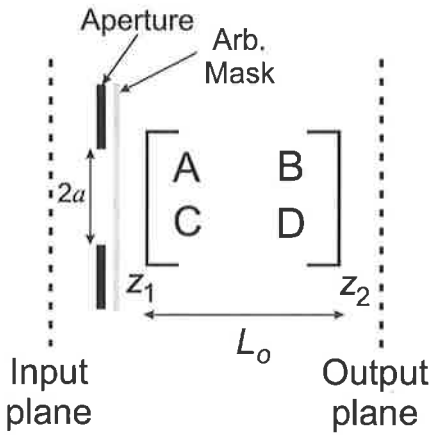

Figure 6.3: Physical setup used for wavefront propagation.

around the resonator until the amplitude at a specific location does not change appreciably after successive round-trips, thus yielding the amplitude distribution of the resonator eigenmode. Once convergence is obtained, an additional calculation can be used to determine the near-field amplitude distribution at the output plane. The output distribution can then be propagated to the far-field to investigate the beam quality.

The wave propagation within the resonator is modelled using commercially available computer software that applies Huygens' integral in the paraxial approximation[1]. The software propagates a wave through a system comprised of a hard-edged aperture, an arbitrary mask, and paraxial optical system described by an ABCD matrix, as shown in Figure 6.3.

The arbitrary mask allows specific reflectivity profiles, soft-edged apertures and gain apodization effects to be incorporated in the Fox-Li model. This is described further later in this section.

Propagation of a one-dimensional wave (amplitude) $\tilde{u}_1(x_1)$, truncated by a hard-edged aperture with full-width $2a$, from plane z_1 to z_2, is given by Huygens' integral through the general ABCD system[89][90][91]

[1]Fresnel, submodule of PARAXIA Resonator and Optics Programs version 2.02, distributed by SCIOPT Enterprises, San Jose, CA 95160, U.S.A.

$$\tilde{u}_2(x_2) = e^{-jkL_o}\sqrt{\frac{j}{\mathrm{B}\lambda_o}}\int_{-a}^{+a}\tilde{u}_1(x_1)\exp\left[-j\frac{\pi}{\mathrm{B}\lambda_o}\left(\mathrm{A}x_1^2 - 2x_1x_2 + \mathrm{D}x_2^2\right)\right]dx_1 \tag{6.1}$$

where k is the wavenumber, λ_o is the optical wavelength in free space, L_o is the on-axis optical path length, A, B and D are the ABCD matrix elements. x_1 and x_2 represent the transverse positions at the input (z_1) and output (z_2) planes respectively. If there is more than one aperture within the resonator then Huygens' integral cannot be applied for the full resonator in one evaluation. Instead, at each aperture it is necessary to evaluate Huygens' integral from that aperture to the next aperture, and so on.

Fast Fourier Transform (FFT) techniques are used to evaluate the Huygens' integral and thus care needs to be taken with choosing the appropriate FFT sampling rates. The Fresnel Number ($\mathrm{N}_f = a^2/\lambda_o\mathrm{B}$) of the optical system between planes z_1 and z_2 determines the number of points used to describe the transverse dimension of the wave. The criterion used to avoid aliasing and ensure accurate evaluation of Huygens' integral was the number of points for the FFT should be greater than $8\mathrm{N}_f M$[92].

The remainder of this section discusses mathematical descriptions of optical elements that are included in the Fox-Li resonator model.

6.2.1 Gainmask

Only the central region of the crystal (in the vertical direction) is pumped by the optical fibres, as shown in Figure 6.1. This pump geometry is considerably different from uniform side-pumping. Consequently the Fox-Li model should include this gain inhomogeneity. In this work the gain inhomogeneity is included as a gainmask, which allows the effects of gain apodization to be approximated. It does not allow for the effects of the gain saturation and spatial hole burning produced by the zigzag path to be included.

The single-pass small-signal gain factor is given by

$$\mathrm{G} = \exp\left[g_o l_g\right] = \exp[\sigma n_p l_g] \tag{6.2}$$

where l_g is the pathlength in the gain region. The small-signal gain coefficient, g_o, is given by the product of the stimulated emission cross-section (σ) and the inversion density between the upper and lower laser level (n_p)[83].

The pump field from the single layer of large diameter, high power pump fibres was investigated by measuring the pump intensity profile. After a propagation distance of 1 mm it can be well approximated by a Gaussian profile. That is, $n_p(x)$ is given by

$$A\exp\left[-2\left(\frac{x}{w_{pp}}\right)^2\right] \tag{6.3}$$

where w_{pp} is the radius of the pump intensity profile within the slab. Note that h_p in Table 6.1 is equal to $2w_{pp}$.

The gain factor can be written using Equation 6.2 as

$$\mathrm{G}(x) = \exp\left[\sigma l_g A\exp\left\{-2\left(\frac{x}{w_{pp}}\right)^2\right\}\right] \tag{6.4}$$

This distribution is used as the gainmask in the Fox-Li model. The magnitude of the coefficient $\sigma l_g A$ is not important for this analysis since gain saturation is not included in the model and the waves are normalized at each aperture in the system.

The minimum Gaussian pump profile radius assumed in this analysis is 1.0 mm (see Table 6.1). The pump profile radius could be increased by moving the pump fibres away from the slab side faces (y-direction). Hence the gainmask models were chosen to have radii, w_{pp}, of 1.0, 1.1, 1.21, 1.44 and 1.66 mm. The calculations using gainmasks will be compared to a calculation with no gainmask to asses the influence of the gainmask on the unstable resonator mode.

6.2.2 Thermal lensing of gain medium

In Chapter 4, the pumped Nd:YAG slab was shown to have a near parabolic refractive index profile in the vertical direction. Thus, the gain medium can be modelled as a lens duct, in which the index of refraction is given by [93]

$$n_c(x) = n_o\left(1 - \frac{1}{2}\widetilde{\gamma}^2 x^2\right) \tag{6.5}$$

where n_o is the index of refraction of the duct at the optical axis and $\widetilde{\gamma}$ is a duct parameter which is related to the rate of transverse variation in index of refraction.

The general form of an ABCD matrix that describes a duct with geometric length, L, is[93]

$$\begin{bmatrix} \cos\widetilde{\gamma}L & (n_o\widetilde{\gamma})^{-1}\sin\widetilde{\gamma}L \\ -n_o\widetilde{\gamma}\sin\widetilde{\gamma}L & \cos\widetilde{\gamma}L \end{bmatrix} \tag{6.6}$$

The effective focal length of the lens duct can be found by comparing the matrix above and the ABCD matrix of a thick lens. Thus the 'C' element of the matrix above is equated to $-1/f_{therm}$, which gives

$$f_{therm} = \frac{1}{n_o\widetilde{\gamma}\sin(\widetilde{\gamma}L)} \tag{6.7}$$

For the Fox-Li modelling in Section 6.3, $\widetilde{\gamma}$ is calculated for each value of the chosen focal length of the thermal lens, f_{therm}. This gives the ABCD matrix elements for the lens duct.

6.2.3 Output coupler model

The GRM output coupler can be modelled using several methods. A GRM with a Gaussian profile can be described using the ABCD formalism[39]

$$\begin{bmatrix} 1 & 0 \\ -j\epsilon & 1 \end{bmatrix} \tag{6.8}$$

where $\epsilon = \lambda/\pi w_{ga}^2$ and w_{ga} is defined by the amplitude reflectivity $r(x) = \exp[\frac{-x^2}{w_{ga}^2}]$. This matrix formalism is directly applicable to the Huygens' integral described earlier, where the ABCD matrix of the GRM is multiplied with the ABCD matrix of the remaining system.

A more flexible approach, however, is to use a mask multiplication operation, which allows arbitrary mask functions to be used (e.g.: parabolic, order n super-Gaussian, etc.) rather than only the Gaussian profile above. In this approach the incident wave is multiplied by a mask function, changing the amplitude profile, before applying Huygens' integral to calculate the resultant wave amplitude at z_2. Both approaches give the same result.

6.3 Travelling-wave stable-unstable resonator

The travelling-wave resonator analyzed in this section was discussed briefly in Chapter 4, and is shown by Figure 6.4. The apex angle (closest to the slab end) of the reflecting prism is 80° and a max-R coating at 57° angle of incidence (π-pol.) has been applied to the adjacent surfaces, as indicated by the shaded lines in Figure 6.4. Using the prism to separate the beams produces small angles of incidence at the GRM and the max-R mirror. This will allow the injected beam from the master laser and the output beam to pass through the centre of the piezo-electric transducer (PZT) tube on which the GRM will be mounted for active stabilization of the injection lock. Furthermore, small angles of incidence simplifies coating of the GRM, and the resonator armlengths can be increased simply by moving both mirrors away from the prism.

The travelling-wave mode of interest here travels clockwise around the ring; it reflects from the GRM to the max-R mirror via lens f_2, then from one side of the coated prism, through the TIR slab, to the other coated surface of the prism and

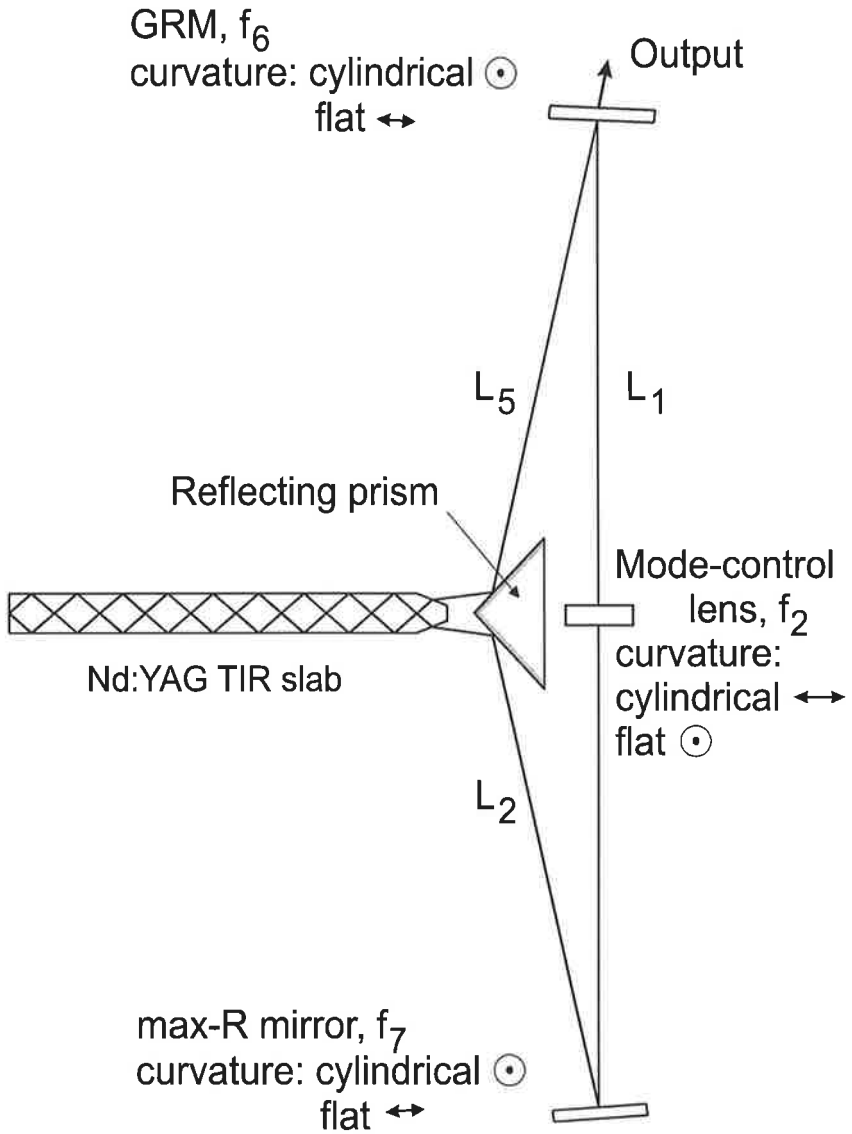

Figure 6.4: Travelling-wave stable-unstable resonator configuration. The GRM and max-R mirrors are cylindrical perpendicular to the page, as indicated by "⊙", and flat in the plane of the page. The mode-control lens is cylindrical also but orthogonal to the GRM and max-R mirrors. The reflecting surfaces of the prism are indicated by the shaded line.

on to the GRM, thus closing the ring. The vertical magnification of the mode is determined by the strength of the thermal lens, and the curvatures of the cylindrical GRM and max-R mirrors. Horizontal mode control is provided by the residual thermal lens and the mode-control lens, f_2.

This section describes the resonator design in both the horizontal (stable) and vertical (unstable) planes. The choice of mirror curvatures and GRM properties, such as the reflectivity profile, radius and peak reflectance are discussed.

6.3.1 Horizontal plane - stable

As discussed in Section 5.7, if the mode in the horizontal plane adequately fills the entrance and exit apertures of the Nd:YAG slab then the mode will couple efficiently to the gain. Furthermore, if the lowest-order mode diameter is approximately 60% of the diameter of one of these apertures then there will be sufficient discrimination against higher-order modes while not limiting the power in the lowest-order mode[86]. Thus, a horizontal mode radius of 0.38 mm is required at the slab apertures.

An ABCD model of the resonator in the horizontal plane was used to design the stable resonator. The combination of a weak residual horizontal thermal lens and f_2 produce a stable horizontal mode. Figure 6.5 shows the calculated dependence of the horizontal mode radius at the slab aperture on the focal length of the horizontal thermal lens, for given mode-control lens focal lengths, f_2. Choosing the appropriate focal length of f_2 allows the mode radius at the crystal aperture to be adjusted for optimum operation. The appropriate Gaussian mode radius (indicated by the dash-dot line in Figure 6.5) can be achieved for horizontal thermal lens focal lengths in the regime of meter's, which coincides with the value estimated in Chapter 5.4.2.

6.3.2 Vertical plane - unstable

As discussed above, a Fox-Li model is used to predict the vertical mode profile and determine the most appropriate GRM reflectivity. The flow chart in Figure 6.6 shows how the resonator design was determined. Initially:

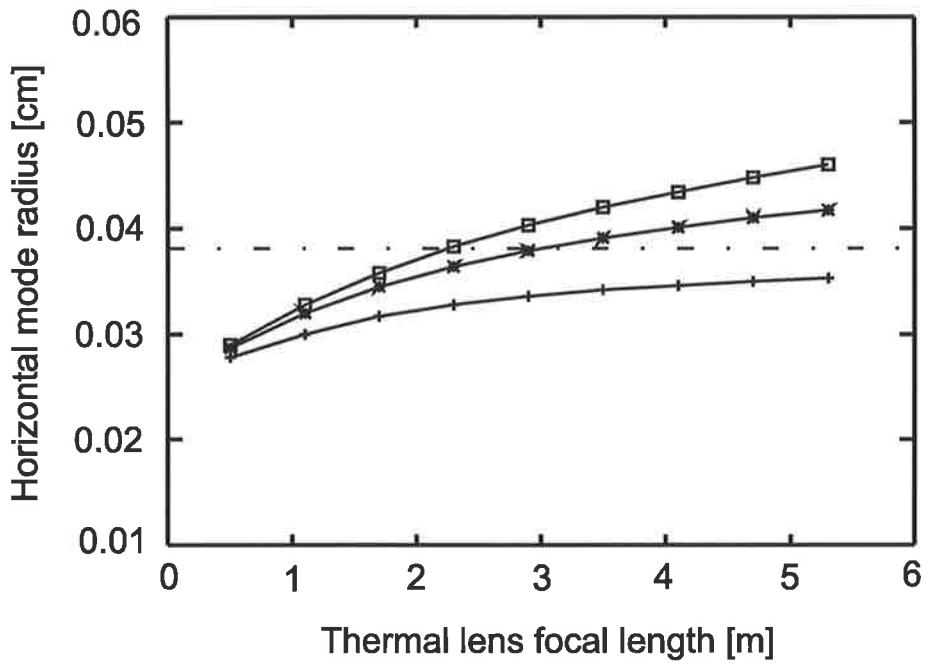

Figure 6.5: Plot of dependence of the stable mode radius at the entrance and exit faces of the slab as a function of the focal length of the horizontal thermal lens for various mode-control lens focal lengths, f_2 (mode control lens focal lengths of 0.8 m (+), 2.6 m (*) and 15 m (□)). The horizontal dash-dot line represents the optimum mode radius of 0.38 mm.

1) Determine the unstable resonator magnification based on the expected optimum average reflectance, using Equation 2.14 - see section 6.1.1.

2) Determine the functional form of the pump profile and the radius of the pump profile, w_{pp}, for the gainmask - see section 6.2.1.

3) Choose the height of the gain medium - see Table 6.1.

4) Select the resonator configuration including the mirror curvatures, separations, and the focal length of the thermal lens.

5) Estimate the GRM properties such as the reflectivity profile, profile radius (Eqn. 6.10) and peak reflectivity (Eqn. 2.13).

The Fox-Li model is then evaluated in the absence of a gainmask, to confirm the geometric magnification of the resonator. After this the gainmask is included in the model. The resonator parameters are then modified to adjust the magnification, spatial overlap of gain and mode regions, and the average reflectance of the GRM. Finally, the beam quality and mode discrimination are assessed by considering the near- and far-field profiles.

Resonator configuration: negative-branch confocal

A negative-branch unstable resonator was chosen for this application due to the greater perturbation and alignment stability compared to the positive-branch resonator, see Chapter 2.1. Negative-branch unstable resonators are known to be sensitive to changes in resonator length, but, in this application the length of the resonator will be actively controlled to stabilize the injection lock[46]. A disadvantage of negative-branch unstable resonators in some instances is they have an intra-cavity focus[46]. However, the travelling-wave resonator length modelled here is quite long (approx. 35 cm), and therefore the focal spot can be located outside the gain medium and between the mirrors so as to avoid damage of the optical components. Furthermore, since this laser is CW, the power density at the focal spot is much less than that required to cause breakdown of the air at the focal spot, which is the major issue in pulsed lasers.

A confocal unstable resonator is considered here. These resonators are preferred for many applications as they produce a collimated mode within the gain region,

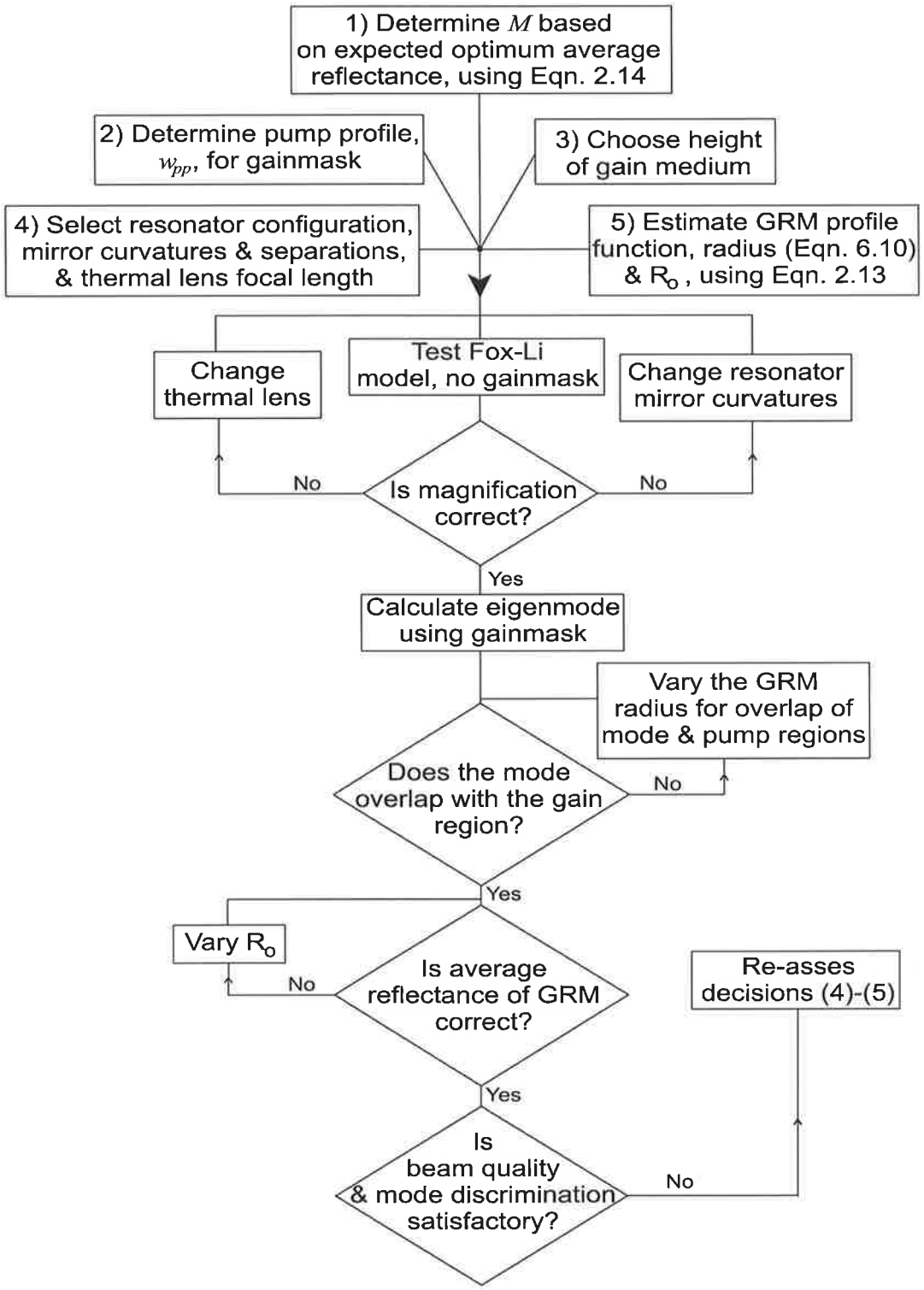

Figure 6.6: Design flow chart used to choose appropriate strip GRM unstable resonator parameters.

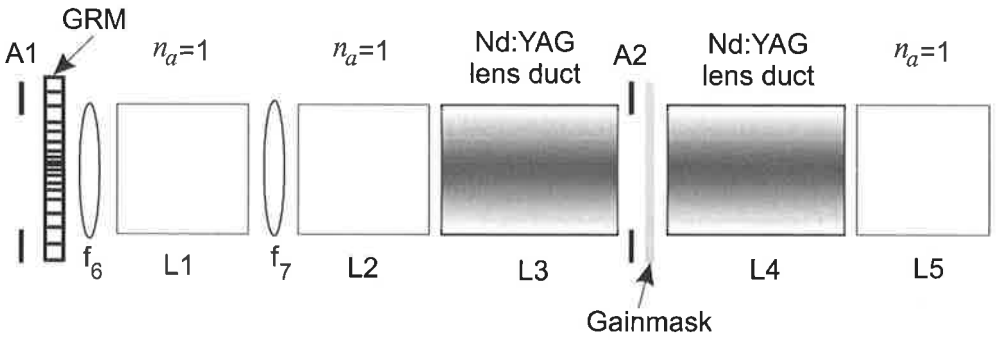

Figure 6.7: The basic model used for travelling-wave unstable resonator calculations (vertical plane).

and typically produce a collimated output beam. Thus a negative-branch confocal travelling-wave unstable resonator is considered in the remainder of this Chapter.

The equivalent lens-guide model of the unstable resonator is shown in Figure 6.7. Table 6.2 gives the parameters assumed for the model in Figure 6.7. The model was evaluated in two sections, from A1 to A2 and then from A2 to the GRM. A1 represents the GRM substrate aperture. A2 represents the height of the slab. f_6 and f_7 are the focal lengths of the GRM and max-R mirror respectively. The incident field passes through aperture A1, reflects from the GRM, is focussed by lens f_6, propagates through free space (L1), is focussed by f_7, before propagating through free space (L2) to the Nd:YAG slab. The Nd:YAG slab is treated as two successive sections of lens duct, with an aperture (A2) in between. L3 + L4 is the total length of the zigzag path within the slab. After the slab, the field propagates through free space (L5) before re-entering aperture A1.

In principle, the entire gain medium should be dissected into infinitely short lengths and Huygens' integral should be applied repeatedly, so as to thoroughly allow for the possible aperturing caused by the finite crystal height. However, the Fresnel number would be too large for each of these propagation segments and require more wavefront sampling points than could be achieved due to memory limitations of the computer used for this analysis. Furthermore, as described in the previous section, the confocal design of the resonator typically produces a mode that is collimated within the gain medium. Since the pumped region is smaller than the crystal aperture (see Table 6.1) and overlap of the mode and gain is desired, multiple

Parameter	Value
GRM aperture radius, A1	0.5 cm
Slab aperture radius, A2	0.215 cm
L1	11.54 cm
L2, L5	6.3705 cm
L3, L4	4.5229 cm
Nd:YAG refractive index	1.8197
GRM reflectivity profile function	$n = 2$ super-Gaussian
f_6	GRM, cylindrical curvature
f_7	max-R, cylindrical curvature
$\widetilde{\gamma}$	Lens duct parameter$^{\Sigma}$

Table 6.2: Quantities used for travelling-wave unstable resonator Fox-Li calculations ($^{\Sigma}$ The lens duct parameter, $\widetilde{\gamma}$, is related to the thermal lens focal length by Equation 6.7).

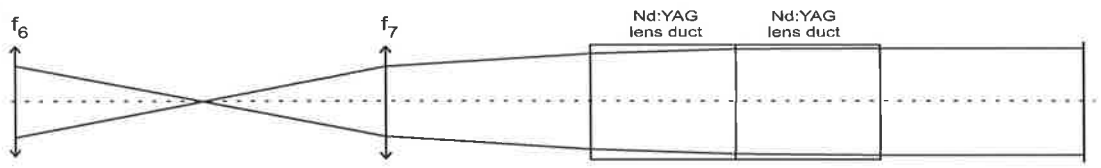

Figure 6.8: Gaussian beam propagation through the negative-branch travelling-wave unstable resonator model. The gain medium is treated as two successive sections of Nd:YAG lens duct. Note that the boxes labelled 'Nd:YAG lens duct' indicate schematically the location of the duct within the lensguide model and do not have a meaningful vertical scale.

apertures are probably not necessary. It was also assumed that the wavefront can be multiplied by the gainmask at aperture A2, the centre of the slab, on each round-trip.

Figure 6.8 shows the predicted transverse dimensions of typical mode propagating through the unstable resonator. The beam-path was predicted by propagating a Gaussian beam that had a profile radius of 0.722 mm and a wavefront radius of curvature of 54.5 m (the reason for this choice will become obvious later) through the resonator described later in this section, using the commercial software code ABCD[2]. The almost collimated mode within the lens duct justifies the assumptions above.

In general, a mode in a confocal unstable resonator can be considered as the

[2]PARAXIA-Plus, Resonator and Optics Program, release 0.95, distributed by SCIOPT Enterprises, P.O. Box 20637, San Jose, CA 95160, U.S.A.

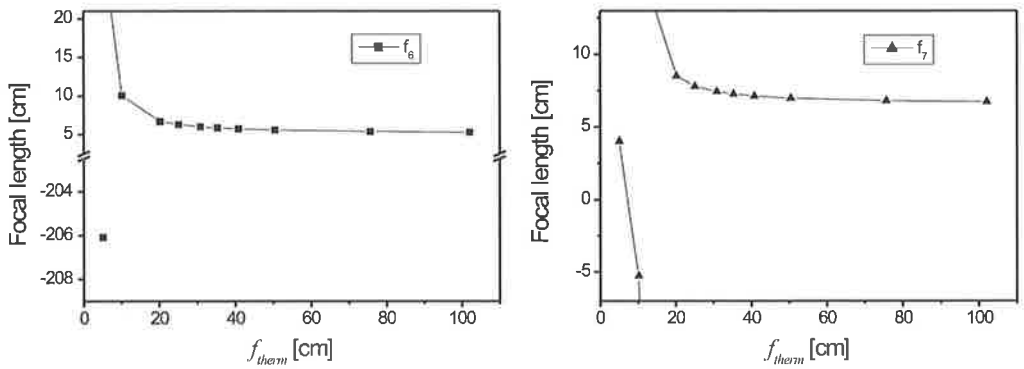

Figure 6.9: Focal length of the GRM substrate, f_6, and the max-R mirror, f_7, for the travelling-wave unstable resonator model as a function of the focal length of the thermal lens. Note the broken axis is used on the left graph due to the large deviation of the first point from the other values.

combination of a zero length telescope with magnification $|M|$, followed by free space propagation of equivalent length $-M$B[94]. It can be described by the following ABCD matrix:

$$\begin{bmatrix} A & B \\ C & D \end{bmatrix}_{\substack{Unstable \\ Resonator}} = \begin{bmatrix} 1 & -M\mathrm{B} \\ 0 & 1 \end{bmatrix} \begin{bmatrix} -M & 0 \\ 0 & \frac{1}{-M} \end{bmatrix} = \begin{bmatrix} -M & \mathrm{B} \\ 0 & \frac{1}{-M} \end{bmatrix} \tag{6.9}$$

To determine the focal lengths of the GRM and max-R mirrors, f_6 and f_7, the ABCD matrix in Equation 6.9 was equated to the ABCD matrix calculated for the travelling-wave resonator shown in Figure 6.4. The magnification was set to -1.3. This gives two equations with f_6 and f_7 unknown, for a given lens duct parameter, $\widetilde{\gamma}$, which allows f_6 and f_7 to be evaluated for a given thermal lens focal length.

The focal lengths of the resonator mirrors, f_6 and f_7, required to produce a magnification of -1.3 is shown in Figure 6.9. For thermal lens focal lengths shorter than 20 cm, f_6 and f_7 change significantly for small changes in the focal length of the thermal lens. Thus, a resonator design that uses thermal lens focal lengths greater than 20 cm would give the most reliable operation.

GRM profile

The output coupler chosen for the initial analysis was a $n = 2$ super-Gaussian profile since the pump profile also has a Gaussian form. The peak reflectance was chosen to satisfy the maximally flat condition for an $|M| = 1.3$ unstable resonator, that is $R_o = 76.9\%$ from Equation 2.13. The GRM profile radius can be estimated using Equation 6.10, which relates the $n = 2$ super-Gaussian GRM radius, w_{GRM}, and the radius of the mode incident on the GRM, w_{im}[95].

$$w_{GRM} = \frac{w_{im}}{\sqrt{M^2 - 1}} \tag{6.10}$$

Since w_{im} is unknown, it was initially assumed to be similar to the smallest radius of the pump profile in the crystal. The smallest w_{pp} value considered is 1.0 mm, thus $w_{im} = 1.0$ mm and $w_{GRM} = 1.20$ mm.

Fox-Li analysis

The lowest-loss mode of the negative-branch confocal travelling-wave unstable resonator was calculated for several thermal lens focal lengths between 20 cm and ∞. Figure 6.10 shows the magnification (a), average reflectance (b), mode radius at the crystal centre (c) and near-field radius after transmission through the GRM (d) for several thermal lens focal lengths and a variety of gainmasks. The magnification was calculated by comparing the radii of the intracavity modes just before and just after reflection from the GRM. The average reflectance was calculated by comparing the integral of the intensity distribution just after reflection from the GRM to that just before the GRM. The mode radius at the crystal centre refers to the mode radius at aperture A2.

The solutions were calculated for gainmask models based on the Gaussian intensity pump profile radii, w_{pp}, of 1.0, 1.1, 1.21, 1.44 and 1.66 mm. A solution with no gainmask was also calculated to show the influence of the gainmasks. The horizontal lines on the graphs in Figure 6.10 indicate the result assuming an infinite thermal lens focal length, for each gainmask.

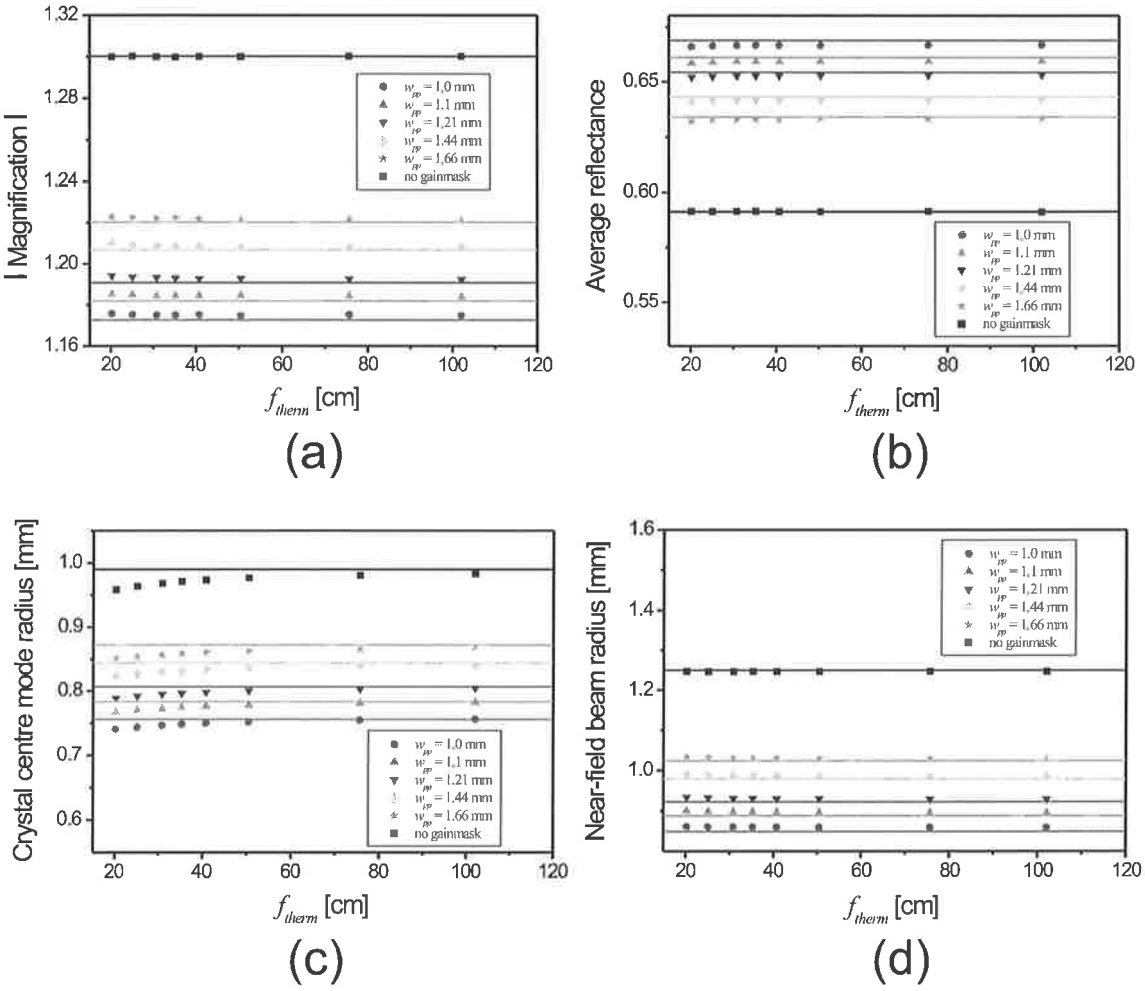

Figure 6.10: Magnification (a), average reflectance (b), mode radius at the crystal centre (c) and near-field radius after transmission through the GRM (d) for the travelling-wave stable-unstable resonator calculated for thermal lens focal lengths from 20 cm to 100 cm. The solid lines assume infinite thermal lens focal length in each case. Each curve assumes a different $n = 2$ super-Gaussian pump profile radius, as indicated. $R_o = 76.9\%$ and $w_{GRM} = 1.20$ mm for all points.

Figure 6.10(a) shows that the resonator operates as expected and discussed above when there is no gainmask. When the gainmask is included in the model, however, the gain guiding significantly reduces the magnification and mode size. Since the mode size is much smaller than the size of the pumped region, the laser will be inefficient and there will be unsaturated gain potentially available to higher-order modes.

The size of the mode can be changed by varying the GRM radius, w_{GRM}. Figure 6.11 shows the change in magnification (a), average reflectance (b) and the mode radius at the crystal centre (c) as w_{GRM} is varied. Note that these results, and all further predictions, assume $f_{therm} = 25$ cm and $w_{pp} = 1.1$ mm. As w_{GRM} is reduced, the effect of the gainmask on the formation of the unstable mode is reduced, hence $|M|$ approaches 1.3. Unfortunately, the mode radius at the crystal centre is also reduced (see Figure 6.11(c)) so this solution is not practical. Increasing w_{GRM} increases the mode radius at the crystal centre but further decreases $|M|$, which will probably degrade the mode discrimination of the unstable resonator.

However, the mode discrimination of the resonator will not be degraded as quickly as the decrease in $|M|$ suggests. Figure 6.12 shows that the average reflectivity, $\overline{R}$ does not increase as quickly as would be predicted by $1/M^2$. That is, while the mode discrimination in a standard unstable resonator is usually discussed in terms of $|M|$ because the output coupling losses are related to $|M|$, this is not the case for the resonator considered here, and therefore $|M|$ is not a good indicator of mode discrimination. Furthermore, mode discrimination in the design presented here is enhanced by ensuring that the lowest-order mode and pumped region overlap.

Increasing w_{GRM} beyond 2.15 mm would push the lowest-order mode outside the pumped region where the index of refraction profile changes from quadratic to linear. The lens duct model of the gain medium would then cease to be valid, and the wavefront would become abberated.

In Figure 6.11(c), the data point that has a crystal centre mode radius of 1.1 mm has a corresponding GRM average reflectance of 70%, according to Figure 6.11(b). From the gain calculation in section 6.1.1, the average reflectance of the GRM can be decreased by a further 10% with little change in output power. One approach to

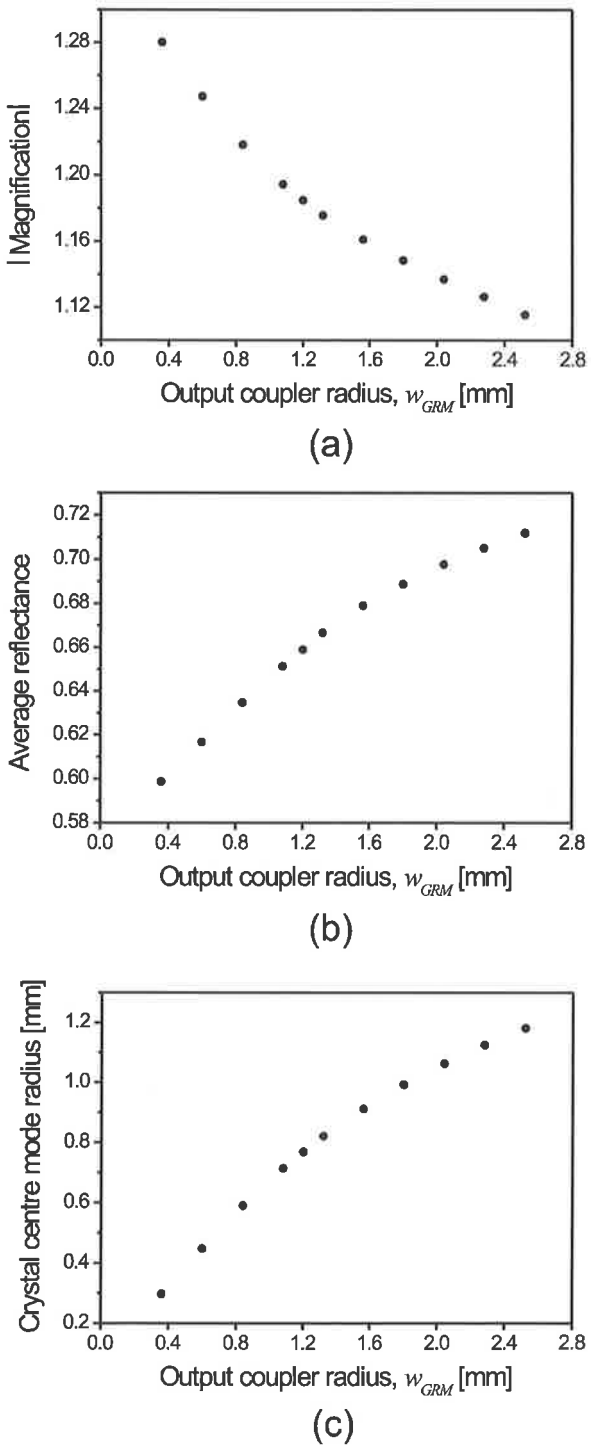

Figure 6.11: Magnification (a), average reflectance (b), and mode radius at the cystal centre (c) as a function of the GRM ($n = 2$, super-Gaussian) reflectance profile radius, w_{GRM}. A thermal lens focal length of 25 cm is assumed, $R_o = 76.9\%$, $w_{pp} = 1.1$ mm and the geometric magnification $= -1.3$.

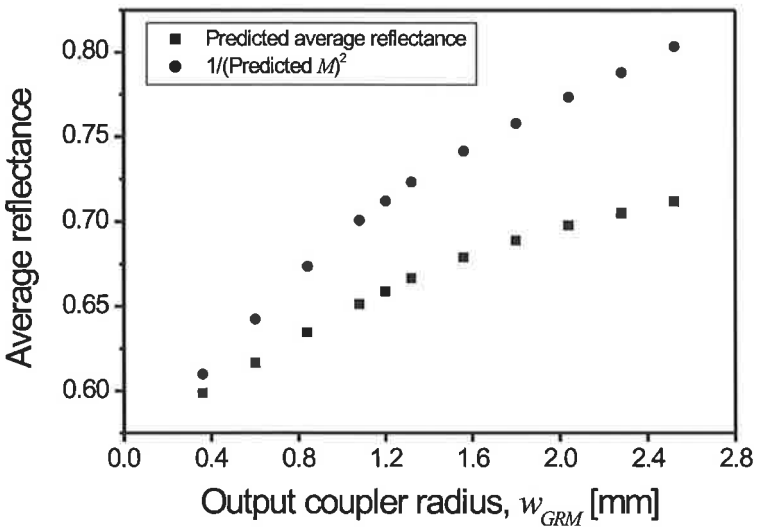

Figure 6.12: Average reflectance as a function of the GRM profile radius, w_{GRM}. Both the average reflectance of the GRM predicted by Fox-Li analysis, and the inverse of the Fox-Li predicted magnification squared are included on the graph. The focal length of the thermal lens was 25 cm, $w_{pp} = 1.1$ mm, $R_o = 76.9\%$ and the geometric magnification $= -1.3$.

decrease the average reflectance of the GRM is to decrease the peak reflectance of the GRM profile. However M is only -1.12 (see Figure 6.11), which requires R_o to be increased to 89% (using Eqn. 2.13), to achieve a maximally flat near-field. Thus, decreasing R_o is a move in the wrong direction.

Another approach which recovers the mode discrimination properties and probably enhances the alignment stability, is to increase the magnification of the unstable resonator. As discussed in Chapter 2.1, the advantage of increasing M is that it decreases the sensitivity due to perturbations and misalignments of the resonator.

The curvatures of the GRM and max-R mirrors in the Fox-Li model were therefore changed to give a geometric magnification of -1.5. Figure 6.13 shows the magnification (a), average reflectance (b), and mode radius at the crystal centre (c) as a function of GRM ($n = 2$, super-Gaussian) reflectance profile radius, w_{GRM}, for the $M = -1.5$ resonator. Again, the focal length of the thermal lens is 25 cm and $w_{pp} = 1.1$ mm. R_o is assumed to be 66.7%, as given by Equation 2.13.

A crystal centre mode radius of 1.1 mm is obtained using a GRM profile radius of 1.2 mm. This gives a predicted magnification of -1.32 and an average reflectance of 52.5%.

Finally, the average reflectance can be increased to give an appropriate average reflectivity specified in section 6.1.1. Increasing R_o to 76% satisfies the maximally flat near-field profile condition (for the predicted $|M|$ of 1.32) and results in an average reflectance of 60%, which yields an acceptable output coupling fraction for the travelling-wave resonator described in this Chapter. An almost $1/M$ dependence between $\overline{R}$ and R_o, as might be expected from Equations 2.13 and 2.14, was predicted by the Fox-Li model indicating that the GRM radius was not too large for the gainmask used.

Figure 6.14 shows the predicted intensity (left) and corresponding phase (right) profiles for the travelling-wave unstable resonator model. These profiles show the intensity and phase distributions at the centre of the crystal (A2) (a), just before aperture A1 (b), immediately after reflection from the GRM (c), and in the near-field (d).

The central region of the phase profile in Figure 6.14(c) was fitted to determine

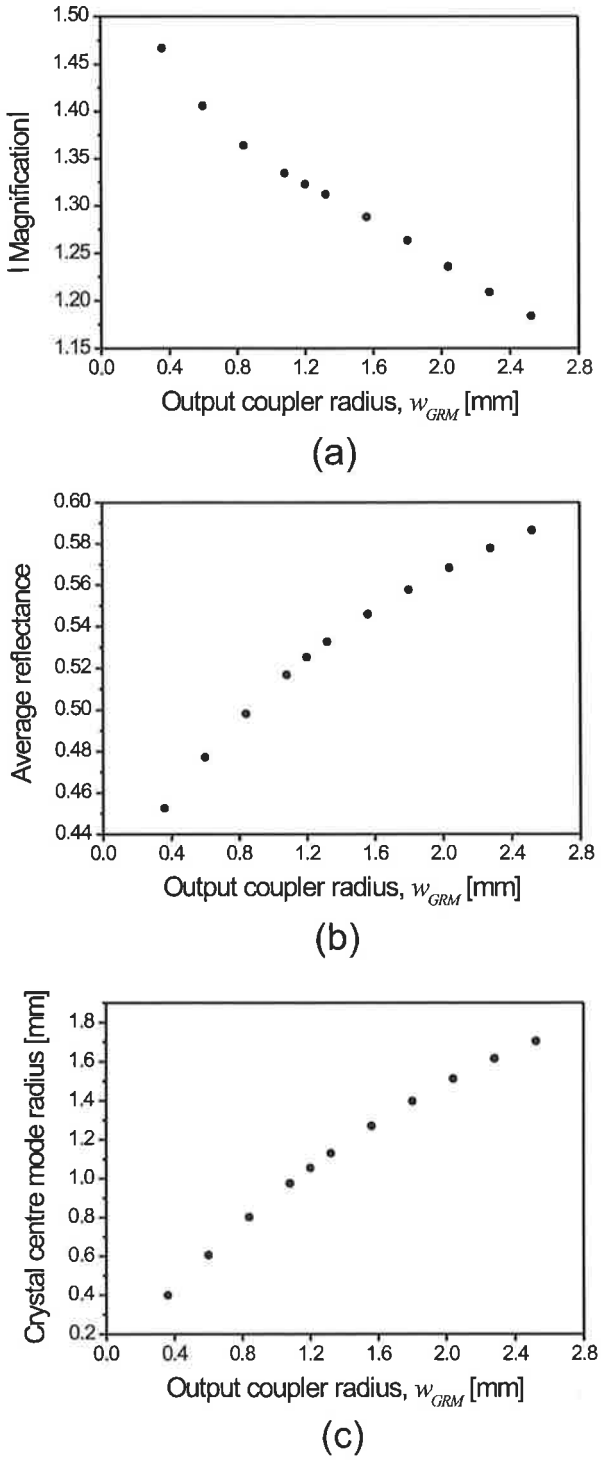

Figure 6.13: Magnification (a), average reflectance (b), and mode radius at the cystal centre (c), for a fixed thermal lens focal length of 25 cm, $w_{pp} = 1.1$ mm, and $M = -1.5$ as a function of the GRM ($n = 2$, super-Gaussian) output coupler reflectance profile radius, w_{GRM}. $R_o = 66.7\%$.

the wavefront radius of curvature of the unstable resonator mode immediately after reflection from the GRM, and was found to be 54.5 m. Figure 6.8 shows the transverse dimensions of a Gaussian beam (TEM_{oo}), as a function of position within the $M = -1.5$ travelling-wave unstable resonator with the same initial intensity profile radius and wavefront radius of curvature as immediately after reflection from the GRM.

To assess the beam quality, the M^2 beam quality factor (no relation to the magnification, M) was determined. The propagation formula for an arbitrary unabberated real laser beam in one transverse dimension ($x-$direction) as a function of distance (z), is given by[96][97]

$$W^2(z) = W_0^2 + \left(M^2\right)^2 \times \frac{\lambda^2}{\pi^2 W_0^2}\left(z - z_0\right)^2 \tag{6.11}$$

where W_0 is the beam radius at the waist, z_0 is the $z-$location of the waist and M^2 is the beam quality factor. The near-field distribution in Figure 6.14(d) was propagated through a positive lens of focal length 1 m to several locations along the z-axis (the direction of propagation). The radius was determined at each location using the second moment of the intensity distribution ($\sigma_s^2 = W^2/4$). Figure 6.15 shows the predicted beam radius as a function of propagation distance after passing through the 1 m lens (located at $z = 0$). The predicted data in Figure 6.15 was fitted using Equation 6.11 yielding the M^2 beam quality factor, the result of the fit is also plotted in Figure 6.15. The number of data points at and near the beam waist was increased to ensure accurate determination of the location and beam radius at the waist. The predicted M^2 is 1.0660.

Figure 6.16 shows the intensity (left) and phase (right) profiles at the $z-$position of the fitted waist (a) and at $z = 1$ m (b), after passing through the lens with a focal length of 1 m. The combination of uniform phase over the main intensity lobe in Figure 6.16(a), coupled with the negligible side-lobes and the M^2 near 1 indicates the excellent beam quality of the unstable mode. This also indicates the absence of significant higher-order modes as these would degrade these properties if they were present. For comparison, the beam quality of unstable resonators discussed earlier

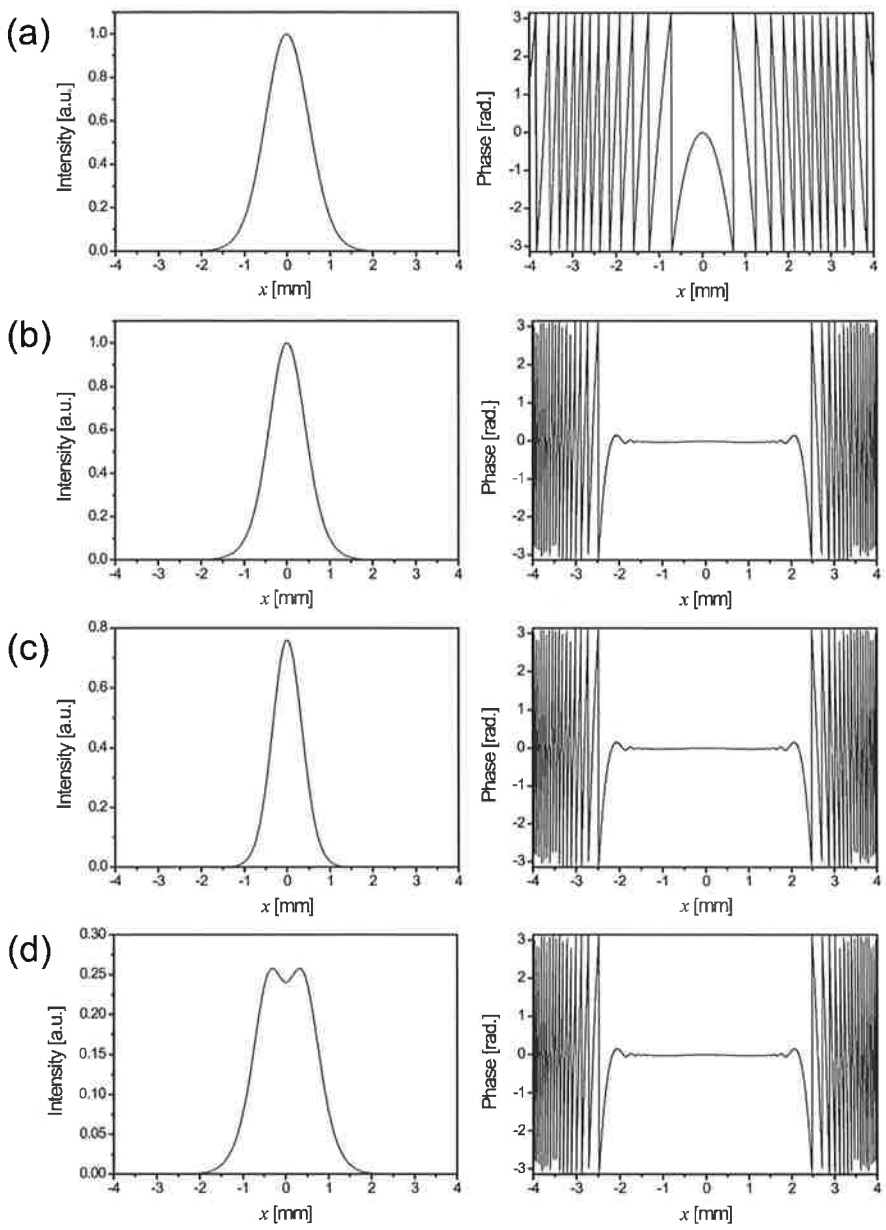

Figure 6.14: Predicted intensity (left) and corresponding phase (right) profiles for the travelling-wave unstable resonator model. Mode profiles show the intensity and phase distributions at the centre of the crystal (A2) (a), just before aperture A1 (b), immediately after reflection from the GRM (c), and in the near-field (d).

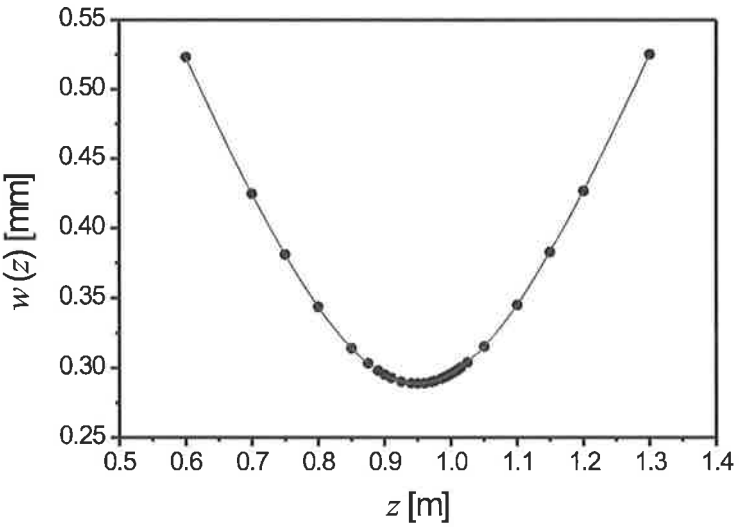

Figure 6.15: Predicted laser beam radius as a function of propagation distance. Geometric magnification = -1.5. Predicted $M^2 = 1.066$ (beam quality factor).

Geometric M	GRM, R_o	Predicted M	Predicted $\overline{R}$	Predicted M^2
-1.3	76%	-1.12	70%	1.0295
-1.5	67%	-1.32	52.5%	1.0223
-1.5	76%	-1.32	60%	1.0660

Table 6.3: Beam quality factor comparison for three different resonator models with different geometric magnifications and GRM peak reflectivities.

in this Chapter with a geometric magnification of -1.3 ($R_o = 76\%$) and a geometric magnification of -1.5 ($R_o = 67\%$) were determined, see Table 6.3. The predicted magnification and average reflectance determined from the Fox-Li model is included along with the M^2 factor that was calculated using the approach outlined above.

The beam quality experiences a marginal improvement when increasing the geometric magnification from -1.3 to -1.5. For a geometric magnification of -1.5, the beam quality decreased slightly when increasing the GRM peak reflectance, this is probably due to the small dip in the near-field shown in Figure 6.14(d). However, the increased average reflectance was necessary to achieve optimum output coupling.

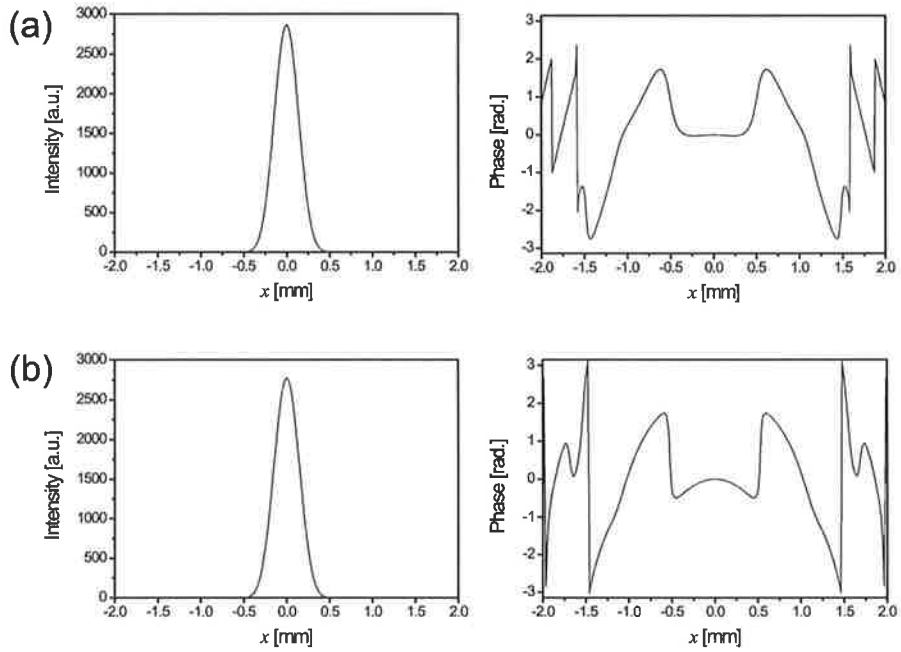

Figure 6.16: Intensity (left) and phase (right) at the z-position of the fitted waist (given by Figure 6.15) (a) and at $z = 1$ m (b), after passing through the lens with a focal length of 1 m.

6.4 Summary

The negative-branch confocal travelling-wave unstable resonator model presented in this Chapter demonstrated useful operation for a realistic range of thermal lens focal lengths. The reverse mode of the travelling-wave resonator was not considered here, since it will be suppressed by injection locking. Mode discrimination was accomplished by combining the well known reduced average reflectance of the GRM for the higher-order unstable resonator modes (see Chapter 2) and ensuring good overlap between the lowest-order mode and the gain region. The second feature is specific to the unstable resonator (and laser head) described in this thesis. Matching the gain distribution and the lowest-order mode of the unstable resonator reduces the available gain for the higher-order modes which typically have a significant fraction of their intensity that does not coincide with the resonator axis. Hence, the gain available to the higher-order modes is less than for the lowest-order mode which has it's energy located on or near the resonator axis. The specific pump geometry used in this thesis should therefore enhance the mode discrimination. Both of these effects increase the lasing threshold of the higher-order modes, thus providing mode discrimination.

The absence of higher-order modes was inferred from the low M^2 factors. Excellent beam quality from low magnification unstable resonators with GRM's has also been shown by other authors. McCarthy *et al.*[98] showed an unstable resonator which incorporates a GRM does not need a large magnification to be able to produce a good quality beam. Parent *et al.*[70] demonstrated that the use of a GRM can significantly improve the far-field power density.

The gain guiding properties of the gainmask were also investigated. Unless the GRM profile radius is significantly smaller than the gainmask radius, in general the resulting magnification is less than the geometric magnification. The reduced M results in a higher GRM average reflectance than would be expected in the absence of a gainmask. This allows the geometric M to be increased so that the predicted (real) magnification (including effects of the gainmask) can be adjusted to the desired value, thereby giving the appropriate $\overline{R}$.

Increasing the M value reduces the sensitivity of the resonator to perturbations

and misalignments. It is presumed that the geometric magnification determines the resonator sensitivity to misalignments and the actual magnification predicted by the Fox-Li analysis determines the resonator sensitivity to perturbations. This subject is left for further investigation after this thesis and can presumably can be investigated using the Fox-Li model incorporating E and F parameters to describe mirror misalignment.

It is commonly believed that low order GRM's result in poor extraction efficiency because the mode intensity is not as uniform as that for a higher-order GRM profile. However, Paré [99] has shown that the efficiency is not significantly affected by the order of the GRM. He shows that the uniformity of the mode produced by the high-order super-Gaussian may be compensated by the superior energy extraction in the axial region by a mode produced by a lower-order super-Gaussian. The disadvantage of the Gaussian GRM profile is therefore not that it has a poorer energy extraction efficiency due to decreasing mode intensity with radius, but that the mode has a greater spatial extent and may experience clipping by apertures[70]. In the laser design presented in this thesis, the apertures are significantly larger than the pump and mode regions, hence the gain medium is not expected to aperture the mode. This feature allows a low order super-Gaussian ($n = 2$) to be used, which suits the pump profile. Furthermore, as shown in Equation 2.14, the lowest-order super-Gaussian profile gives the greatest $\overline{R}$ assuming a maximally flat near-field is required. Thus, it allows larger values of M to be used.

The work in this Chapter demonstrates the feasibility of travelling-wave design. To increase the accuracy of these models, gain saturation should to be included in the models.

Chapter 7 will present experimental evidence of stable-unstable resonator operation in a standing-wave, lower gain, subscale experiment and a comparison to a Fox-Li model of the resonator. The correlation between the experiments and predicted results is discussed.

Chapter 7

Standing-Wave Stable-Unstable Resonator

The aim of this Chapter is to demonstrate that the side-pumped, side-cooled zigzag slab geometry can be used in a CW stable-unstable resonator and that the predictions of the Fox-Li model are consistent with the observed performance. A sub-scale design verification experiment is described that uses a standing-wave resonator rather than a travelling-wave resonator, due to the limited diode-laser pump power (100 W).

The discussion in Chapter 6 assumed a larger pump power and pump volume than for the laser head described and characterized in Chapters 4 and 5. The single-pass gain-length product, $g_o l_g$, for the travelling-wave model in Chapter 6, (see Table 6.1) is a factor of 2.5 times greater than for the laser head in Chapters 4 and 5 (see Table 5.2). Furthermore, a travelling-wave resonator only single-passes the gain medium each round-trip, while a standing-wave resonator double-passes the gain medium. Therefore, since the stable-unstable resonator has a relatively large output coupling, the laser head in Chapters 4 and 5 is clearly not suited to a travelling-wave resonator as described in Chapter 6, especially with the increased loss within the crystal due to the crack.

This standing-wave resonator used a positive-branch unstable resonator, rather than the negative-branch resonator described in Chapter 6, as it was shorter and more compact than the travelling-wave resonator. Avoiding the intra-cavity focus

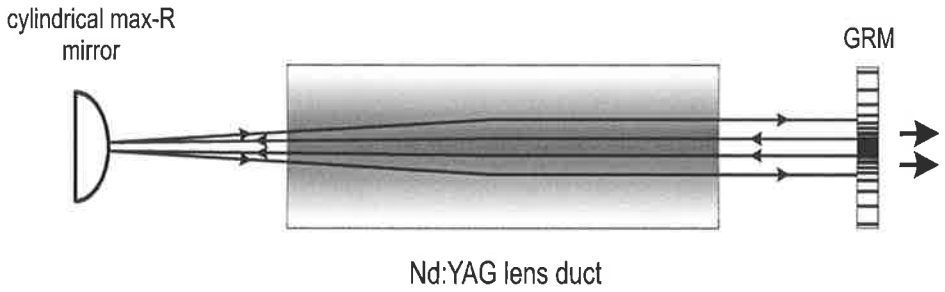

Figure 7.1: Standing-wave unstable resonator concept (vertical plane). The gain-medium is located between a cylindrical curved max-R mirror and the flat GRM.

allows the unstable resonator mode to have a better overlap with the gain region. The penalty for using the positive-branch unstable resonator is the greater sensitivity to misalignment.

The Fox-Li model of the standing-wave resonator is described in section 7.1. The approach is similar to that used in Chapter 6. The modifications to the experimental configuration described in Chapters 4 and 5 are discussed in section 7.2 and the experimental behavior of the standing-wave stable-unstable resonator is reported in section 7.3. Finally, the experimental results are compared to the prediction of the Fox-Li model, confirming the validity of the Fox-Li model.

7.1 Standing-wave unstable resonator model

A simplified representation of the unstable resonator investigated in this Chapter is shown in Figure 7.1. The resonator is stable in the horizontal plane and unstable in the vertical plane. The gain medium is located between the convex max-R mirror and a flat Graded Reflectivity Mirror (GRM). The layout of the standing-wave stable-unstable resonator is shown in Figure 7.2.

In Chapter 5 the pumped height in the slab is 1 mm, which is smaller than the minimum strip-GRM full-width of 1.58 mm ($1/e$ full-width) that can be produced by the GRM vendor (INO[1]). Thus, the height of the pumped region in the slab was increased by changing the vertical position of the arrays of fibres: the vertical

[1]National Optics Institute, 369, rue Franquet, Sainte-Foy, (Québec) Canada G1P 4N8. Tel. (418) 657-7006, Fax. (418) 657-7009.

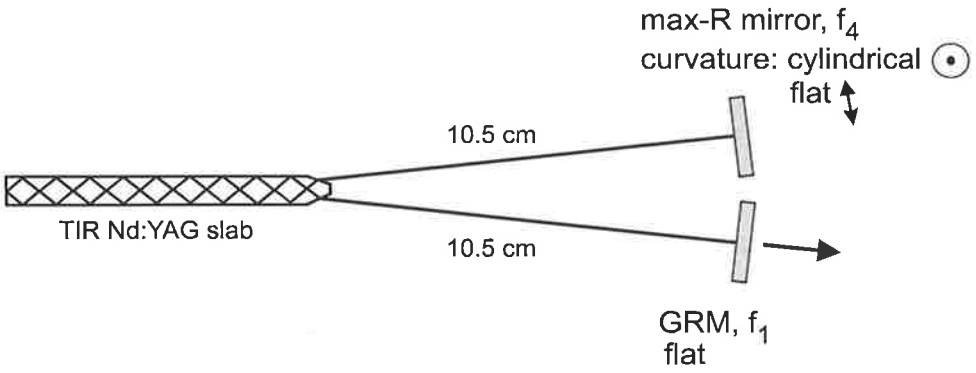

Figure 7.2: Standing-wave stable-unstable resonator layout. Cylindrical optics were used with curvature perpendicular to the page as shown here, the armlength is 10.5 cm.

position of the planar array of fibres on one side of the slab was increased by 300 μm, and the vertical position of the planar array of fibres on the other side was decreased by 300 μm.

In Chapter 6, a Gaussian GRM profile was assumed. However for this resonator a $n = 5$ super-Gaussian profile was used, since lower-order strip profiles were not available in a strip GRM that had the minimum full-width given above. The measured GRM profile is shown in Figure 7.3. The peak reflectivity is 77%, the reason for choosing this peak reflectivity was based on Fox-Li predictions that are described later in this section. The peak reflectivity of the GRM was not chosen to satisfy the maximally flat condition in this instance, as this would give an average GRM reflectance of 40% for $M = 1.3$ (see discussion in Chapter 2.3), which is significantly less than the optimum output coupling of 75% measured in Chapter 5.

The design sheet for the GRM supplied to the manufacturer, INO, is included in Appendix H. This shows the design parameters specified for the GRM and an appropriate set of tolerances.

The design parameters for the laser resonator are listed below:

- A standard curvature max-R cylindrical mirror was used, RoC = -152.6 mm.
- The resonator mirrors were 10.5 cm from the end of the slab, as this enabled efficient fundamental mode operation in the horizontal (stable) plane, as demonstrated in Chapter 5.

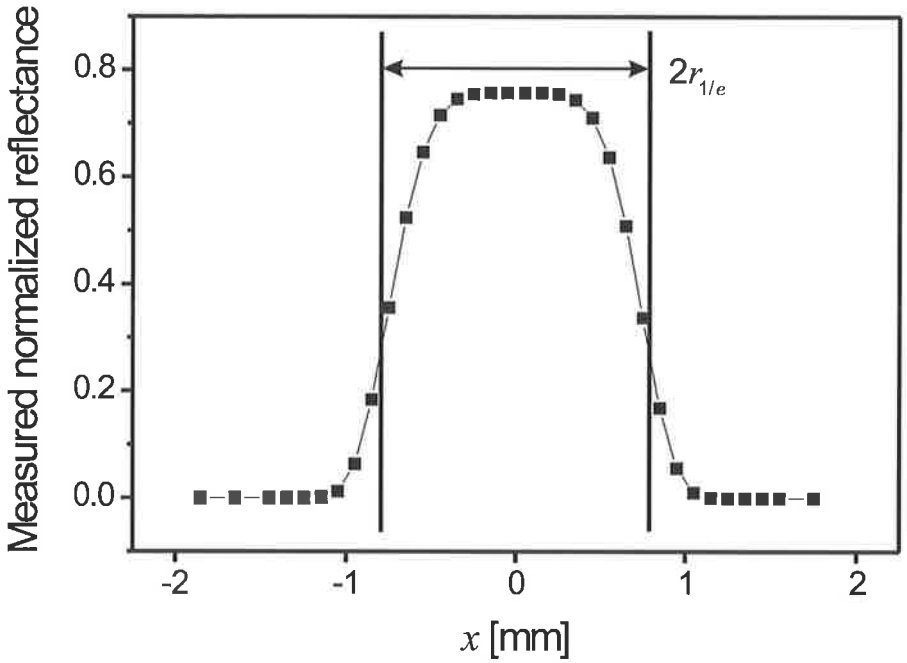

Figure 7.3: Measured GRM profile (■), manufactured by INO and fitted $n = 5$, super-Guassian profile (—), (see Eqn. 2.11). The two vertical lines indicate the $1/e$ diameter of the superguassian profile which is 1.58 mm. The profile was measured using a low power Nd:YAG laser (described in App. F) beam that was focussed onto the GRM and scanned across the profile.

- The strip-GRM was deposited on a flat AR coated substrate, due to time limitations, as this eliminated the need for custom-made radii of curvature substrates.

7.1.1 Horizontal plane - stable

The stable horizontal mode arises due to the weak horizontal thermal lens within the slab (see Chapter 5). A mirror distance of 10.5 cm from the end of the slab was chosen as justified previously.

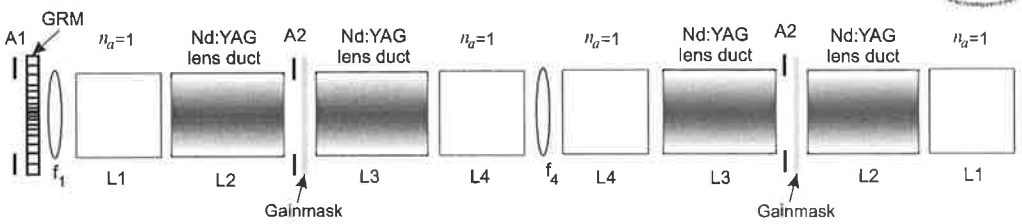

Figure 7.4: The basic model used for standing-wave unstable resonator Fox-Li calculations.

Parameter	Value
GRM aperture radius, A1	0.5 cm
Slab aperture radius, A2	0.17 cm
Geometric lengths L1 & L4	10.5 cm
Geometric lengths L2 & L3	4.5229 cm
Nd:YAG refractive index	1.8197
GRM cylindrical focal length, f_1	∞
GRM reflectivity profile function	$n = 5$ super-Gaussian
GRM reflectivity profile radius	0.79 mm $(1/e)$
max-R, cylindrical focal length, f_4	-7.63 cm
Nd:YAG lens duct focal length	variable, between 12 and 34 cm

Table 7.1: Quantities used for standing-wave unstable resonator Fox-Li calculations.

7.1.2 Vertical plane - unstable

Figure 7.4 shows the standing-wave Fox-Li unstable resonator model and Table 7.1 contains a summary of the parameter values. As described for the Fox-Li analysis in Chapter 6, a wave is propagated between apertures in the resonator using an ABCD matrix which describes the elements between the apertures. A1 is the GRM substrate aperture, and apertures A2 represent the bottom and top edges of the slab at the blunt end of the slab. The vertical magnification of the mode is provided by a combination of the convex max-R mirror and the thermal lens. The gain medium is modelled as a lens duct. The effective focal length of the lens duct is referred to as the thermal lens, f_{therm}, in the text here.

Gainmask model

As discussed at the beginning of this section, the height of the pumped region was increased to suit the GRM profile. The vertical staggering of the fibre arrays by ± 300 μm results in a near Gaussian pump profile (x-direction) and increases

the radius by 20%, compared to co-planar layers of pump fibres. To examine the effect of the height of the pumped region in the Fox-Li analysis, a range of Gaussian gainmask pump profile radii w_{pp} of 0.55, 0.66, 0.77, 0.94 and 1.22 mm were used in the following analysis. As in Chapter 6, the calculations using gainmasks are compared to a calculation with no gainmask to assess the influence of the gainmask on the unstable resonator.

Fox-Li analysis Figure 7.5 shows the predicted magnification (a), average reflectance (b) and the near-field beam radius (c) as a function of the focal length of the lens duct, with the radius of the gainmask as a parameter. The numbers 1 to 5 refer to configurations that are used later in the Chapter.

The stability diagram in Figure 7.6 indicates the resonator transition from positive-branch unstable through a stable region to a negative-branch region, as the pump power and associated thermal lens is varied. Short thermal lens focal lengths ($\lesssim$ 0.12 m) give rise to a resonator that is negative-branch unstable.

As the focal length of the thermal lens is increased the resonator approaches the stable region, as indicated by the point in Figure 7.5 that has magnification = 1. All of the gainmask models give the same result at this point. Furthermore, the average reflectance is almost the same as the peak reflectance of the super-Gaussian output coupler. This indicates the laser mode lies in the center of the output coupler reflectivity profile.

As the focal length of the thermal lens is further increased the resonator again becomes unstable, but in the positive-branch region of the stability diagram, and the magnification increases. As expected, the average reflectance decreases with increasing magnification (see Equation 2.14), and the near-field beam radius increases. As the magnification of the unstable resonator increases, the influence of the gainmask also increases, due to gain guiding. A qualitative comparison between these predictions and the measured results is given in the next section.

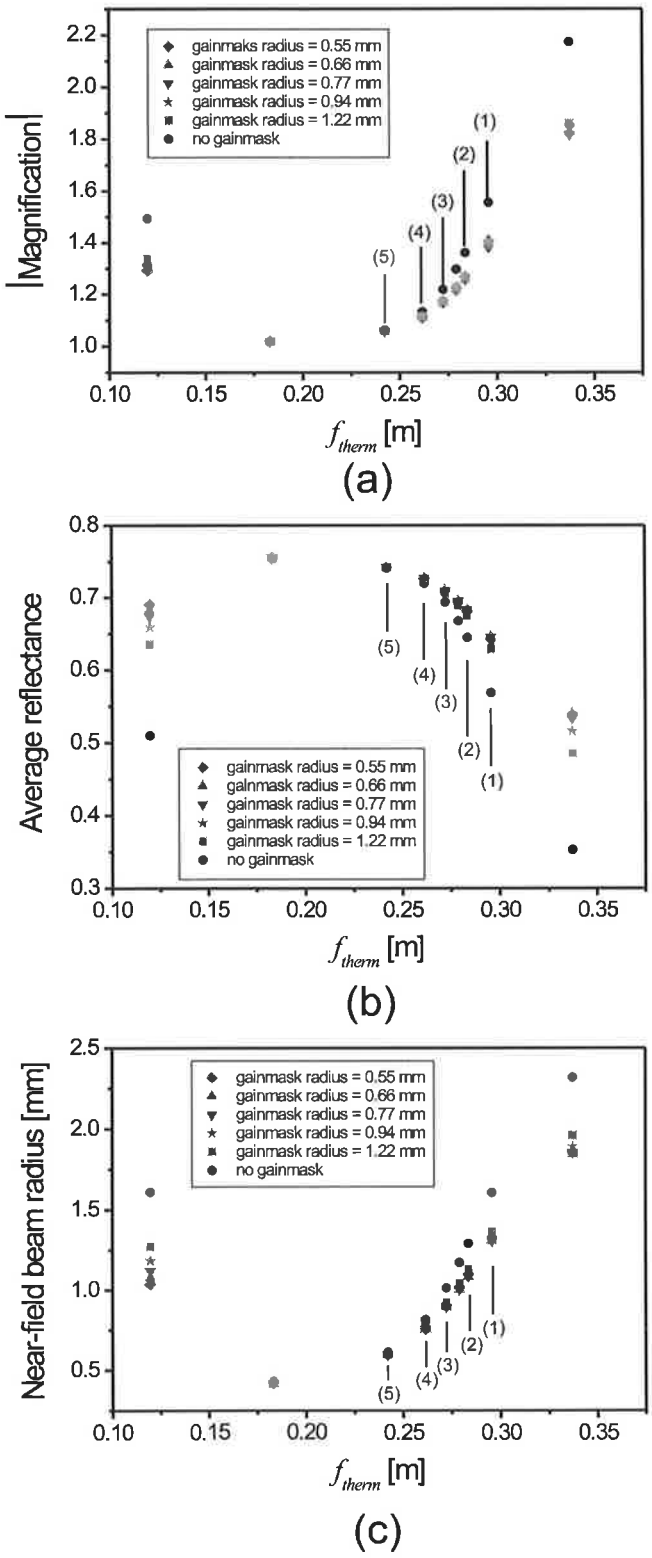

Figure 7.5: Predicted magnification (a), average reflectance of the GRM (b) and near-field beam radius (c) as a function of the focal length of the thermal lens for mirror curvatures $f_1 = \infty$ and f_4 = -7.63 cm. Each set of data points correspond to a different gainmask.

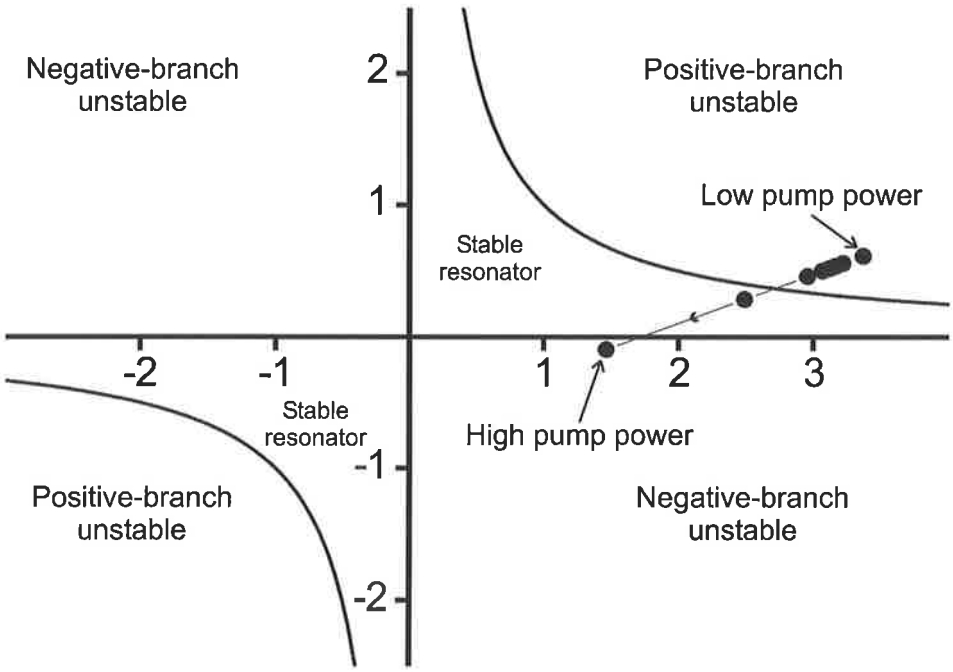

Figure 7.6: Resonator stability diagram (g-diagram) showing the resonator g-parameters with changing pump power. At low pump powers, which result in long focal lengths, the resonator is positive-branch unstable. As the pump power is increased, the resonator becomes stable before crossing the axis finally becoming negative-branch unstable, for short thermal focal lengths.

7.2 Experimental configuration

The laser head used to investigate the standing-wave stable-unstable resonator is similar to that described in Chapters 4 and 5. The most significant change is the TEC's have been replaced by 'heat-bars', as shown in Figure 7.7. This was done to enable increased heating of the bottom and top of the slab, which allows the vertical thermal lens focal length to be increased more than when using the TEC's.

To increase the heating capacity at these surfaces Pyrotenax[2] MI heating cable was mounted in copper heatsinks to produce the heat-bars. Pyrotenax MI cable consists of nichrome wire with a nominal resistance of 10 Ω/m inside a stainless-steel sheath. The core is electrically insulated but not thermally insulated from the sheath by a highly compressed mineral insulant. The heating capacity of the wire is 390 W/m at 20 °C. The estimated maximum heating capacity of each heat-bar was 8-12 W, which was greater than the 4 W of the TEC. A thin stainless-steel sheathed thermocouple was also mounted in the copper to replace the bulky thermistor which was used with the TEC's. A stainless-steel spacer was used to thermally insulate the 'heat-bar' from the lower temperature of the laser head mount, and to give the same dimensions as before.

7.3 Experimental results

Operation of the unstable resonator can be demonstrated by either adjusting the pump power to provide the required thermal lens or by using the heat-bars to adjust the thermal lens at high pump power. Plate # 6(A)-(E) and Plate # 7(F)-(I) show the near-field (left) and far-field (right) beam profiles measured as the pump power increased. The near-field profiles were measured by imaging the strip GRM output coupler onto a CCD (see Figure 7.10). The far-field profiles were measured by a CCD located at the focal plane of a positive lens. The horizontal parallel lines on the near-field profiles in Plates # 6 and # 7 represent the $1/e$ full-width of the GRM. Corresponding parallel vertical lines are also included on Figure 7.3. The

[2]Manufactured by BICCGeneral Pyrotenax Cables Ltd., 7037 Fly Road, East Syracuse, N.Y., 13057, U.S.A.

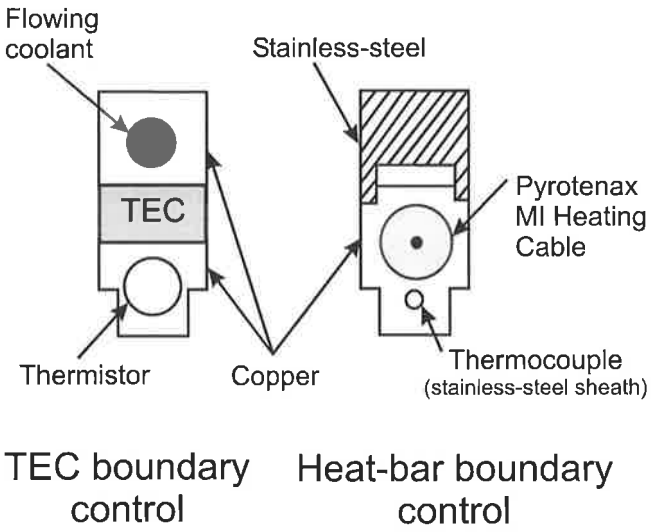

Figure 7.7: End view showing the modification of the TEC temperature control of the bottom and top of the slab, to the heat-bar system.

Diagram designator	Pump power (W)	Laser power (W)
A	74.3	6.9
B	76.5	8.5
C	78.7	10.5
D	80.8	11.1
E	83.0	11.7
F	85.1	12.0
G	87.3	12.3
H	89.5	13.9
I	91.6	14.5

Table 7.2: Pump power and laser output power for pictures A-I, in Plates 6 and 7.

pump and laser powers for each profile are given in Table 7.2. These powers are difficult to compare with previous results due to the crystal fracture and resulting increased intra-cavity loss.

At low pump powers, the focal length of the thermal lens is long and thus the resonator is positive-branch unstable with a large M. The near-field spot size is thus much larger than the GRM profile, as shown in Plate # 6(A). Note that the resonator at this point is over-coupled, and this results in a poor efficiency.

As the pump power is increased, and the thermal lens focal length is reduced, the magnification decreases and the width of the near-field profile approaches the width of the GRM. Eventually, the resonator becomes stable shown in Plate # 7(F)-(G),

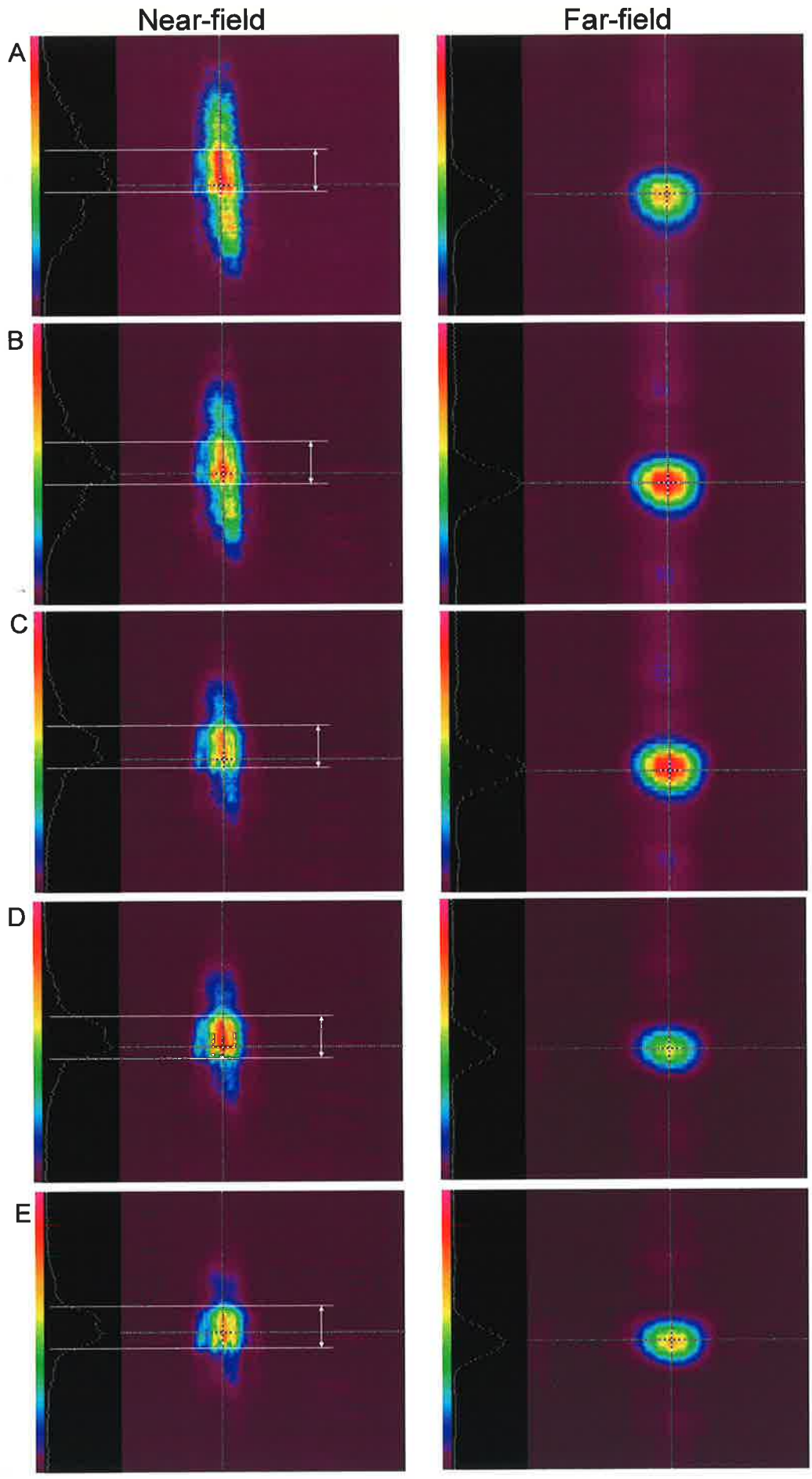

Plate # 6

Near- and far-field beam profiles. The near-field was measured by imaging the strip GRM output coupler onto the CCD plane. The far-field was measured using a CCD at the focal plane of a positive lens. The far-field profiles were measured concurrently with the near-field measurements. Each case denoted A-E was a different pump power, as specified in Table 7.2. The horizontal parallel white lines represent the $1/e$ diameter of the strip-GRM profile.

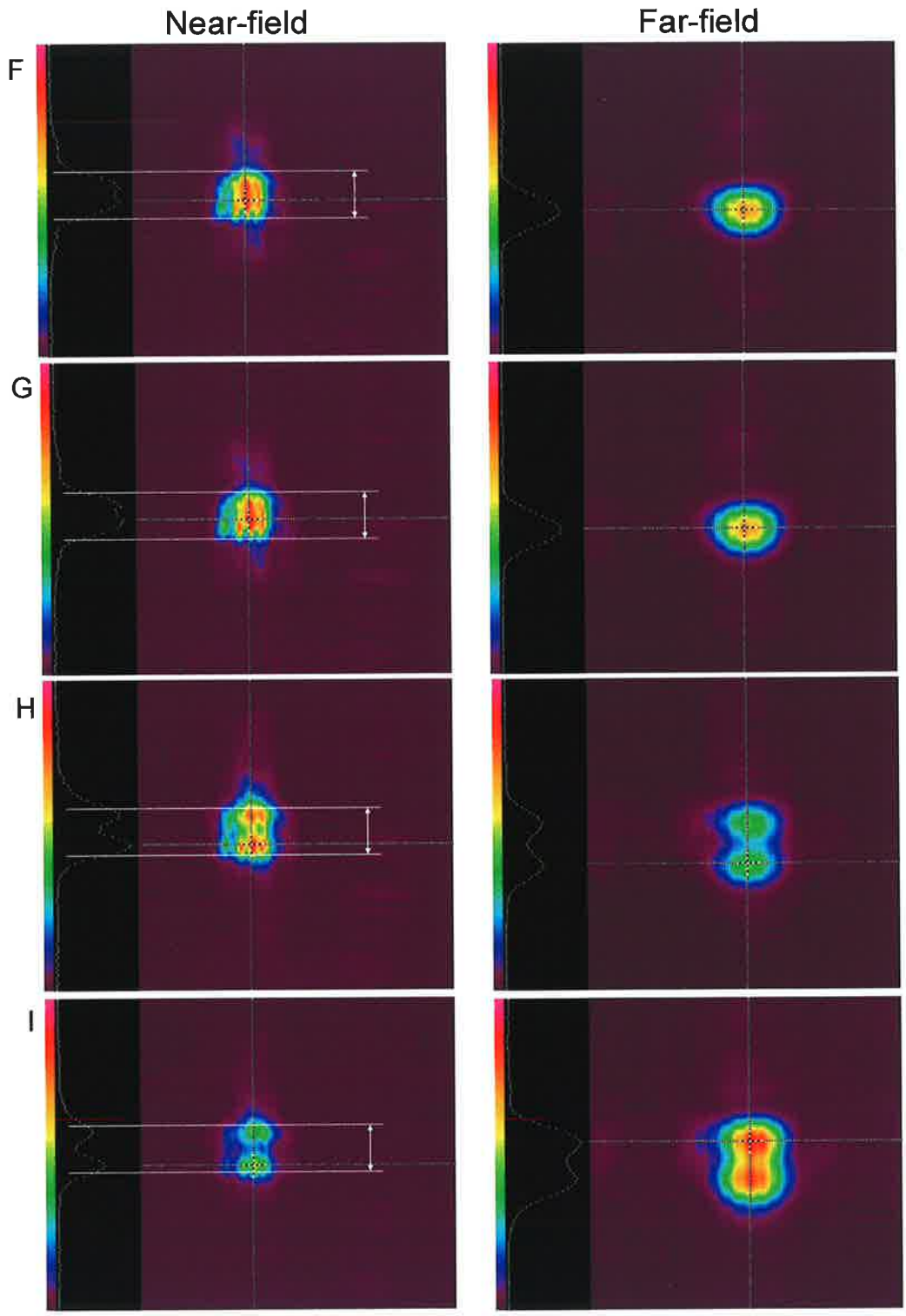

Plate # 7

Near- and far-field beam profiles. The near-field was measured by imaging the strip GRM output coupler onto the CCD plane. The far-field was measured using a CCD at the focal plane of a positive lens. The far-field profiles were measured concurrently with the near-field measurements. Each case denoted F-I was a different pump power, as specified in Table 7.2. The horizontal parallel white lines represent the 1/*e* diameter of the strip-GRM profile.

with the mode lasing off the centre of the GRM profile. In Plate # 7(I), a TEM_{01} mode is favored by the laser.

The behavior shown in Plates # 6 and # 7 agrees with that shown in Figure 7.5: starting at the right-hand side of the curve (long thermal lens focal lengths, similar to Plate # 6(A)), and moving toward the left side (shorter thermal lens focal lengths, similar to Plate # 7(I)). Figure 7.8 shows a comparison of predicted and measured near-field intensity profiles. The near-field intensity profiles of Plate # 6(A)-(E), are represented as dashed (|) curves in Figure 7.8(A)-(E). The predicted near-field profiles that most closely match the measured results, marked on Figure 7.5 by indicators (1)-(5), are also plotted on Figure 7.8(A)-(E) using ∇. The qualitative correlation between the measured and predicted profiles is moderately good. There is evidence of a step on the side of the peak of predicted curve (1) and also in the measured near-field profile (A). This can also be observed with predicted curve (2) and profile (B). Some difference between the predictions and measurements is expected since the calculations do not include gain saturation, or losses and wavefront distortion due to the crack. Nevertheless, it appears that the laser operated with $M = 1.3$ somewhere between models (1) and (2), for which the far-field beam quality was good. Unfortunately, the focal length of the thermal lens could not be measured concurrently with the lasing and thus a more precise comparison was difficult.

At maximum pump power, the resonator was stable. The heat-bars were used to increase the focal length of the thermal lens. The results are shown in Figure 7.9. Profile J corresponds to a pump power of 91.6 W with no heating by the heat-bars. Adding heat using the heat-bars significantly improved the far-field beam quality, as shown by profile K, with only 8% reduction in the output power.

It is unclear whether the resonator was unstable when it produced profile K, but it is clear that further increase in the focal length of the thermal lens would result in an unstable resonator that has near-field beam profiles similar to that shown in Plates # 6(A) and (B). The heat-bars therefore provide tunability of the resonator properties necessary for this work and are an appropriate replacement for the TEC's where large heat generating capacity is required.

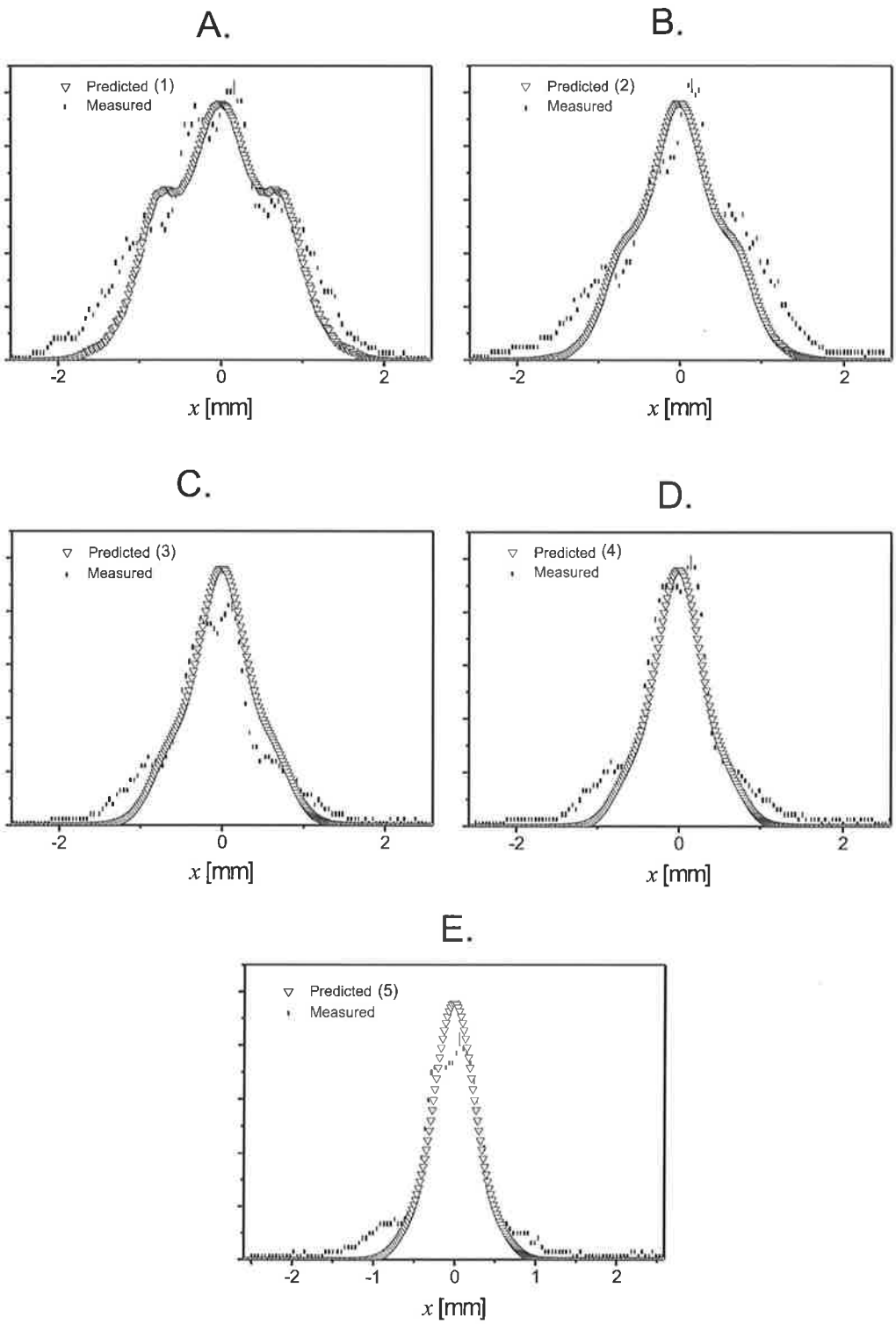

Figure 7.8: Qualitative comparison of predicted (∇) and measured (|) near-field intensity profiles. Figures A - E show the identical measured intensity curves (|) in the vertical (x-) direction to those in Plate # 6(A)-(E). The curves calculated using the Fox-Li model (∇) are shown in Figure 7.5 by numbers (1) to (5). The vertical axis is intensity and has arbitrary units.

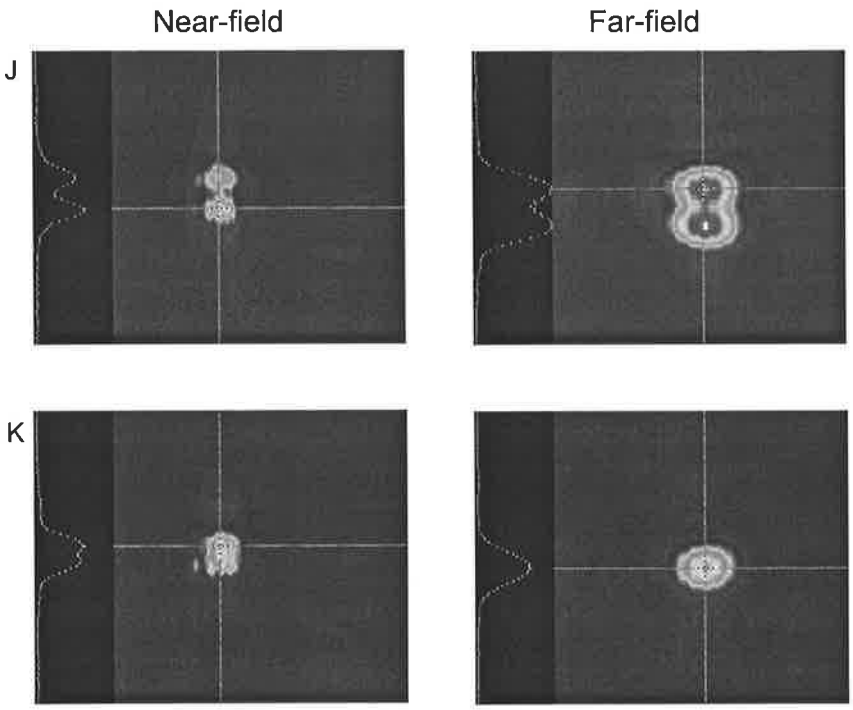

Figure 7.9: Near- and far-field beam profiles with heat-bars off (J) and heat-bars on (K), constant pump power of 91.6 W.

7.4 Injection locking

As discussed in Chapter 1, the long-term aim of this work is to injection lock the travelling-wave stable-unstable resonator. In this section single frequency operation of the standing-wave stable-unstable resonator is shown by injecting power from a NPRO master laser. Figure 7.10 shows the experimental setup used. The appropriately polarized, 500 mW NPRO master laser beam passes through mode-matching optics and a Faraday rotator before entering the slave cavity through the GRM. The slave and master laser fields travel back through the Faraday rotator and are rejected by one of the polarizers. The output is monitored using a power meter and a scanning Fabry Perot cavity (10 GHz FSR). The output of the slave resonator could also be monitored in the near- and far-fields in order to set the operation of the resonator.

The free running spectrum of the slave cavity is shown by Figure 7.11(A). Note the multiple longitudinal modes, which are separated by the FSR of the slave resonator (440 MHz).

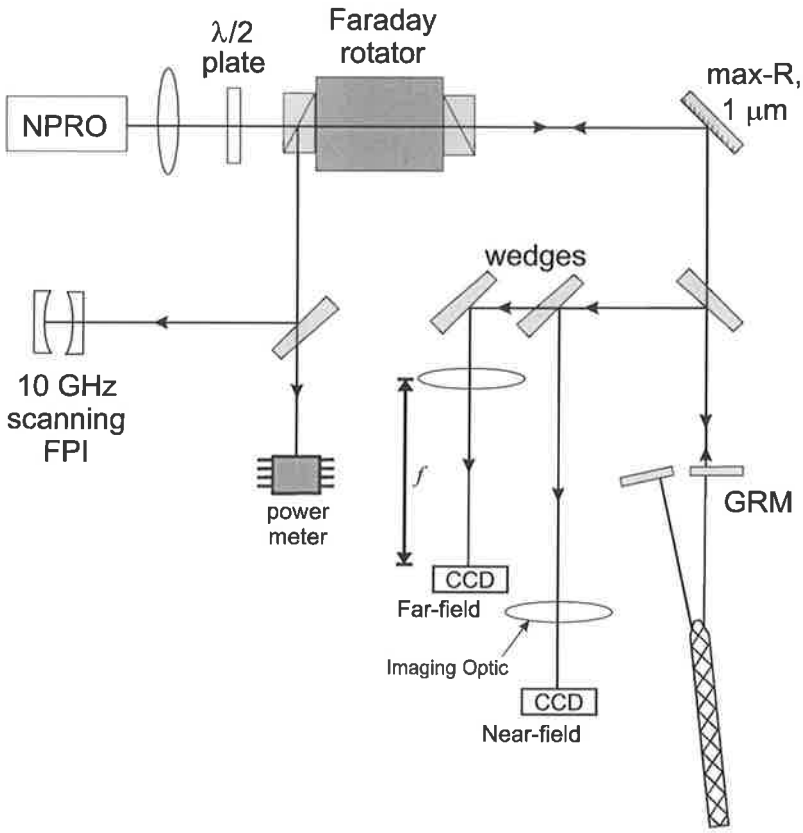

Figure 7.10: Experimental setup for single frequency operation.

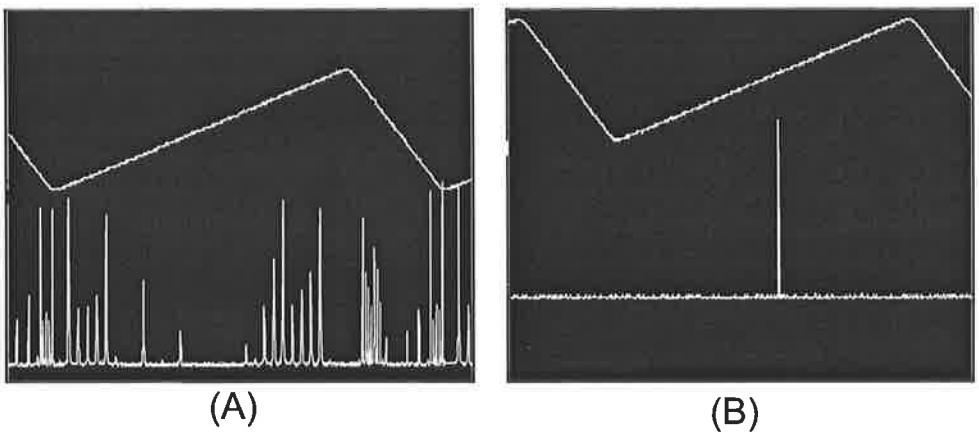

Figure 7.11: Multimode operation of free-running slave resonator (A) and evidence of single-frequency operation when seeded with master oscillator (B). The triangular waveform illustrates the sweep rate of the FPI in each case.

The temperature of the master and slave gain media were set so that they were similar, and the frequency of the NPRO was swept over a frequency range of 270 MHz. The frequency of the NPRO frequency sweep was 5-10 kHz. At some frequency within the sweep, the frequency of the NPRO coincided with the frequency of one of the longitudinal modes of the slave laser. The NPRO was then regeneratively amplified, which saturated the gain below threshold for free-running oscillation. Figure 7.11(B) shows a typical spectrum indicating that all except one mode was suppressed.

7.5 Summary

The measured near-field profiles in Plates # 6 and # 7 clearly indicate that the mode size is larger than the diameter of the GRM, indicating a magnification larger than one, and that the mode produced by this resonator has good far-field beam quality. Although direct comparison was not possible since the thermal lens of the resonator could not be measured concurrently with lasing, specific calculated examples were compared to measured results and showed good qualitative agreement. This verified that the stable-unstable resonator could be operated with a geometric magnification of 1.3, and that the Fox-Li modelling gives a good indication of the behavior of the

resonator even though gain saturation effects were not included. The output power could not be compared to Chapter 5 due to the crack in the crystal.

Injection locking of the stable-unstable resonator was also demonstrated by injection of a master field into the slave cavity.

Chapter 8

Conclusion

This thesis has presented a high power diode-laser-pumped, CW Nd:YAG slab laser design that uses a stable-unstable resonator. The idea to use a stable-unstable resonator for producing high quality, high power, CW laser beams from a Nd:YAG gain medium was first described by this author[1]. Proof-of-principle experiments have demonstrated that the laser head works as designed, and that the stable-unstable resonator design is well suited to both standing-wave and travelling-wave resonators.

This is the first side-pumped and side-cooled implementation of the efficient TIR zigzag CW laser geometry developed by Richards and McInnes[23]. The co-planar pumping and heat removal of the side-pumped, side-cooled design allows the height of the mode to be increased in the vertical direction orthogonal to the zigzag plane. Avoiding cooling the bottom and top surfaces of the slab results in reduced thermal lensing in the vertical plane, with the major thermal gradient in the horizontal plane. The zigzag path averages the refractive index variations in the horizontal plane, resulting in minimal net horizontal thermal lensing.

Subscale experimental investigations showed that the net horizontal thermal lens was indeed weak, indicating that the zigzag path was successfully averaging the horizontal thermal gradients. The thermal lens in the vertical direction could be adjusted by using TEC's which were placed on the bottom and top of the slab to heat or cool these surfaces. The range of the focal length of the thermal lens could be set between 47 mm and 450 mm. This adjustability allowed the resonator design to

be optimized. Furthermore, the horizontal and vertical thermal lenses were shown to be decoupled which allowed the mode height to be increased in the vertical direction and allowed simple power scaling of the laser head.

The efficiency of the laser head was investigated using a short, flat-flat, stable resonator. The slope efficiency of the laser was 37%, and the multimode power was 32 W using 100 W of pump power. Increasing the length of the resonator and using the slab apertures to provide horizontal mode discrimination produced a near diffraction limited TEM_{oo} output power of 20 W. Thus a compact stable laser was demonstrated. Most importantly, the laser head design operated successfully, with good thermo-optic control of the gain medium and good efficiency.

A strip, $n = 2$ super-Gaussian GRM was found to be the optimum output coupler for the stable-unstable laser, due to the limited gain of CW Nd:YAG. The average reflectance of the GRM is a factor of M larger for a strip GRM (1-D) than for a toroidal or spherical GRM (both 2-D). Since there is no mode discrimination penalty using the lower-loss strip geometry, this allows M to be maximized, which improves the mode discrimination and beam quality. Furthermore, it was found that the output coupling loss associated with a magnification of -1.3 could be sustained using pump densities below the crystal fracture limit. Travelling-wave unstable resonators with a similar magnification were assessed using a Fox-Li model. Useful operation over a realistic range of thermal lens focal lengths was predicted.

Mode discrimination is accomplished by combining the reduced average reflectance of the GRM for the higher-order unstable resonator modes and ensuring good overlap between the lowest-order mode and the gain region. It was shown that the lowest-order mode can be matched to the gain distribution. This reduces the available gain for the higher-order modes which typically have a significant fraction of their intensity that does not coincide with the resonator axis. The absence of higher-order modes was confirmed by the excellent M^2 beam quality factor produced by the low magnification unstable resonator.

The gain guiding properties of the gainmask in the Fox-Li model were also investigated. Unless the GRM profile radius was significantly smaller than the gainmask radius, the resulting magnification was less than the geometric magnification in

general. It presumed that the geometric magnification determines the sensitivity to misalignment and that the predicted magnification determines the perturbation stability. This is left for further investigation.

A subscale experimental investigation of a standing-wave stable-unstable resonator was performed using the available crystal and available diode-lasers, and is described in Chapter 7. A standing-wave resonator was chosen due to the limited gain. The resonator was shown to lase with magnification up to and greater than the design point of 1.3, by using pump power to control the focal length of the thermal lens. The measured far-field beam quality was excellent, particularly at high magnifications.

A qualitative comparison of the measured near-field beam profiles and the predicted near-field profiles was presented. This gives some indication that the Fox-Li model accurately predicts the behavior of the experiment. Unfortunately, the efficiency of the unstable resonator could not be assessed due to a crack which developed in the gain medium. Finally, an injection locking experiment was conducted using the stable-unstable resonator. Suppression of the multiple longitudinal modes was observed resulting in stable-unstable resonator operation at a single frequency.

The results in this thesis have successfully shown the viability of our high power laser design. Experiments are currently underway to investigate the use of the travelling-wave stable-unstable resonator as described in Chapter 6, using a higher aspect ratio slab and a pump power of 500 W.

Appendix A

Explanation of Fresnel Numbers

Fresnel numbers are routinely used to discuss the effects of apertures in optical resonators. The exact Fresnel number used depends upon the type of laser resonator. This section is intended to illustrate to the reader some definitions and relationships between different Fresnel number definitions used here and in the literature. For the simplest case of a two mirror resonator, the Fresnel number is a dimensionless quantity describing the number of Fresnel zones across one of the end mirrors, as seen from the centre of the other mirror in the resonator[100].

Ordinary Fresnel Number

$$\mathrm{N}_f = \frac{a^2}{\lambda \mathrm{B}}$$

where: a is the aperture radius, the half-width of hard-edged output coupler.

λ is the optical wavelength of the laser.

B is the 'B' element from the overall ABCD matrix of the laser resonator.

Collimated Fresnel Number

$$\mathrm{N}_c = M.\mathrm{N}_f = \frac{Ma^2}{\lambda \mathrm{B}}$$

where: M is the magnification of the unstable resonator, given by:

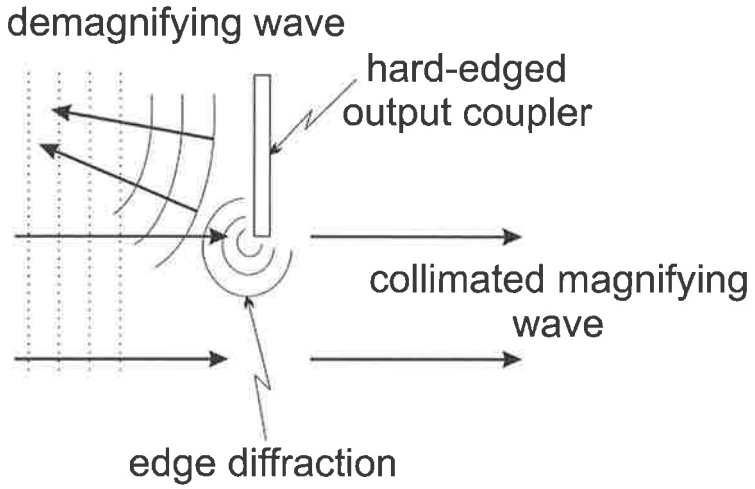

Figure A.1: Edge diffraction at the aperture scatters energy from the magnifying wave into the demagnifying wave.

$$M = m + \left(m^2 + 1\right)^{\frac{1}{2}}$$

where: $2m$ = (A+D) is the trace of the round-trip matrix.

Equivalent Fresnel Number Figure A.1 shows edge-diffractive scatter of the magnifying wave into the direction of the demagnifying wave. This scatter is demagnified into the core of the resonator until it becomes small and diffraction dominates. It then spreads away from the resonator axis forming a magnifying wave. The equivalent Fresnel number for an unstable resonator gives the relative phase shift between the magnifying and demagnifying eigenwaves at the hard-edge of the output coupler.

$$\begin{aligned} \mathrm{N}_{eq} &= \frac{(M^2-1)}{2M^2}\mathrm{N}_c \\ &= \frac{(M^2-1)}{2M}\mathrm{N}_f \\ &= \frac{(M^2-1)}{2M}\frac{a^2}{\lambda \mathrm{B}} \end{aligned}$$

Gaussian Aperture Fresnel Number

$$\mathrm{N}_{ga} = \frac{w_{ga}^2}{\lambda \mathrm{B}}$$

where: w_{ga} is defined by the amplitude reflectivity profile $r(x) = \exp[\frac{-x^2}{w_{ga}^2}]$ of a GRM.

Appendix B

Choice of Nd^{3+} Host Material

B.1 Introduction

It is often stated that YAG is the best host material for high power solid-state lasers yet we could not find a comprehensive comparison of possible Nd-hosts. Many authors discuss selected groups of host materials but there are few comparisons of the spectroscopic and thermomechanical properties of both established and newly emerging materials.

While the spectroscopic properties of the gain medium are important, it is the thermomechanical properties of the host medium which limits the power scalability of most CW solid-state lasers. The important thermomechanical properties will be introduced in section B.2, and the choice of the most suitable host material is discussed in section B.3. We will compare the properties of YLF, YAP, Glass, YAG, YVO_4, GSGG:Cr, KGW, BeL, S-VAP, CWO, NGWO and SGGM. We include S-VAP and YVO_4 for comparison only, as these materials, along with YOS and S-FAP, are more suited to microchip lasers[101][102]. Chromium-doped GSGG is also included for comparison even though the absorption bands of the Cr^{3+} sensitizing ion do not match the emission band of GaAlAs diode-lasers. We also discuss the significance of cross-relaxation, Auger upconversion and excited state emission for the more important host materials.

There is often significant variation in the parameter values in the literature due to material impurities and imperfections, doping concentrations, and varying growth

and measurement techniques used by different investigators. The data in Tables I and II is a realistic summary of the thermomechanical and spectroscopic properties of the host media, and is therefore useful information for solid-state laser designers.

B.2 Thermomechanical Properties

The thermal gradients produced when heat is removed from the gain medium results in surface stresses. As the surface stress, σ_s, approaches the material fracture strength, σ_f, the probability of material fracture increases. For a side-pumped, side-cooled slab laser of infinite length and height, a thermal stress resistance parameter, R_s, can be defined by[14][25][76]

$$R_s = \frac{\sigma_f k\,(1-\nu)}{\alpha E} \tag{B.1}$$

where k is the thermal conductivity, ν is Poisson's ratio, α is the thermal expansion coefficient and E is the elastic modulus. The surface stress is then given by

$$\sigma_s = \frac{Qw^2\sigma_f}{12R_s} \tag{B.2}$$

where Q is the thermal power deposited in the slab per unit volume, and w is the slab width.

Unfortunately, values for R_s are not common in the literature due to the uncertainty in σ_f which depends strongly on surface quality. Marion[76] has demonstrated that up to a fourfold increase in σ_f could be obtained for GSGG, GGG and YAG compared to values obtained using standard polishing techniques. Further increase in σ_f could be obtained at the expense of optical flatness.

A more common alternative material parameter, M_s, given by[14]

$$R_s = \sigma_f M_s \tag{B.3}$$

is often specified. Values of M_s and typical values of σ_f (where known) are listed in Table I along with thermal conductivities and refractive-index temperature coefficients ($\mathrm{d}n/\mathrm{d}T$) for the host media.

B.3 Discussion

While the thermomechanical properties are of fundamental importance in the design of high power lasers, the spectroscopic properties, summarized in Table II, are also important as they affect the efficiency and compactness of the high power diode-laser pumped solid-state laser (HPDPSSL). Ideally, the gain medium should have a large gain-length product ($g_o l$). Maximizing the gain-length product can be achieved by either increasing the pathlength within the gain medium, l, or by maximizing the small-signal gain coefficient, g_o. Zigzag optical paths are a practical way of increasing the pathlength within the gain region, but the slabs must have highly polished sides to minimize scatter from residual roughness. If the pathlength becomes too long then the intracavity losses due to bulk absorption and scattering within the material increase, thereby decreasing the efficiency and increasing the lasing threshold. The need for high optical quality, low distortion materials is thus apparent.

The small-signal gain coefficient is proportional to the stimulated emission cross section, $\sigma_{\mathrm{emission}}$, and the population inversion density which is, in turn, determined by the pump rate and the spontaneous emission lifetime of the upper state, τ_f. Thus, the $\sigma_{\mathrm{emission}}\tau_f$ product is an important spectroscopic parameter.

The pump rate can be maximized by using a material that has a large pump-absorption coefficient and an absorption band that is broader than the emission spectrum of the diode-laser, or by simply pumping more intensely. YVO_4 and S-VAP have high absorption coefficients, low thresholds (high $\sigma_{\mathrm{emission}}\tau_f$), good efficiency and polarized output, however they have poor thermomechanical properties.

High absorption coefficients in other hosts can be attained by increasing the concentration of Nd-ions. However, materials such as YAG experience fluorescence quenching at high Nd^{3+}concentrations, due to local distortions in the crystal matrix caused by a size mismatch between the neodymium-ion and the YAG lat-

tice. Neodymium doping in YAG is therefore limited to approximately 1.1 at. %. This problem is not shared by all Nd host media; higher Nd-concentrations can be achieved in materials like KGW where the ionic radius of Gd^{3+} closely matches that of Nd^{3+}[103], with up to 10% neodymium-doping being reported by Moncorgé *et al.*[104]. However, KGW has a low thermal conductivity.

If the absorption band of the dopant is narrower than the diode-laser emission band then the effective absorption coefficient is less than that shown in Table II. For example, our measurements for diode-pumping Nd:YAG (1.1 at.%) with diode bars (3-4 nm linewidth) indicate an effective absorption coefficient of approximately 4 cm^{-1}. Another significant practical advantage of a broad absorption band is that it simplifies the temperature control of the diode-laser.

Intense pumping can be achieved by using multiple fibre-coupled diode-lasers [3][5] or by focusing the pump light from arrays of diode-lasers using beamshaping lenses or non-imaging lens ducts[105]. However, the material fracture strength could be exceeded even in materials like YAG, which has the best thermomechanical properties (thermal conductivity) in Table I. Also, intense optical pumping increases the inversion density toward regimes where parasitic energy transfer processes occur. Mechanisms such as cross-relaxation and Auger upconversion lead to non-radiative decay in Nd^{3+}[106][107]. Non-radiative decay reduces the gain, increases thermal loading of the gain medium and increases thermal lensing. Gain reduction and increased thermal lensing degrade system performance, while the increased thermal loading increases the probability of fracture of the gain medium.

Cross-relaxation (or self quenching) is the principal energy transfer mechanism at lower pump densities. In this process, part of the energy from an excited ion is transferred to an unexcited ion, and produces two excited ions which decay to the ground state via multiphonon relaxation. Cross-relaxation can be reduced by emptying the ground level, as occurs under intense optical pumping.

At high pump densities, Auger upconversion (or energy transfer upconversion) is dominant[106]. This process involves the interaction of two nearby excited ions: one of the ions decays to a lower state (and eventually to ground state via non-radiative decay) giving it's energy to the other ion which is excited to a higher state. The ion

in the highly excited state subsequently relaxes back to it's original state mostly by multiphonon emission[106][107].

Increasing the doping levels in strongly pumped systems which are affected by Auger upconversion will increase upconversion losses, rather than the gain, and as a consequence increase the thermal loading of the material. Upconversion was demonstrated to be significant in Nd:YAG with high-inversion densities by Guy *et al.*[106]. A similar result was reported by Chuang *et al.*[107] for Nd:YLF.

Excited state absorption (ESA) is another energy loss process observed in some materials. However, a recent series of publications[108][109][110] have shown the effects of ESA to be negligible at the main laser line near 1 μm for YAG, YAP, YVO_4, YLF and CWO. Guyot *et al.*[111] has also reported that ESA at 1.064 μm in Nd:YAG is negligible.

Efficient and compact high power lasers therefore require large $\sigma_{\text{emission}}\tau_f$ products and good pump absorption. However, whether using a host with a large pump absorption or pumping intensely, significant thermal energy per unit volume will be deposited. Parasitic energy loss mechanisms exacerbate this problem. Thus, it is important that the host medium has a large thermal stress resistance parameter.

As shown in Table I, most materials have low thermal conductivities compared to YAG, power-scaling laser materials with poor thermomechanical properties is difficult. Crystal fracture in SGGM[112][113] and KGW [114] using CW pump powers less than 10 W has been reported (both of these materials have low thermal conductivities). It is evident that the only materials suiting the demanding thermomechanical characteristics required for use as CW HPDPSSL host materials are those with thermal conductivities comparable to YAG, which are YLF and YAP. Both materials also have $\sigma_{\text{emission}}\tau_f$ products and absorption coefficients similar to YAG. YLF has an M_s value approximately 70% that of YAG, and a lower thermal conductivity. However σ_f for YLF is only one fifth that of YAG resulting in a low R_s making this material unsuitable for a HPDPSSL.

YAP (or YALO) is the other material with comparable thermal conductivity to YAG (α and E also comparable with YAG). YAP was investigated in the early 70's[115][116][117], and has similar bulk material properties to YAG. In the past it

has been difficult to grow because of a propensity for twinning[118] and therefore high quality material was difficult to obtain. Improved growth techniques have recently produced higher optical quality YAP crystals renewing interest in this material[119]. Thermal lensing in YAP has been observed to be up to 50-60% greater than YAG under identical situations[104][119][120] which, coupled with the slightly lower thermal conductivity and higher thermal expansion coefficient makes YAP less suitable than YAG for a HPDPSSL.

A lack of reported thermomechanical properties at the present time make a quantitative comparison of CWO, NGWO and SGGM with the materials in Table I difficult.

The polarization of the laser beam is another issue often of concern in laser development. Insertion of an intracavity polarizing optic in an unpolarized laser beam can significantly attenuate the output power. This is most significant in rod lasers due to strong thermally induced stress birefringence[121]. Polarized laser beams can be generated by either using a material with inherent polarizing properties or by inserting Brewster-angled surfaces in the laser cavity. Materials with uniaxial or biaxial structures exhibit natural polarization properties, but the crystal orientation must be chosen carefully to ensure appropriate absorption and stimulated emission cross-sections. Significant thermally induced astigmatic focussing is typically found in these materials, necessitating sometimes complicated (and expensive) cylindrical intracavity optics.

Isotropic materials do not exhibit such properties due to the homogeneous nature of the refractive index temperature coefficient, $\mathrm{d}n/\mathrm{d}T$. Polarization can be achieved in isotropic materials by introducing intracavity polarizing elements such as Brewster angle windows to the laser cavity. This is usually achieved for zigzag slab lasers in practice by fabricating the laser slab with entrance or exit faces (or both) oriented so that the intracavity laser mode is incident on the gain medium at Brewster's angle. Alternatively, multiple thin slabs of gain medium can be orientated at Brewster's angle to the intracavity mode[78]. Thus materials without natural polarization properties (like Nd:YAG) are not necessarily a disadvantage but instead allow greater flexibility in terms of pump geometry and avoid astigmatic focussing.

B.4 Conclusion

All materials in Tables I and II with the exception of YLF and YAP have much lower thermal conductivity than YAG. For intensely pumped high power lasers, the combination of high thermal conductivity, isotropic thermal expansion coefficient, high M_s and σ_f values and level of technological development reveal that YAG is currently the most appropriate Nd^{3+} host material for a CW high-power diode-laser-pumped solid-state laser.

B.5 Table Captions

- Table I: Nd^{3+} Material Host Thermomechanical Parameters. Ψ calculated assuming $\nu = 0.33$[25], using k, α and E from Table I. † Errors quoted for a, b and c axes are ± 0.60, ± 0.95 and ± 0.40 respectively[122], subscripts a, b and c refer to crystallographic axes [100], [010] and [001]. Subscripts d, e and f correspond to crystallographic axes [100], [110] and [111] in Nd:YAG. $\diamondsuit$ Data was calculated assuming $\nu = 0.28$. The YVO_4 crystal is tetragonal meaning there are two equivalent 'a' directions and a 'c' direction, all mutually orthogonal. A typical rod axis is oriented along the a axis of the crystal, maximum pump absorption occurs when the pump light polarized along the c axis[123]. BeL is reported in x, y, and z directions denoting mutually orthogonal principle vibration directions. y is aligned with the conventional b crystallographic axis, while z is oriented at 31.7° to the c axis[124]. Here E$\|c$ yields the π polarization and E$\perp$ c is the σ polarization.

- Table II: Nd^{3+} Material Host Spectroscopic Parameters. * The absorption spectrum of Nd:YAP consists of several absorption spikes from 0.78-0.82 μm and has corresponding multiple sharp emission spikes from 1.05 μm to 1.105 μm. The most intense occurs at 1.0795 μm (E$\|b$). Note that the polarization dependent data for Nd:YAP in these Tables was compiled using Pnma space-group notation, some of the references cited use Pbnm notation instead, the difference between co-ordinate systems is given by $(a, b, c)_{\mathrm{Pnma}} \longleftrightarrow (b, c, a)_{\mathrm{Pbnm}}$[118]. Ω Shen *et al.* report a higher value of 6.9 x 10^{-23} cm^2s compared to the number reported here[125]. ‡ The absorption linewidth of Nd:Cr:GSGG incorporates the broad absorption bands of Cr^{3+}, $^4T_1$ and $^4T_2$ centered at 460 and 645 nm, each with a FWHM of ~100 nm[126] [127]. The biaxial structure of Nd:KGW is usually described by three orthogonal axes n_p, n_m, and n_g. n_p (usually aligned to the rod axis) is oriented along the crystallographic b axis, n_m is 24° to the a axis, and n_g makes and angle of 20° to the c axis[104][114].

Nd^{3+}Host Material	Crystal Structure	σ_f (MPa)	M_s (x10^{-6} $Wm^{-1}Pa^{-1}$)	k ($Wm^{-1}K^{-1}$)	dn/dT (x10^{-6} K^{-1})	Therm. Exp. Coeff., α, (x10^{-6} K^{-1})	Elastic Modulus, E, (GPa)
YLF	Uniaxial	54[25]	$6.53_{\parallel c}$ Ψ	6_{π}[128][129]	-4.3_{π}, -2_{σ}[128]	$13_{\parallel a}$, $8_{\parallel c}$[128]	77[25]
YAP (or YALO)	Biaxial	-	3.8_a, 8.4_b 3.6_c $\diamondsuit$	11[120]	10.08_a, 9.12_b, 13.75_c†[122]	$9.5_{\parallel a}$, $4.3_{\parallel b}$, $10.1_{\parallel c}$[104]	220[120]
Glass	Isotropic	166[25]	1.39[25]	1.26[130]	3.8[130]	7.7[130]	94[130]
YAG	Isotropic	280[25]	3.74	10.39[131], 14[123]	8.9[132]	8.2_d, 7.7_e, 7.8_f[133]	282 [25]
YVO_4	Uniaxial	-	-	5.1_a, 5.23_c[134]	8.5_a, 3.9_c[134]	3.1_a, 7.2_c[134]	-
GSGG:Cr	Isotropic	240[25]	2.74[25]	6[25]	10.1[25]	7.5[25]	212[83]
KGW	Biaxial	137_a, 100_b, 63_c[135]	4.0_a, 5.0_b $3.1_c\diamondsuit$	2.6_a, 3.8_b, 3.4_c[114] [135]	0.4 [103][129][132]	$4_{\parallel a}$, $3.6_{\parallel b}$, $8.5_{\parallel c}$[104]	115.8_a, 152.5_b, 92.4_c[135]
BeL	Biaxial	98[124]	2.24[124]	4.6_a, 4.7_b, 4.7_c[136]	$2.86_{\parallel x}$, $1.53_{\parallel y}$, $-6.23_{\parallel z}$[124]	7.0_a, 7.9_b, 9.5_c[136]	-
S-VAP	Uniaxial	-	-	1.7[137]	-8, -11[137]	-	-
CWO	Uniaxial	-	-	4[138][139]	-	11.2_a, 18.7_b[139]	-
NGWO	Uniaxial	-	-	-	-	-	-
SGGM	Uniaxial	-	-	-	-	-	-

Table I

Nd^{3+} Host Material	Formula	$\lambda_{absorption}$ (μm)	Abs. Linewidth (nm)	Nd^{3+} Doping (typ.) Concentration	Abs. Coeff. (cm^{-1})	$\sigma_{emission}\tau_f$ (x10^{-23} cm^2s)	$\lambda_{emission}$ (μm)
YLF	$YLiF_4$	0.793_{π}[129], 0.806_{σ}[142]	2.42_{π}[140]	1.1 at.%[140]	7.2_{π}[140]	10.2_{π}, 7.41_{σ}[141]	1.047_{π}, 1.053_{σ}[129]
YAP (or YALO)	$YAlO_3$	$0.813^{*}_{\parallel b}$[104][118]	$2\text{-}4^{*}_{\parallel b}$[104][118]	1.0(max 1.8) at.% [104][118]	$11.5^{*}_{\parallel b}$[104][118]	$5.25^{*\Omega}_{\parallel b}$[118]	1.0645, 1.0725, 1.0795*[83]
Glass	ED-2 Silicate	0.810[143]	26-30[143]	3.1 wt.%[143]	-	0.909[143]	1.0623[143]
YAG	$Y_3Al_5O_{12}$	0.808[129]	1.2[138]	1.1(max 1.25) at.%[104]	9[104]	6.4[83]	1.064[144]
YVO_4	YVO_4	0.809_{π}[145]	1.4_{π}[138]	1.1(max 3.0) at.%[140]	31_{π}[140]	17.9_{π}[101]	1.064_{π}[123]
GSGG:Cr	$Gd_3Sc_2Ga_3O_{12}$:Cr	‡	‡	1.0(Cr:1.0) at.%	‡	3.61[25]	‡
KGW	$KGd(WO_4)_2$	$0.810_{\parallel n_m}$[104]	$2_{\parallel n_m}$[104][132]	3.0(max 10.0) at.%[104]	$8_{\parallel n_m}$[104]	$4.08_{\parallel n_m}$[104]	$1.067_{\parallel n_m}$[104][129]
BeL	$La_2Be_2O_5$	$0.811_{x,y}$[144]	-	1.0 wt.% [146]	-	2.02_x, 3.12_y[146]	1.0792_x, 1.0701_y[146]
S-VAP	$Sr_5(VO_4)_3F$	0.8095_{π}[137]	1.6_{π}[137][140]	0.38 at.%[140]	16.9_{π}[140]	11.5_{π}[137]	1.065_{π}[125]
CWO	$CaWO_4$	0.8033_{π}[138]	2.6_{π}[138]	1.0(max 2.0) at.%[138]	4.9_{π}[138]	3.24_{π}[138]	1.0578_{π}[138]
NGWO	$NaGd(WO_4)_2$	0.8032_{π}[138]	2.9_{π}[138]	1.0 at.%[138]	5.5_{π}[138]	1.86_{π}[138]	1.058_{π}[138]
SGGM	$SrGdGa_3O_7$	$0.808_{\perp c}$[112][123]	$8_{\perp c}$[112][132]	4.0 at.%[123]	$13_{\perp c}$[123]	$1.62_{\perp c}$[132]	$1.065_{\perp c}$[123]

Table II

Appendix C

Laser Crystal Schematic Diagrams

The schematic diagrams in this Appendix describe the Nd:YAG laser crystal used for the experiments in this thesis. The crystal dimensions were calculated and toleranced (and subsequently drawn) by the author.

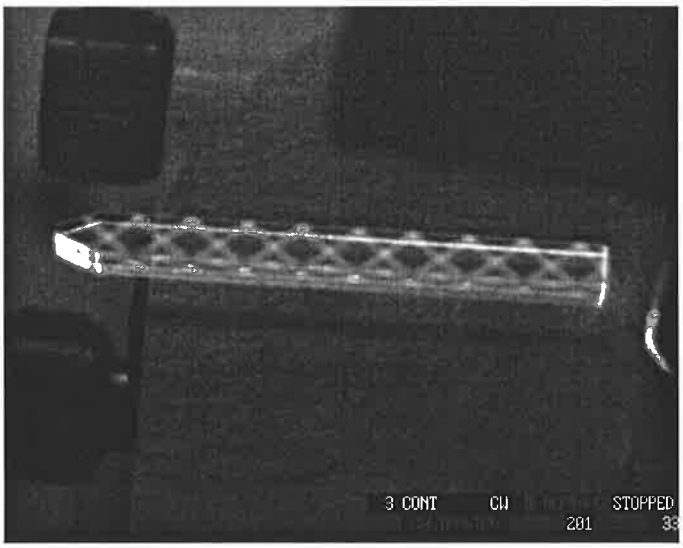

Photograph of an infrared beam ($\lambda = 1.064$ μm) passing through the 19 TIR-bounce long Nd:YAG zigzag slab described by the following schematic diagrams.

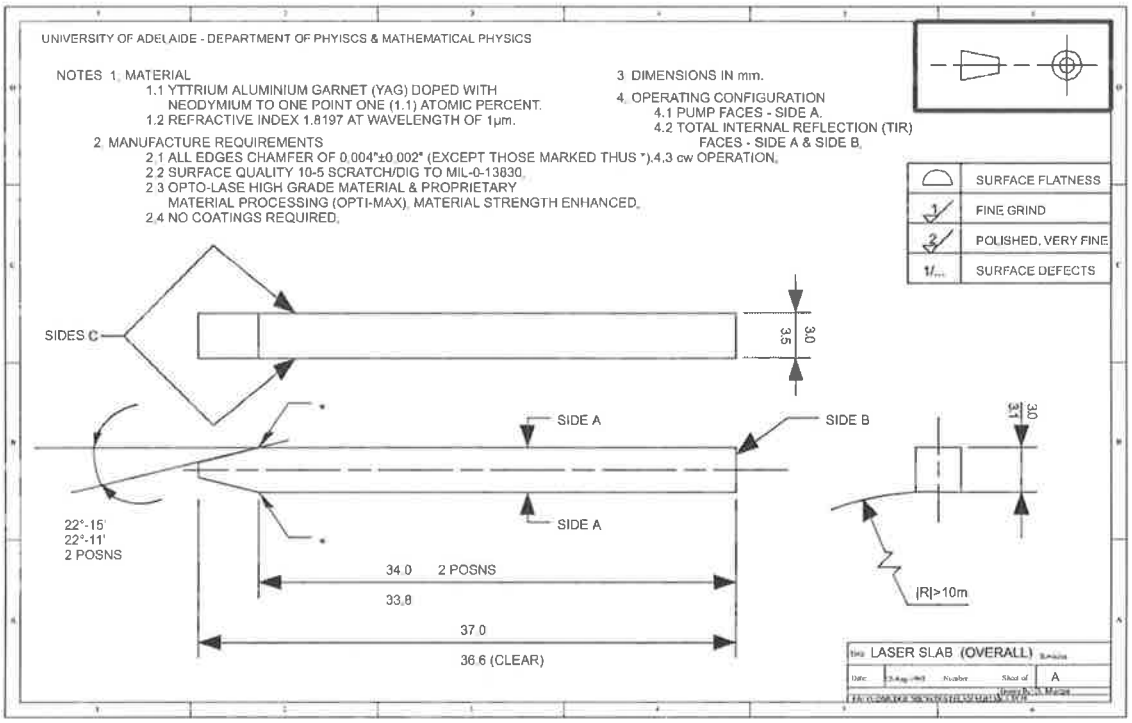
UNIVERSITY OF ADELAIDE - DEPARTMENT OF PHYISCS & MATHEMATICAL PHYSICS
NOTES 1. MATERIAL
1.1 YTTRIUM ALUMINIUM GARNET (YAG) DOPED WITH NEODYMIUM TO ONE POINT ONE (1.1) ATOMIC PERCENT.
1.2 REFRACTIVE INDEX 1.8197 AT WAVELENGTH OF 1μm.
2. MANUFACTURE REQUIREMENTS
2.1 ALL EDGES CHAMFER OF 0.004"±0.002" (EXCEPT THOSE MARKED THUS *).4.3 cw OPERATION.
2.2 SURFACE QUALITY 10-5 SCRATCH/DIG TO MIL-0-13830.
2.3 OPTO-LASE HIGH GRADE MATERIAL & PROPRIETARY MATERIAL PROCESSING (OPTI-MAX). MATERIAL STRENGTH ENHANCED.
2.4 NO COATINGS REQUIRED.
3. DIMENSIONS IN mm.
4. OPERATING CONFIGURATION
4.1 PUMP FACES - SIDE A.
4.2 TOTAL INTERNAL REFLECTION (TIR) FACES - SIDE A & SIDE B.
SURFACE FLATNESS
FINE GRIND
POLISHED, VERY FINE
SURFACE DEFECTS
SIDES C
3.5
3.0
SIDE A
SIDE B
SIDE A
22°-15'
22°-11'
2 POSNS
34.0 2 POSNS
33.8
37.0
36.6 (CLEAR)
3.1
3.0
|R|>10m
LASER SLAB (OVERALL)

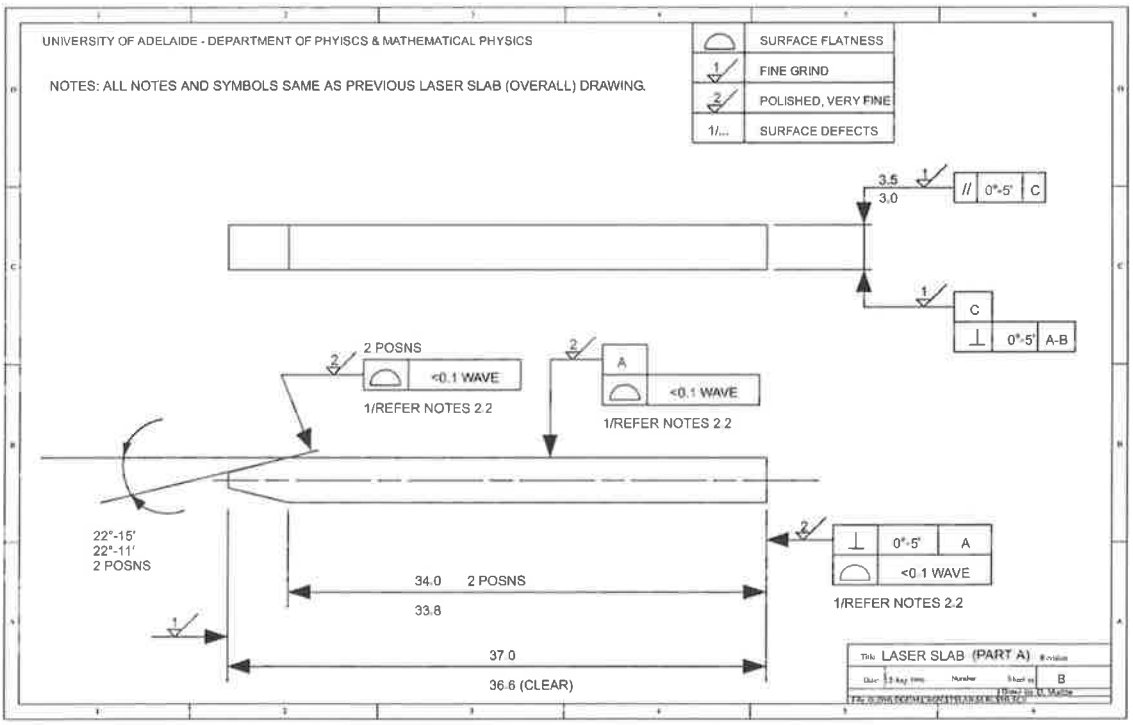
UNIVERSITY OF ADELAIDE - DEPARTMENT OF PHYISCS & MATHEMATICAL PHYSICS
NOTES: ALL NOTES AND SYMBOLS SAME AS PREVIOUS LASER SLAB (OVERALL) DRAWING.
SURFACE FLATNESS
FINE GRIND
POLISHED, VERY FINE
SURFACE DEFECTS
3.5
3.0
// 0°-5' C
C
⊥ 0°-5' A-B
2 POSNS
<0.1 WAVE
1/REFER NOTES 2.2
A
<0.1 WAVE
1/REFER NOTES 2.2
22°-15'
22°-11'
2 POSNS
34.0 2 POSNS
33.8
37.0
36.6 (CLEAR)
⊥ 0°-5' A
<0.1 WAVE
1/REFER NOTES 2.2
LASER SLAB (PART A)

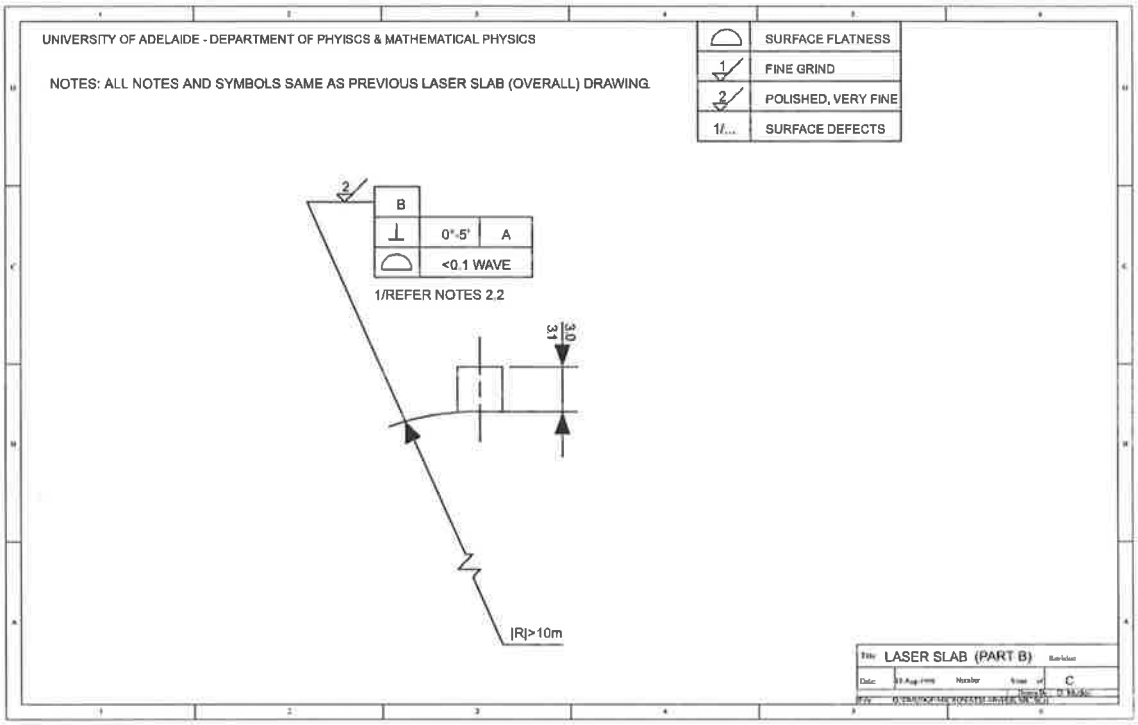
UNIVERSITY OF ADELAIDE - DEPARTMENT OF PHYISCS & MATHEMATICAL PHYSICS
NOTES: ALL NOTES AND SYMBOLS SAME AS PREVIOUS LASER SLAB (OVERALL) DRAWING.
SURFACE FLATNESS
FINE GRIND
POLISHED, VERY FINE
SURFACE DEFECTS
B
0°-5'
A
<0.1 WAVE
1/REFER NOTES 2.2
3.0
3.1
|R|>10m
LASER SLAB (PART B)
C

Appendix D

Diode-Laser Cooling Setup & Drive Circuits

The wavelength of a diode-laser is temperature dependent (1 nm per 2.7-3°C). For optimum performance these devices require temperature stability as well as cooling. One method of achieving this requires a feedback circuit. This Appendix includes a diagram of the diode-laser cooling arrangement (see Figure D.1) and the feedback control circuit used to temperature stabilize the diode-lasers used for the work in this thesis. The cooling arrangement in Figure D.1 uses a TEC (Melcor, model # CP 2-127-06L) with dimensions 62 mm × 62 mm × 4.6 mm high. The lower copper heatsink is water cooled to a temperature of 15°C. The diode-laser is mounted on the upper copper block; good thermal contact was ensured with a layer of Indium foil. The TEC is placed between the copper blocks (using thermal grease) and acts as a heat valve, moving heat from the diode-laser ($T_C \approx 25°C$) to the heatsink ($T_H \approx 15°C$)[1]. The copper block contained a thermistor to monitor the diode-laser temperature and provide feedback to the control circuit.

The control circuit is an adaption of the circuitry published by Bradley *et al.*[147]. The circuit was modified to include a power op-amp rather than transistors as used by the original authors due to large currents required to drive the TEC's. The response of the proportional, integration and differentiation stage was optimized to

[1] T_C and T_H is a common notation used to denote the temperatures of the 'cold' and 'hot' sides of the TEC respectively, typical applications yield an increasing temperature gradient across the TEC from the 'cold' to 'hot' sides. In this application the 'cold' side is warmer than the 'hot' side.

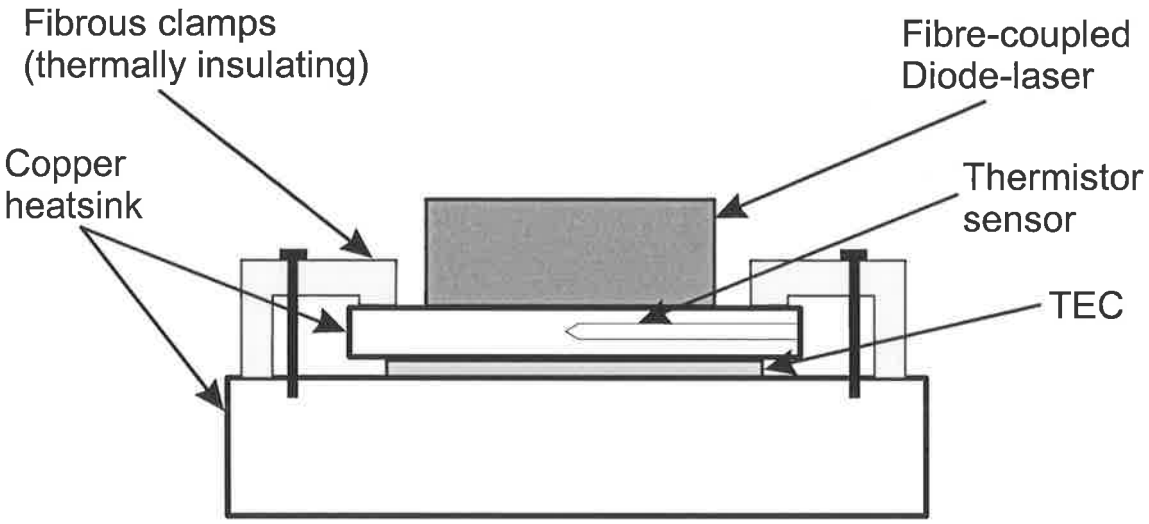

Figure D.1: Cooling arrangement for the diode-laser.

suit the cooling system here. Using this circuitry, the temperature of the diode-lasers was maintained to an accuracy of better than $\pm$ 0.1°C at maximum heat load, as required by the laser system. Note that $\pm$ 0.1°C is equivalent to 3.3 x 10^{-3} nm.

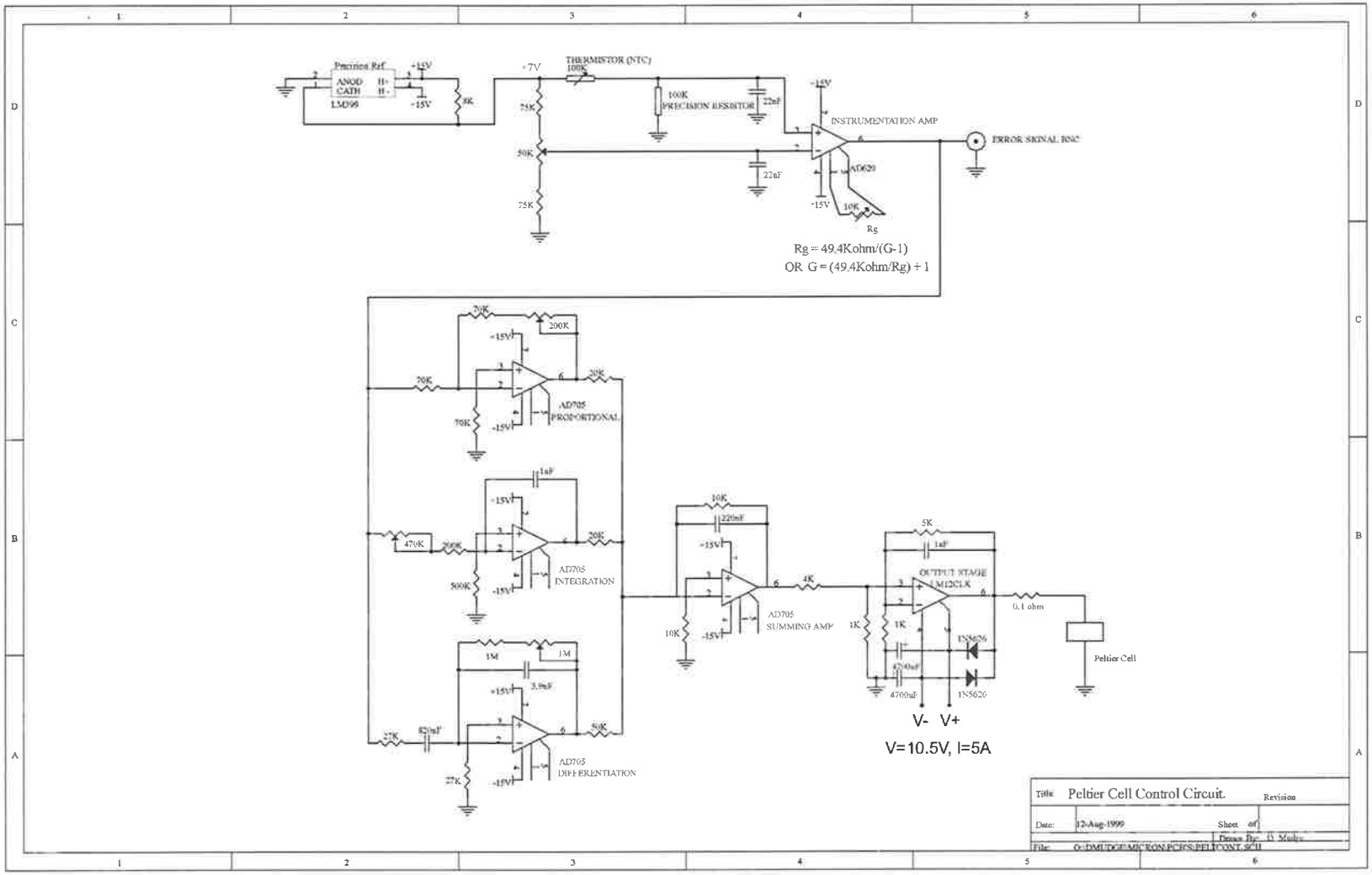
Precision Ref.
ANOD
CATH
LM399
+15V
-15V
8K
+7V
THERMISTOR (NTC)
100K
75K
50K
75K
100K
PRECISION RESISTOR
22nF
22nF
INSTRUMENTATION AMP
AD620
10K
Rg
ERROR SIGNAL BNC
Rg = 49.4Kohm/(G-1)
OR G = (49.4Kohm/Rg) + 1
20K
200K
20K
20K
70K
AD705
PROPORTIONAL
1uF
470K
200K
20K
500K
AD705
INTEGRATION
1M
1M
3.9nF
27K
820nF
50K
27K
AD705
DIFFERENTIATION
10K
220nF
10K
AD705
SUMMING AMP
4K
5K
1uF
OUTPUT STAGE
LM12CLK
1K
1K
0.1 ohm
1N5626
4700uF
4700uF
1N5626
Peltier Cell
V- V+
V=10.5V, I=5A
Title: Peltier Cell Control Circuit.
Revision
Date: 12-Aug-1999
Sheet of
Drawn By: D. Mullis
File: G:\DMU\DGE\MICRON\PCFS\PELTCONT.SCH

Appendix E

Small-Signal Gain & Crystal Loss

E.1 Small-signal gain

The small-signal gain, g_o, for a four-level laser may be approximated by [83]

$$g_o \approx \sigma_{21} W_p n_o \tau_f \tag{E.1}$$

where σ_{21} is the stimulated emission cross-section, W_p is the pumping rate, n_o is the number of atoms in the ground state per unit volume and τ_f is the fluorescence lifetime. $W_p n_o$ is number of atoms excited from the ground to upper laser level per unit volume and time, which can alternatively be written as $(\eta_{tot} P'/h\nu_l V)$. η_{tot} is the product of the quantum efficiency (η_q) and the Stokes factor (η_s), and $h\nu_l$ is the energy per laser photon. P' is given by $\eta_B P_p$, η_B is the beam overlap efficiency, and P_p is the pump-power deposited in volume V. Multimode lasers typically have a value of η_B of 0.8-0.9[83]. Therefore,

$$g_o \approx \frac{\sigma_{21} \tau_f \eta_{tot} \eta_B P_p}{h\nu_l V} \tag{E.2}$$

For a slab geometry V has dimensions $w_p \times h_p \times l_p$ (whereas for a rod V has dimensions $\pi r_p^2 \times l_p$, using the same notation as previously with the subscript p denoting a pumped dimension). For a TIR zigzag path in a slab, similar to Figure 4.4, not all of the pathlength within the slab overlaps the pumped region. The total pathlength in the gain region, l_g, can be expressed in terms of the pumped length,

l_p, and the TIR angle, θ_1.

$$l_g = \frac{2l_p}{\sin(\theta_1)} \tag{E.3}$$

For a standing-wave resonator the output power is given by[148]

$$P_{out,\text{standing-wave}} = A_m I_s \frac{(1-\overline{R})}{1-\overline{R}+\sqrt{\overline{R}}(\frac{1}{Y}-Y)} \left[g_o l_g - \left|\ln\sqrt{Y^2\overline{R}}\right|\right] \tag{E.4}$$

For a travelling-wave (or ring) resonator the output power can be expressed as[148][149]

$$P_{out,\text{travelling-wave}} = A_m I_s \frac{(1-\overline{R})}{1-Y\overline{R}} \left[g_o l_g - \left|\ln(Y\overline{R})\right|\right] \tag{E.5}$$

assuming no loss at intracavity apertures. A_m is the cross-sectional area of the mode, I_s is the saturation intensity, Y is the net loss factor within the resonator and $\overline{R}$ is the reflectance of the output coupler.

E.2 Crystal Loss

In this section the loss mechanisms relevant to TIR slab lasers is investigated. High intracavity loss decreases efficiency and increases the threshold of a laser. Therefore, high quality (low loss) crystals are sought for all high power solid-state laser applications. Crystal loss is due to two mechanisms: bulk scatter from crystal imperfections, thermal aberrations and material impurities; and scatter due to micro-roughness of the sides (only important for TIR lasers).

$$loss_{\text{bulk scatter}} = 1 - \exp[-\alpha_o l] \tag{E.6}$$

$$loss_{\text{TIR scatter}} = 1 - [1 - loss_{\text{per TIR}}]^{nb} \tag{E.7}$$

where nb is the number of TIR-bounces, α_o is the bulk scatter coefficient, l is the total pathlength in the crystal and $loss_{\text{per TIR}}$ is the loss per TIR bounce. Low loss TIR zigzag crystals, like those required for this work, are highly dependent on side polish quality. Quantitative details of loss mechanisms enable calculation of intracavity loss, and therefore the impact on expected laser performance. The other loss term to be included is the loss at external mirrors or apertures ($loss_{\text{ext.}}$) with a typical value of 1% for example. Note that this does not include the loss at the output coupler (which is $(1 - \overline{R})$).

The loss factor is then given by Y

$$Y = 1 - loss_{\text{bulk scatter}} - loss_{\text{TIR scatter}} - loss_{\text{ext.}}$$

Hence,

$$Y = \exp[-\alpha_o l] + [1 - loss_{\text{per TIR}}]^{nb} - loss_{\text{ext.}} - 1 \tag{E.8}$$

Appendix F

Alignment Laser

During the work in this thesis, a low power Nd:YAG laser was required for alignment and testing of 1.064 μm optics; including measurement of GRM reflectivity profiles, single-pass gain measurements and single-pass crystal loss measurements at 1.064 μm. It was also used for adjustment of the arrays of pump fibres so the pump field and the zigzag mode were co-planar, as this can be achieved by maximizing the single-pass gain.

A stable TIR zigzag slab laser was chosen for this purpose, the crystal is the same as that used by Richards and McInnes[23]. A short standing-wave resonator was constructed using a flat max-R mirror and a flat 90% reflectance output coupler. Both mirrors are 4 cm from the end of the slab. The laser used a stable resonator due to the positive horizontal and vertical thermal lensing. The focal length of the horizontal thermal lens was very weak due to the zigzag and careful alignment was required in the horizontal direction. The vertical direction provided a somewhat stronger thermal lens focal length, as this was the direction of slab cooling.

Figure F.1 shows an end-view of the low power Nd:YAG TIR zigzag slab laser. The slab is side-pumped by a nominally 5 W diode-laser (SDL-3480-S). The fast axis ($x-$direction) of the diode-laser pump field is collimated by a 0.75 mm glass fibre (no AR coating), which acted as a cylindrical lens for the pump radiation. The length of the optical fibre was slightly longer than the pumped length of the slab ($z-$axis). Alignment of the optical fibre requires adjustment of height ($x-$direction), distance from the diode-laser ($y-$direction), two tilt directions (about $x-$ and $y-$axes) to

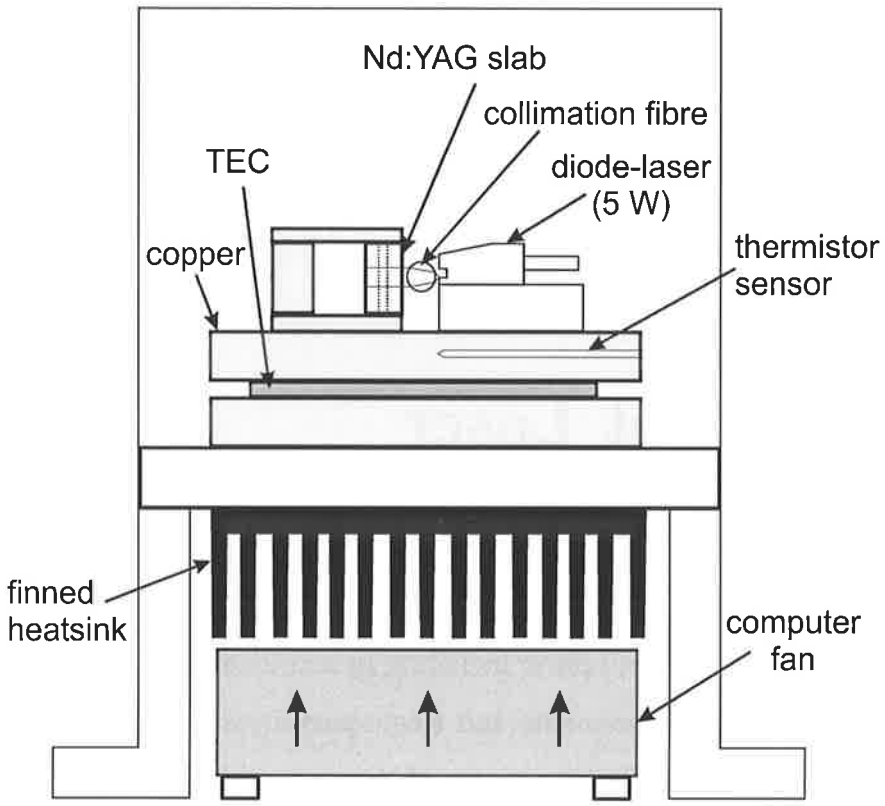

Figure F.1: End view of the low power Nd:YAG TIR zigzag slab laser and the cooling system.

allow the collimation fibre to be adjusted so that it is parallel to the active region of the diode-laser. Using the maximum diode-laser current that could be supplied by the diode-driver, the pump power after the collimating fibre is 4 W.

The diode-laser and the Nd:YAG slab are mounted on a common copper plate. Heat is removed from the copper plate using a TEC (Marlow Industries, model # DT12-6). A thermistor is positioned in the copper plate to provide input to the circuitry which controlled the TEC, using a circuit that is similar to the one described in App. D. The TEC and feedback system allowed the temperature of the diode-laser and slab to be accurately set, while simultaneously cooled. The waste heat from the hot side of the TEC is removed by forced-air convection from the heatsink. Plate # 8 shows a photograph of the top view of the laser, showing the diode-laser, slab and the locations of the resonator mirrors. The laser was enclosed by a metal cover to contain any stray pump light.

The laser produced up to 540 mW, from 4 W of pump power. This is more power

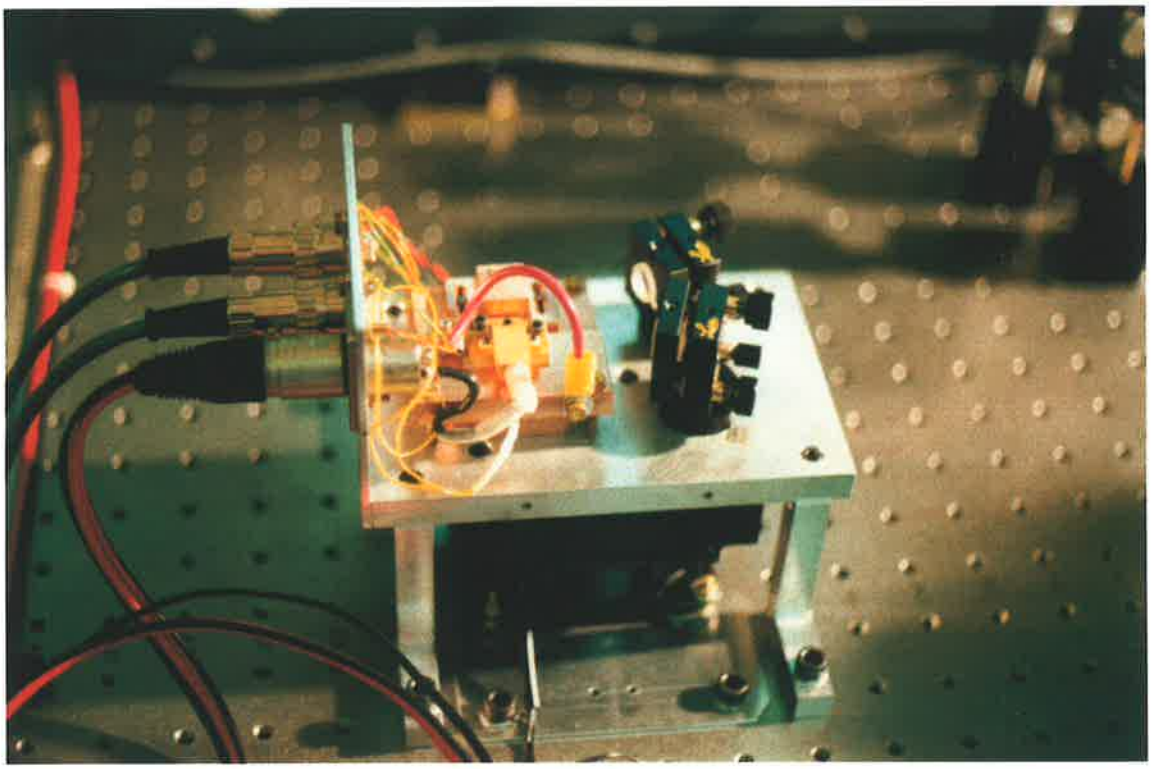

Plate # 8

Nd:YAG alignment laser.

than required for the applications here so no attempt was made to change the output coupler to investigate the efficiency, a 95% output coupler would probably be more appropriate. The measured M^2 was better than 1.02 in both x- and y-directions[1], for 300 mW of output power.

[1] M^2 measured using an M^2-101 Laser Beam Propagation Analyzer, and LBA-100A Laser Beam Analyzer from Spiricon, Inc., Logan, UT, U.S.A.

Appendix G

Publications

G.1 Publications resulting from this work

- D. Mudge, P.J. Veitch, J. Munch, D. Ottaway, and M.W. Hamilton, "High-Power Diode-Laser-Pumped CW Solid-State Lasers Using Stable-Unstable Resonators," *IEEE J. Selected Topics in Quantum Electron.*, vol. 3, no. 1, pp. 19-25, Feb. 1997.

- D. Mudge, M. Ostermeyer, P.J. Veitch, J. Munch, B. Middlemiss, D.J. Ottaway, and M.W. Hamilton, "Power Scalable TEM_{oo} CW Nd:YAG Laser with Thermal Lens Compensation," *IEEE J. Selected Topics in Quantum Electron.*, vol. 6, no. 4, pp. 643-649, Jul./Aug. 2000.

Mudge, D., Veitch, P.J., Munch, J., Ottaway, D., and Hamilton, M.W., (1997) High-power diode-laser-pumped CW solid-state lasers using stable-unstable resonators. *IEEE Journal of Selected Topics in Quantum Electronics, v. 3 (1), pp. 19-25.*

Mudge, D., Ostermeyer, M., Veitch, P.J., Munch, J., Middlemiss, B., Ottaway, D.J., and Hamilton, W.M., (2000) Power scalable TEM/sub 00/ CW Nd:YAG laser with thermal lens compensation.
IEEE Journal of Selected Topics in Quantum Electronics, v. 6 (4), pp. 643-649.

G.2 Other publications associated with this work

- D.J. Ottaway, P.J. Veitch, M.W. Hamilton, C. Hollitt, D. Mudge, and J. Munch, "A Compact Injection-Locked Nd:YAG Laser for Gravitational Wave Detection" *IEEE J. Quantum Electron.*, vol. 34, no. 10, pp. 2006-2009, Oct. 1998.

- D.J. Ottaway, P.J. Veitch, C. Hollitt, D. Mudge, M.W. Hamilton, and J. Munch, "Frequency and Intensity Noise of an Injection-Locked Nd:YAG Ring Laser," *Appl. Phys. B,* vol. B71, no. 2, pp. 163-168, Aug. 2000.

Appendix H

GRM Specification Sheet

Included in this Appendix is a copy of the GRM specification sheet submitted to the National Optics Institute[1] (INO), showing the specifications and tolerances of the GRM used for the experiments in Chapter 7 of this thesis.

[1]National Optics Institute, 369, rue Franquet, Sainte-Foy, (Québec) Canada G1P 4N8. Tel. (418) 657-7006, Fax. (418) 657-7009.

INSTITUT NATIONAL D'OPTIQUE | NATIONAL OPTICS INSTITUTE
369, rue Franquet, Sainte-Foy, (Québec) Canada G1P 4N8 - Tél. (418) 657-7006 Fax (418) 657-7009

GRADED REFLECTIVITY MIRROR™ SPECIFICATIONS

REF. NO: DATE: 19/01/00

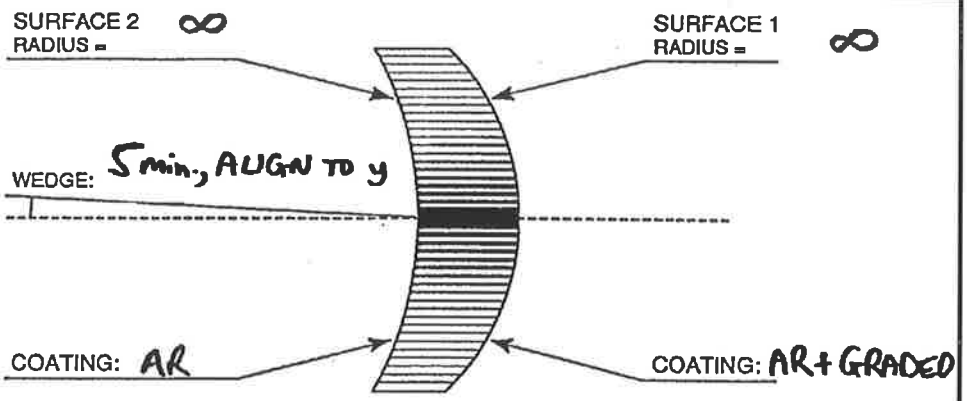

SUBSTRATE

DIAMETER: 0.5"
THICKNESS: 0.375"
MATERIAL: FUSED SILICA
QUANTITY: 1

COATING

GRM REFLECTIVITY PROFILE

$$R(x,y) = R_o * Exp\left[-\left(\frac{x}{\omega_x}\right)^{n_x}\right] * Exp\left[-\left(\frac{y}{\omega_y}\right)^{n_y}\right] + R_s$$

R_o - 77 ± 3 % $R_s \leq$ 1.5 %
ω_x = 3 ± 0.5 mm ω_y = 0.7 ± 0.1 mm
n_x - 20 ± 5 n_y - 5 ± 3

WAVELENGTH OF UTILISATION: 1.064 µm
ENERGY/POWER REGIME: D.T. < 500 MW/cm² CW
(Specify J/cm² and τ_p for pulsed operation) BEST EFFORT

NAME UNIV. OF ADELAIDE : GRM
JOB TITLE DIVISION/DEPT PHYSICS
COMPANY UNIVERSITY OF ADELAIDE
ADDRESS *SEE ORDER FORM (UNIV. OF ADEL.)
CITY FOR DELIVERY INFORMATION & ADDRESS.*
ZIP/POSTAL CODE COUNTRY
TELEPHONE NO. +61 8 8303 3552 FAX NO. +61 8 8232 6541

Figure H.1: GRM specification sheet.

Bibliography

[1] D. Mudge, P. J. Veitch, J. Munch, D. Ottaway, and M. W. Hamilton, "High-Power Diode-Laser-Pumped CW Solid-State Lasers Using Stable-Unstable Resonators," *IEEE J. Selected Topics in Quantum Electron.*, vol. 3, pp. 19–25, Feb. 1997.

[2] D. Mudge, M. Ostermeyer, P. Veitch, J. Munch, B. Middlemiss, D. Ottaway, and M. Hamilton, "Power Scalable TEMoo CW Nd:YAG Laser with Thermal Lens Compensation," *IEEE J. Selected Topics in Quantum Electron.*, vol. 6, pp. 643–649, Jul./Aug. 2000.

[3] W. Streifer, D. R. Scifres, G. L. Harnagel, D. F. Welch, J. Berger, and M. Sakamoto, "Advances in Diode Laser Pumps," *IEEE J. Quantum Electron.*, vol. QE-24, pp. 883–893, Jun. 1988.

[4] J. G. Endriz, M. Vakili, G. S. Browder, M. DeVito, J. M. Haden, G. L. Harnagel, W. E. Plano, M. Sakamoto, D. F. Welch, S. Willing, D. P. Worland, and H. C. Yao, "High Power Diode Laser Arrays," *IEEE J. Quantum Electron.*, vol. QE-28, pp. 952–965, Apr. 1992.

[5] T. Y. Fan and R. L. Byer, "Diode Laser-Pumped Solid-State Lasers," *IEEE J. Quantum Electron.*, vol. QE-24, pp. 895–912, Jun. 1988.

[6] A. D. Farinas, E. K. Gustafson, and R. L. Byer, "Design and characterization of a 5.5-W, cw, injection-locked, fibre-coupled, laser-diode-pumped Nd:YAG miniature-slab laser," *Opt. Lett.*, vol. 19, pp. 114–116, Jan. 1994.

[7] I. Freitag, D. Golla, S. Knoke, W. Schöne, A. Tünnermann, and H. Welling, "Amplitude and frequency stability of a diode-pumped Nd:YAG laser oper-

ating at a single-frequency continous-wave output power of 20W," *Opt. Lett.*, vol. 20, pp. 462–464, Mar. 1995.

[8] S. T. Yang, Y. Imai, M. Oka, N. Eguchi, and S. Kubota, "Frequency-stabilized, 10-W continuous-wave, laser-diode end-pumped, injection-locked Nd:YAG laser," *Opt. Lett.*, vol. 21, pp. 1676–1678, Oct. 1996.

[9] K. Contag, S. Erhard, M. Karszewski, M. Larionov, D. Muller, C. Stewen, A. Giesen, and I. Johannsen, "Power scalability and beam quality of the thin disk laser," No. CTuE3, pp. 198–199, CLEO Proc., OSA Technical digest (Optical Society of America, Washington DC), May 2000.

[10] S. C. Tidwell, J. F. Seamans, and M. S. Bowers, "Highly efficient 60-W TEM_{oo} cw diode-end-pumped Nd:YAG laser," *Opt. Lett.*, vol. 18, pp. 116–118, Jan. 1993.

[11] S. C. Tidwell, J. F. Seamans, M. S. Bowers, and A. K. Cousins, "Scaling CW Diode-End-Pumped Nd:YAG Lasers to High Average Powers," *IEEE J. Quantum Electron.*, vol. QE-28, pp. 997–1009, Apr. 1992.

[12] B. Neuenschwander, R. Weber, and H. P. Weber, "Thermal Lens and Beam Properties in Multiple Longitudinally Diode Laser Pumped Nd:YAG Slab Lasers," *IEEE J. Quantum Electron.*, vol. QE-32, pp. 365–369, Mar. 1996.

[13] D. Golla, M. Bode, S. Knoke, W. Schöne, and A. Tünnermann, "62-W cw TEM_{oo} Nd:YAG laser side-pumped by fiber-coupled diode lasers," *Opt. Lett.*, vol. 21, pp. 210–212, Feb. 1996.

[14] J. M. Eggleston, T. J. Kane, K. Kuhn, J. Unternahrer, and R. L. Byer, "The Slab Geometry Laser - Part I: Theory," *IEEE J. Quantum Electron.*, vol. QE-20, pp. 289–301, Mar. 1984.

[15] T. J. Kane, R. C. Eckardt, and R. L. Byer, "Reduced Thermal Focusing and Birefringence in Zig-Zag Slab Geometry Crystalline Lasers," *IEEE J. Quantum Electron.*, vol. QE-19, pp. 1351–1354, Sep. 1983.

[16] R. J. Shine, A. J. Alfrey, and R. L. Byer, "40-W cw, TEM_{oo}-mode, diode-laser-pumped, Nd:YAG miniature-slab laser," *Opt. Lett.*, vol. 20, pp. 459–461, Mar. 1995.

[17] G. F. Albrecht, J. M. Eggleston, and R. A. Petr, "Progress on Slab Lasers," *SPIE*, vol. 622, pp. 18–29, 1986.

[18] N. Hodgson and T. Haase, "Beam parameters, mode structure and diffraction losses of slab lasers with unstable resonators," *Opt. and Quantum Electron.*, vol. 24, pp. S903–S926, Sep. 1992.

[19] Q. Lü, S. Dong, and H. Weber, "A compact resonator design for high power slab lasers," *Opt. Commun.*, vol. 99, pp. 201–206, Jun. 1993.

[20] N. Hodgson, S. Dong, and Q. Lü, "Performance of a 2.3-kW Nd:YAG slab laser system," *Opt. Lett.*, vol. 18, pp. 1727–1729, Oct. 1993.

[21] R. J. StPierre, D. W. Mordaunt, H. Injeyan, J. G. Berg, R. C. Hilyard, M. E. Weber, M. G. Wickham, G. M. Harpole, and R. Senn, "Diode Array Pumped Kilowatt Laser," *IEEE J. Selected Topics in Quantum Electron.*, vol. 3, pp. 53–58, Feb. 1997.

[22] R. J. StPierre, G. W. Holleman, M. Valley, H. Injeyan, J. G. Berg, G. M. Harpole, R. C. Hilyard, M. Mitchell, M. E. Weber, J. Zamel, T. Engler, D. Hall, R. Tinti, and J. Machan, "Active Tracker Laser (ATLAS)," *IEEE J. Selected Topics in Quantum Electron.*, vol. 3, pp. 64–70, Feb. 1997.

[23] J. Richards and A. McInnes, "Versatile, efficient, diode-pumped miniature slab laser," *Opt. Lett.*, vol. 20, pp. 371–373, Feb. 1995.

[24] A. E. Siegman, "Unstable optical resonators for laser applications," *Proc. IEEE*, vol. 53, pp. 277–287, Mar. 1965.

[25] W. F. Krupke, M. D. Shinn, J. E. Marion, J. A. Caird, and S. E. Stokowski, "Sprectroscopic, optical, and thermomechanical properties of neodymium- and chromium-doped gadolinium scandium gallium garnet," *J. Opt. Soc. Am. B*, vol. 3, pp. 102–114, Jan. 1986.

[26] R. A. Chodzko, H. Mirels, F. S. Roehrs, and R. J. Pedersen, "Application of a Single Frequency Unstable Cavity to a CW HF Laser," *IEEE J. Quantum Electron.*, vol. QE-9, pp. 523–530, May 1973.

[27] D. Ehrlichmann, U. Habich, H. D. Plum, P. Loosen, and G. Herziger, "Azimuthally Unstable Resonators for High-Power CO_2 Lasers with Annular Gain Media," *IEEE J. Quantum Electron.*, vol. QE-30, pp. 1441–1447, Jun. 1994.

[28] A. Lapucci, A. Labate, F. Rossetti, and S. Mascalchi, "Hybrid stable-unstable resonators for diffusion-cooled CO_2 lasers," *Appl. Opt.*, vol. 35, pp. 3185–3192, Jun. 1996.

[29] M. K. Reed and R. L. Byer, "The output beam quality of a Q-switched Nd:Glass slab laser," *IEEE J. Quantum Electron.*, vol. QE-26, pp. 2138–2145, Dec. 1990.

[30] K. Kuba, T. Yamamoto, and S. Yagi, "Improvement of slab-laser beam divergence by using an off-axis unstable-stable resonator," *Opt. Lett.*, vol. 15, pp. 121–123, Jan. 1990.

[31] K. Yasui, S. Yagi, and M. Tanaka, "Negative-branch unstable resonator with a phase unifying output coupler for high power Nd:YAG lasers," *Appl. Opt.*, vol. 29, pp. 1277–1280, Mar. 1990.

[32] N. Hodgson and G. Bostanjoglo, "The near-concentric unstable resonator (NCUR) - an improved resonator design for high power solid state lasers," *Opt. Commun.*, vol. 99, pp. 75–81, May 1993.

[33] K. Yasui and J. Nishimae, "Beam-mode calculations for a strongly pumped solid-state rod laser with an unstable resonator," *Opt. Lett.*, vol. 19, pp. 560–562, Apr. 1994.

[34] N. Hodgson and H. Weber, "High-power solid-state lasers with unstable resonators," *Opt. and Quantum Electron.*, vol. 22, pp. S39–S55, Jul. 1990.

[35] N. Pavel, T. Dascalu, and V. Lupei, "Positive-branch unstable resonators with thermal lens compensation," *Opt. and Laser Technol.*, vol. 28, pp. 451–455, Sep. 1996.

[36] A. E. Siegman, "Excess spontaneous emission in non-Hermitian optical systems. I. Laser amplifiers," *Phys. Rev. A*, vol. 39, pp. 1253–1263, Feb. 1989.

[37] C. J. Buczek, R. J. Freiberg, and M. L. Skolnick, "Laser Injection Locking," *Proc. of the IEEE*, vol. 61, pp. 1411–1431, Oct. 1973.

[38] A. E. Siegman, "Lasers without photons - or should it be lasers with too many photons?," *Appl. Phys. B*, vol. 60, pp. 247–257, 1995.

[39] J. Doumont, P. L. Mussche, and A. E. Siegman, "Excess Spontaneous Emission in Variable Reflectivity-Mirror Lasers," *IEEE J. Quantum Electron.*, vol. 25, pp. 1960–1967, Aug. 1989.

[40] K. Du, N. Wu, J. Xu, J. Giesekus, P. Loosen, and R. Poprawe, "Partially end-pumped Nd:YAG slab laser with a hybrid resonator," *Opt. Lett.*, vol. 23, pp. 370–372, Mar. 1998.

[41] R. A. Chodzko and A. N. Chester, *Optical Aspects of Chemical Lasers.* N. Y.: J. Wiley and Sons, 1976.

[42] K. E. Oughstun, *Unstable Resonator Modes*, vol. XXIV. B. V.: Elsevier Science Publishers, 1987.

[43] M. Morin, "Graded reflectivity mirror unstable laser resonators," *Opt. and Quantum Electron.*, vol. 29, pp. 819–866, 1997.

[44] A. E. Siegman, *Lasers*, p. 686. California: Mill Valley, 1986.

[45] J. T. LaTourette, S. F. Jacobs, and P. Rabinowitz, "Improved Laser Angular Brightness Through Diffraction Coupling," *Appl. Opt.*, vol. 3, pp. 981–982, Aug. 1964.

[46] W. F. Krupke and W. R. Sooy, "Properties of an Unstable Confocal Resonator CO_2 Laser System," *IEEE J. Quantum Electron.*, vol. QE-5, pp. 575–586, Dec. 1969.

[47] A. E. Siegman and R. Arrathoon, "Modes in Unstable Optical Resonators and Lens Waveguides," *IEEE J. Quantum Electron.*, vol. QE-3, pp. 156–163, Apr. 1967.

[48] A. E. Siegman, "Unstable Optical Resonator," *Appl. Opt.*, vol. 13, pp. 353–367, Feb. 1974.

[49] R. L. Sanderson and W. Streifer, "Laser Resonators with Tilted Reflectors," *Appl. Opt.*, vol. 8, pp. 2241–2248, Nov. 1969.

[50] Y. A. Anan'ev, N. A. Sventsitskaya, and V. E. Sherstobitov, "Properties of a laser with an unstable resonator," *Sov. Phys. JETP*, vol. 28, pp. 69–74, Jan. 1969.

[51] P. E. Dyer, D. J. James, and S. A. Ramsden, "Single transverse mode operation of a pulsed volume excited atmospheric pressure CO_2 laser using an unstable resonator," *Opt. Commun.*, vol. 5, pp. 236–238, Jul. 1972.

[52] Y. A. Anan'ev and V. E. Sherstobitov *Sov. J. Quantum Electron.*, vol. 1, p. 263, 1971.

[53] A. Yariv and P. Yeh, "Confinement and stability in optical resonators employing mirrors with gaussian reflectivity tapers*," *Opt. Commun.*, vol. 13, pp. 370–374, Apr. 1975.

[54] L. W. Casperson and S. D. Lunnam, "Gaussian Modes in High Loss Laser Resonators," *Appl. Opt.*, vol. 14, pp. 1193–1199, May 1975.

[55] M. S. Bowers, "Diffractive analysis of unstable optical resonators with super-Gaussian mirrors," *Opt. Lett.*, vol. 17, pp. 1319–1321, Oct. 1992.

[56] G. Giuliani, Y. K. Park, and R. L. Byer, "Radial birefringent element and its application to laser resonator design," *Opt. Lett.*, vol. 5, pp. 491–493, Nov. 1980.

[57] J. M. Eggleston, G. Giuliani, and R. L. Byer, "Radial intensity filters using radial birefringent elements," *J. Opt. Soc. Am.*, vol. 71, pp. 1264–1272, Oct. 1981.

[58] G. Emiliani, A. Piegari, S. D. Silvestri, P. Laporta, and V. Magni, "Optical coatings with variable reflectance for laser mirrors," *Appl. Opt.*, vol. 28, pp. 2832–2837, Jul. 1989.

[59] G. Duplain, P. G. Verly, J. A. Dobrowolski, A. Waldorf, and S. Bussiere, "Graded-reflectance mirrors for beam quality control in laser resonators," *Appl. Opt.*, vol. 32, pp. 1145–1153, Mar. 1993.

[60] A. Piegari and G. Emiliani, "Laser mirrors with variable reflected intensity and uniform phase shift: Design process," *Appl. Opt.*, vol. 32, pp. 5454–5461, Oct. 1993.

[61] N. McCarthy and P. Lavigne, "Large-size Gaussian mode in unstable resonators using Gaussian mirrors," *Opt. Lett.*, vol. 10, pp. 553–555, Nov. 1985.

[62] G. M. Ancellet, R. T. Menzies, and A. M. Brothers, "Frequency Stabilization and Transverse Mode Discrimination in Injection-Seeded Unstable Resonator TEA CO_2 Lasers," *Appl. Phys. B*, vol. 44, pp. 29–35, 1987.

[63] A. E. Siegman, *Lasers*, ch. 22-23. Mill Valley, California: University Science Books, 1986.

[64] P. Horwitz, "Asymptotic Theory of Unstable Resonaotr Modes*," *J. Opt. Soc. Am.*, vol. 63, pp. 1528–1543, Dec. 1973.

[65] P. Horwitz, "Modes in Misaligned Unstable Resonators," *Appl. Opt.*, vol. 15, pp. 167–178, Jan. 1976.

[66] W. H. Southwell, "Unstable-resonator-mode derivation using virtual-source theory," *J. Opt. Soc. Am. A*, vol. 3, pp. 1885–1891, Nov. 1986.

[67] M. A. Lauder and G. H. C. New, "Biorthogonality properties and excess noise factors of unstable optical resonators," *Opt. Commun.*, vol. 67, pp. 343–348, Aug. 1988.

[68] A. G. Fox and T. Li, "Resonant Modes in a Maser Interferometer," *Bell Syst. Tech. J.*, pp. 453–488, Mar. 1961.

[69] A. G. Fox and T. Li, "Computation of Optical Resonator Modes by the Method of Resonance Excitation," *IEEE J. Quantum Electron.*, vol. QE-4, pp. 460–465, Jul. 1968.

[70] A. Parent, N. McCarthy, and P. Lavigne, "Effects of Hard Apertures on Mode Properties of Resonators with Gaussian Reflectivity Mirrors," *IEEE J. Quantum Electron.*, vol. QE-23, pp. 222–228, Feb. 1987.

[71] S. D. Silvestri, P. Laporta, V. Magni, and O. Svelto, "Solid-State Laser Unstable Resonators with Tapered Reflectivity Mirrors: The Super-Gaussian Approach," *IEEE J. Quantum Electron.*, vol. QE-24, pp. 1172–1177, Jun. 1988.

[72] S. D. Silvestri, P. Laporta, V. Magni, O. Svelto, and B. Majocchi, "Unstable laser resonators with super-Gaussian mirrors," *Opt. Lett.*, vol. 13, pp. 201–203, Mar. 1988.

[73] S. D. Silvestri, V. Magni, O. Svelto, and G. Valentini, "Lasers with Super-Gaussian Mirrors," *IEEE J. Quantum Electron.*, vol. QE-26, pp. 1500–1509, Sep. 1990.

[74] P. Lavigne, N. McCarthy, A. Parent, and K. J. Snell, "Laser mode control with variable reflectivity mirrors," *Can. J. Phys.*, vol. 66, pp. 888–895, Oct. 1988.

[75] R. Wynne, J. L. Daneu, and T. Y. Fan, "Thermal coefficients of the expansion and refractive index in YAG," *Appl. Opt.*, vol. 38, pp. 3282–3284, May 1999.

[76] J. Marion, "Strengthened solid-state laser materials," *Appl. Phys. Lett.*, vol. 47, pp. 694–696, Oct. 1985.

[77] D. Dawes, "Nd:YAG-the versatile high-power solid-state laser crystal," *Indust. Laser Rev.*, Mar. 1995.

[78] J. E. Marion, "Fracture Mechanisms and Strengthening of Slab Lasers," *SPIE*, vol. 736, pp. 2–12, 1987.

[79] D. Ottaway, D. Mudge, M. W. Hamilton, J. Munch, and P. J. Veitch, "Stable, high power Nd:YAG lasers for gravitational wave interferometers," XX International Quantum Electronics Conference, (Sydney, Australia), p. Paper FE7, 1996.

[80] D. J. Ottaway, P. J. Veitch, M. W. Hamilton, C. Hollitt, D. Mudge, and J. Munch, "A Compact Injection-Locked Nd:YAG Laser for Gravitational Wave Detection," *IEEE J. Quantum Electron.*, vol. 34, pp. 2006–2009, Oct. 1998.

[81] D. J. Ottaway, P. J. Veitch, C. Hollitt, D. Mudge, M. W. Hamilton, and J. Munch, "Frequency and Intensity Noise of an Injection-Locked Nd:YAG Ring Laser," *Appl. Phys. B*, vol. B71, pp. 163–168, Aug. 2000.

[82] R. A. Serway, *Physics for Scientists Engineers with Modern Physics.* U.S.A.: Saunders College Publishing, 3rd ed., 1990.

[83] W. Koechner, *Solid-State Laser Engineering.* N. Y.: Springer-Verlag, 3rd ed., 1992.

[84] J. E. Murray, "Pulsed Gain and Thermal Lensing of Nd:$LiYF_4$," *IEEE J. Quantum Electron.*, vol. QE-19, pp. 488–491, Apr. 1983.

[85] A. E. Siegman, *Lasers.* Mill Valley, California: University Science Books, 1986.

[86] A. E. Siegman, *Lasers*, p. 691. Mill Valley, California: University Science Books, 1986.

[87] D. C. Brown, "Nonlinear Thermal and Stress Effects and Scaling Behavior of YAG Slab Amplifiers," *IEEE J. Quantum Electron.*, vol. 34, pp. 2393–2402, Dec. 1998.

[88] D. C. Brown, "Nonlinear Thermal Distortion in YAG Rod Amplifiers," *IEEE J. Quantum Electron.*, vol. 34, pp. 2383–2392, Dec. 1998.

[89] A. E. Siegman, *Lasers*, p. 781. Mill Valley, California: University Science Books, 1986.

[90] P. Baues, "Huygens' principle in inhomogeneous isotropic media and a general integral equation applicable to optical resonators," *Opto-Electronics*, vol. 1, pp. 37–44, 1969.

[91] J. S. A. Collins, "Lens-system diffraction integral written in terms of matrix optics," *J. Opt. Soc. Am.*, vol. 60, p. 1168, Sep. 1970.

[92] Sciopt Enterprises, P.O. Box 20637, San Jose, CA 95160 U.S.A., *Paraxia - Resonator and Optics Programs*, 2.0 ed.

[93] A. E. Siegman, *Lasers*, pp. 584–587. Mill Valley, California: University Science Books, 1986.

[94] A. E. Siegman, *Lasers*, p. 869. Mill Valley, California: University Science Books, 1986.

[95] A. E. Sigeman, *Lasers*, ch. 23, p. 916. Mill Valley, California: University Science Books, 1986.

[96] A. E. Siegman, "New developments in laser resonators," *SPIE*, vol. 1224, pp. 2–14, 1990.

[97] A. E. Siegman, "Defining, measuring, and optimizing laser beam quality," *SPIE*, vol. 1868, pp. 2–12, 1993.

[98] N. McCarthy and P. Lavigne, "Optical resonators with Gaussian reflectivity mirrors: output beam characteristics," *Appl. Opt.*, vol. 23, pp. 3845–3850, Nov. 1984.

[99] C. Paré, "Optimum laser beam profile for maximum energy extraction from a saturable amplifier," *Opt. Commun.*, vol. 123, pp. 762–776, Feb 1996.

[100] A. E. Siegman, *Lasers*, p. 769. Mill Valley, California: University Science Books, 1986.

[101] D. G. Matthews, J. R. Boon, R. S. Conroy, and B. D. Sinclair, "A comparative study of diode pumped microchip laser materials: Nd-doped YVO_4, YOS, SFAP and SVAP," *J. Mod. Opt.*, vol. 43, pp. 1079–1087, May 1996.

[102] S. Zhao, Q. Wang, X. Zhang, L. Sun, and S. Zhang, "Laser characteristics of a new crystal Nd:$Sr_5(PO_4)_3F$ at 1.059μm," *Opt. Laser Technol.*, vol. 28, pp. 477–480, Sep. 1996.

[103] Y. Chen, L. Major, and V. Kushawaha, "Efficient laser operation of diode-pumped Nd:$KGd(WO_4)_2$ crystal at 1.067 μm," *Appl. Opt.*, vol. 35, pp. 3203–3206, Jun. 1996.

[104] R. Moncorge, B. Chambon, J. Y. Rivoire, N. Garnier, E. Descroix, P. Laporte, H. Guillet, S. Roy, J. Mareschal, D. Pelenc, J. Doury, and P. Farge, "Nd doped crystals for medical laser applications," *Opt. Materials*, vol. 8, pp. 109–119, Jul. 1997.

[105] S. A. Payne, R. J. Beach, C. Bibeau, C. A. Ebbers, M. A. Emanuel, E. C. Honea, C. D. Marshall, R. H. Page, K. I. Schaffers, J. A. Skidmore, S. B. Sutton, and W. F. Krupke, "Diode Arrays, Crystals, and Thermal Management for Solid-State Lasers," *IEEE J. Selected Topics in Quantum Electron.*, vol. 3, pp. 71–81, Feb. 1997.

[106] S. Guy, C. L. Bonner, D. P. Shepherd, D. C. Hanna, A. C. Tropper, and B. Ferrand, "High-Inversion Densities in Nd:YAG: Upconversion and Bleaching," *IEEE J. Quantum Electron.*, vol. 34, pp. 900–909, May 1998.

[107] T. Chuang and H. R. Verdun, "Energy transfer Up-Conversion and Excited State Absorption of Laser Radiation in Nd:YLF Laser Crystals," *IEEE J. Quantum Electron.*, vol. 32, pp. 79–91, Jan. 1996.

[108] S. Kuck, L. Fornasiero, E. Mix, and G. Huber, "Excited state absorption and stimulated emission of nd^{3+} in crystals. part I: $Y_3Al_5O_{12}$, $YAlO_3$, and Y_2O_3," *Appl. Phys. B*, vol. 67, no. 2, pp. 151–156, 1998.

[109] L. Fornasiero, S. Kuck, T. Jensen, G. Huber, and B. H. T. Chai, "Excited state absorption and stimulated emission of Nd^{3+} in crystals. part 2: YVO_4, $GdVO_4$, and $Sr_5(PO_4)_3F$," *Appl. Phys. B*, vol. 67, no. 5, pp. 549–553, 1998.

[110] L. Fornasiero, T. Kellner, S. Kuck, J. P. Meyn, P. E.-A. Mobert, and G. Huber, "Excited state absorption and stimualted emission of Nd^{3+} in crystals III: $LaSc_3(BO_3)_4$, $CaWO_4$, and $YLiF_4$," *Appl. Phys. B*, vol. 68, no. 1, pp. 67–72, 1999.

[111] Y. Guyot, H. Manna, J. Y. Rivoire, R. Moncorge, N. Garnier, E. Descroix, M. Bon, and P. Laporte, "Excited-state-absorption and upconversion studies of Nd^{3+}-doped single crystals $Y_3Al_5O_{12}$, $YLiF_4$, and $LaMgAl_{11}O_{19}$," *Phys. Rev. B*, vol. 51, pp. 784–799, Jan. 1995.

[112] V. Kushawaha and Y. Chen, "CW and quasi-CW diode-laser-pumped Nd:SSGM," *Appl. Phys. B*, vol. 60, no. 1, pp. 67–69, 1995.

[113] F. Hanson, D. Dick, H. R. Verdun, and M. Kokta, "Optical properties and lasing of Nd:$SrGdGa_3O_7$," *J. Opt. Soc. Am. B*, vol. 8, pp. 1668–1673, Aug. 1991.

[114] T. Graf and J. Balmer, "Lasing properties of diode-laser-pumped Nd:KGW," *Opt. Eng.*, vol. 34, pp. 2349–2352, Aug. 1995.

[115] M. J. Weber, M. Bass, K. Andringa, R. R. Monchamp, and E. Comperchio, "Czochralski growth and properties of $YAlO_3$ laser crystals," *Appl. Phys. Lett.*, vol. 15, pp. 342–345, Nov. 1969.

[116] G. A. Massey, "Criterion for selection of cw laser host materials to increase available power in the fundamental mode," *Appl. Phys. Lett.*, vol. 17, pp. 213–215, Sep. 1970.

[117] G. A. Massey, "Measurements of Device Parameters for Nd:$YAlO_3$ Laser," *IEEE J. Quantum Electron.*, vol. QE-8, pp. 669–674, Jul. 1972.

[118] F. Hanson and P. Poirier, "Multiple-wavelength operation of a diode-pumped Nd:$YAlO_3$ laser," *J. Opt. Soc. Am. B*, vol. 12, pp. 1311–1315, Jul. 1995.

[119] L. Schearer and M. Leduc, "Tuning Characteristics and New Laser Lines in an Nd:YAP CW Laser," *IEEE J. Quantum Electron.*, vol. QE-22, pp. 756–758, Jun. 1986.

[120] N. Hodgson, D. J. Golding, and D. Eisel, "Efficient high power operation at 1.44 μm of Nd-doped crystals," *SPIE*, vol. 2206, pp. 426–436, 1994.

[121] T. M. Baer, D. F. Head, P. Gooding, G. J. Kintz, and S. Hutchison, "Performance of Diode-Pumped Nd:YAG and Nd:YLF Lasers in a Tightly Folded Resonator Configuration," *IEEE J. Quantum Electron.*, vol. 28, pp. 1131–1138, Apr. 1992.

[122] Z. Zeng, H. Shen, M. Huang, H. Xu, R. Zeng, Y. Zhou, G. Yu, and C. Huang, "Measurement of the refractive index and thermal refractive index coefficients of Nd:YAP crystal," *Appl. Opt.*, vol. 29, pp. 1281–1286, Mar. 1990.

[123] Litton Airtron SYNOPTICS, Charlotte, NC, USA, *Synthetic Crystal and Opt. Products Catalogue.*

[124] T. Chin, R. C. Morris, O. Kafri, M. Long, and D. F. Heller, "Athermal Nd:BEL Lasers," *SPIE*, vol. 622, pp. 53–60, 1986.

[125] H. Shen, R. R. Zeng, Y. Zhou, G. F. Yu, C. Huang, Z. Zeng, W. J. Zhang, and Q. J. Ye, "Simultaneous Multiple Wavelength Laser Action in Various Neodymium Host Crystals," *IEEE J. Quantum Electron.*, vol. 27, pp. 2315–2318, Oct. 1991.

[126] D. Pruss, G. Huber, A. Beimowski, V. V. Laptev, I. A. Shcherbakov, and Y. V. Zharikov, "Efficient Cr^{3+} Sensitized Nd^{3+}: GdScGa-Garnet Laser at 1.06 μm," *Appl. Phys. B*, vol. 28, no. 4, pp. 355–358, 1982.

[127] V. G. Ostroumov, Y. S. Privis, V. A. Smirnov, , and I. A. Shcherbakov, "Sensitizing of Nd^{3+} luminescence by Cr^{3+} in gallium garnets," *J. Opt. Soc. Am. B*, vol. 3, pp. 81–93, Jan. 1986.

[128] T. M. Pollak, W. F. Wing, R. J. Grasso, E. P. Chicklis, and H. P. Jenssen, "CW Laser Operation of Nd:YLF," *IEEE J. Quantum Electron.*, vol. QE-18, pp. 159–162, Feb. 1982.

[129] C. J. Flood, D. R. Walker, and H. M. V. Driel, "CW diode pumping and FM mode locking of a Nd:KGW laser," *Appl. Phys. B*, vol. 60, no. 2/3, pp. 309–312, 1995.

[130] T. J. Kane, J. M. Eggleston, and R. L. Byer, "The Slab Geometry Laser-Part II: Thermal Effects in a Finite Slab," *IEEE J. Quantum Electron.*, vol. QE-21, pp. 1195–1210, Aug. 1985.

[131] G. A. Slack and D. W. Oliver, "Thermal conductivity of garnets and phonon scattering by rare-earth ions," *Phys. Rev. B*, vol. 4, pp. 592–608, 1971.

[132] V. Kushawaha and L. Major, "Relative performance of a 1.06 μm laser with various Nd doped crystals," *Opt. and Laser Technol.*, vol. 26, no. 5, pp. 351–353, 1994.

[133] Union Carbide, 750S. 32nd street, Washougal, WA 98671, *Union Carbide Crystal Products Nd:YAG.*

[134] V. Optics, *Virgo Optics Nd:YVO_4*. Division of Sandoz Chemicals Corporation, 6736 Commerce Avenue, Port Richey, Florida 34668.

[135] I. V. Mochalov, "Nonlinear optics of the potassium gadolinium tungstate laser crystal Nd^{3+}:$KGd(WO_4)_2$," *J. Opt. Technol.*, vol. 62, pp. 746–756, Nov. 1995.

[136] R. C. Morris, C. F. Cline, R. F. Begley, M. Dutoit, P. J. Harget, H. P. Jenssen, T. S. L. France, and R. Webb, "Lanthanum beryllate: A new rare-earth ion laser host," *Appl. Phys. Lett.*, vol. 27, pp. 444–445, Oct. 1975.

[137] S. A. Payne, B. H. T. Chai, W. L. Kway, L. D. DeLoach, L. K. Smith, G. Lutts, R. Peale, X. X. Zhang, G. D. Wilke, and W. F. Krupke, "New High Cross Section Laser Crystal: Neodymium-Doped Strontium Fluorovanadate," in *Conference on Lasers and Electro-Optics, OSA Technical Digest Series, Vol. 11*, (Washington, D. C.), pp. 692–693, Optical Society of America, 1993.

[138] N. Faure, C. Borel, M. Couchaud, G. Basset, R. Templier, and C. Wyon, "Optical properties and laser performance of neodymium doped scheelites $CaWO_4$ and $NaGd(WO_4)_2$," *Appl. Phys. B*, vol. 63, no. 6, pp. 593–598, 1996.

[139] J. R. Thornton, W. D. Fountain, G. W. Flint, and T. G. Crow, "Properties of Neodymium Laser Materials," *Appl. Opt.*, vol. 8, pp. 1087–1102, Jun. 1969.

[140] J. L. Dallas, "Frequency-Modulation Mode-Locking Performance for Four Nd^{3+}-Doped Laser Crystals," *Appl. Opt.*, vol. vol. 33, pp. 6373–6376, Sep. 1994.

[141] J. R. Ryan and R. Beach, "Optical absorption and stimulated emission of neodymium in yttrium lithium fluoride," *J. Opt. Soc. Am. B*, vol. 9, pp. 1883–1887, Oct. 1992.

[142] N. P. Barnes, M. E. Storm, P. L. Cross, and M. W. S. Jr., "Efficiency of Nd Laser Materials with Laser Diode Pumping," *IEEE J. Quantum Electron.*, vol. 26, pp. 558–569, Mar. 1990.

[143] W. Koechner, *Solid-State Laser Engineering.* New York: Springer-Verlang, 1st ed.

[144] N. P. Barnes, D. J. Gettemy, L. Esterowitz, and R. E. Allen, "Comparison of Nd 1.06 and 1.33 μm Operation in Various Hosts," *IEEE J. Quantum Electron.*, vol. QE-23, pp. 1434–1451, Sep. 1987.

[145] G. J. Kintz and T. Baer, "Single-Frequency Operation in Solid-State Laser Materials with Short Absorption Depths," *IEEE J. Quantum Electron.*, vol. 26, pp. 1457–1459, Sep. 1990.

[146] A. W. Tucker, M. Birnbaum, and C. L. Fincher, "Stimulated emission cross sections of Nd:YVO_4 and Nd:$La_2Be_2O_5$ (BeL," *J. Appl. Phys.*, vol. 52, pp. 3067–3068, Apr. 1981.

[147] C. C. Bradley, J. Chen, and G. Hulet, "Instrumentation for the stable operation of laser diodes," *Rev. Sci. Instrum.*, vol. 61, pp. 2097–2101, Aug. 1990.

[148] N. Hodgson and H. Weber, *Optical Resonators, Fundamentals, Advanced Concepts and Applications.* NY: Springer-Verlag, 1997.

[149] "Private communication between Martin Ostermeyer and Norman Hodgson, regarding error in text.,"